A MEASUREMENT OF PROTON-PROTON AND PROTON-ANTIPROTON FORWARD ELASTIC SCATTERING AT $\sqrt{s}$ = 24.3 GeV WITH SILICON BARRIER DETECTORS

A thesis
submitted to the Faculty of The Rockefeller University
in partial fulfillment of the requirements
for the degree of Doctor of Philosophy

by

Richard E. Breedon

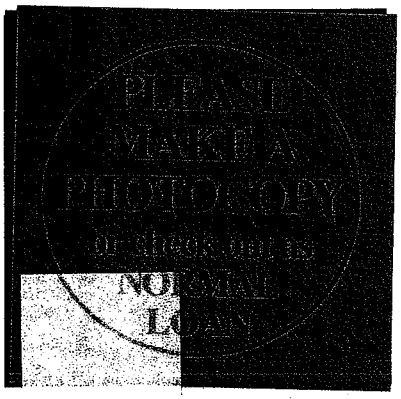

1 April 1988
The Rockefeller University
New York, New York USA

Dedicated to my father,

Edward A. Breedon

(1929-1984)

"We are spending millions of francs in order to clean up the vacuum chamber and the vacuum is as good as the vacuum on the moon, and those guys over there start blowing gas on it."

-Carlo Rubbia
(as quoted in G. Taubes, **Nobel dreams**)

ABSTRACT

This report presents a measurement of the elastic differential cross sections for pp and $\bar{p}p$ scattering,

$$p + p \rightarrow p + p \quad \text{and} \quad \bar{p} + p \rightarrow \bar{p} + p,$$

within the four-momentum transfer range $0.001 \leq |t| \leq 0.06$ $(GeV/c)^2$ at center-of-mass energy 24.3 GeV. From the measurement of the interference between the Coulomb and nuclear amplitudes, the experiment obtained ρ, the ratio of the real part to the imaginary part of the nuclear elastic amplitude at $t = 0$. In addition, the slope of the forward diffractive peak was determined. The measurement was performed as part of Experiment UA6 using a hydrogen gas-jet target and the beams of the CERN SPS which runs when the accelerator operates in collision mode. The kinetic energy, E, recoil angle, θ, and time-of-flight of the low energy scattered target proton (the "recoil" proton) was given by an array of silicon barrier detectors at close to 90° to the beams.

The solid state detector array consisted of a position sensitive detector and three "stacks" of two conventional silicon barrier detectors each. All detectors were mounted on an arm which could be rotated 180° by remote control so that the same detectors could intercept recoils from either pp or $\bar{p}p$ collisions. The arm pivotted within a vacuum chamber which could be moved ±20° from its central position perpendicular to the beams. The detectors were calibrated using 5.5 MeV alpha sources, then the four-momentum-transfer scale was given by

$$|t| = 2m_p E.$$

Excellent background control was obtained from cutting on the time-of-flight and the recoil angle, which for elastic scattering is related to t by

$$|t| = 4m_p^2 \sin^2\theta .$$

In addition, for the stack detectors, the front detector provided a dE/dx measurement and with the rear detector yielded the total energy, enabling particle identification of the recoil proton. The contribution of single diffractive dissociation

$$p(\bar{p}) + p \rightarrow X + p$$

was subtracted based upon a parametrization from Fermilab data. Losses were corrected by Monte Carlo. Data collected at different angles of the vacuum chamber were combined using the integrated luminosity as measured by an additional set of four fixed silicon detectors.

For fitting the differential cross section, values for the total cross sections of pp and $\bar{p}p$ were obtained from a dispersion relation fit to data from other experiments. The fit results for the nuclear slope were $b(pp) = 11.4 \pm 0.5 \pm 0.1$ and $b(\bar{p}p) = 12.3 \pm 0.5 \pm 0.1$ (Gev^{-2}). For the real part measurement, $\rho(pp) = 0.009 \pm 0.010 \pm 0.006$ and $\rho(\bar{p}p) = 0.048 \pm 0.011 \pm 0.006$ were obtained. The real part results are compared to predictions from dispersion relations and to an "odderon" model.

PREFACE

Pursuant to research in high energy physics, I was led to ask myself, to paraphrase Kierkegaard, 'Is there a teleological suspension of the sensible?'[1] The rewards for this effort have been the excellent friends and colleagues I have met along the way, and with whom I have shared in this 'suspension of the sensible.'

Foremost is Rodney L. Cool, my research advisor, who at a crucial time persuaded me to become Rockefeller's second experimental high energy physics graduate student. After entrusting me with the experiment, his advice and direction at all successive stages were essential. Rod brought to physics rare grace and style and his passing during the concluding phase of this project has left a disconsolate loss.

Special thanks are due to Dino Goulianos for his contributions to the elegant design of the experiment. His counsel during analysis was invaluable and his readiness to explain to me his physical insight helped to deepen my understanding. Also of great help were Sebastian White and Tom Chapin, who in addition helped me to tame the Rockefeller VAX to analyze dozens of tapes written at CERN.

I consider myself fortunate for having had the opportunity to work on two experiments with Leslie Camilleri, whose capacity for subtle leadership and restraint will always serve as a model for me.

I gratefully acknowledge all effort that went into making this measurement and I mention some of the contributors here. The experiment was designed and constructed at Rockefeller University by Rod, Dino, Sebastian, and Tom with the technical assistance of Dragoslav Scepanovic and Richard Heidecker. Installation at CERN was accomplished by Tom and Sebastian with technical assistance by André Kupferschmid and Werner Huta. The controlling electronics were installed by Rod, Guy von Dardel and myself. Data aquisition and on-line analysis software were written by Didier Steiner, Bernard Gabioud and myself. Didier also modified and programmed the

---

1 'Is there a teleological suspension of the ethical?' Problem I in Søren Kierkegaard, Fear and Trembling (1843).

Auxillary Crate Controller. I performed all data collection, calibrations, hardware modifications and data compaction and wrote the analysis programs. All errors are of course mine.

A vital aspect of the experiment was that it was located in Switzerland. I thank my friends Tim Cox, who shared with me walks in the mountains followed by raclette at Cave Sierroise, and Andrea Vacchi for evenings of chess and grappa amid the warmth of his family. Greg Snow deserves praise for introducing me to the delights of lunch at the piscine de Meyrin. The Geneva Experience would not be complete without mentioning my friends Helen, Halina, Helena, Manuela and Charling. And it would be impossible to forget meine Süsse, Marie-Anne, for never failing to announce "Kaffeezeit!"

The support of the rest of the CERN-Lausanne-Michigan-Rockefeller Collaboration who somehow escaped being mentioned so far is also appreciated: J. Antille, S. Baumann, A. Bernasconi, J.C. Berney, L. Dick, E.C. Dukes, M. Duro, F. Gaille, P. Giacomelli, J.B. Jeanneret, C. Joseph, W. Kubischta, J.F. Loude, E. Malamud, C. Morel, O. Overseth, J.P. Perroud, P. Petersen, R. Rusack, M.T. Tran and G. Valenti.

On the home front I thank Ruth Snyder for making the department feel like home, Randy Furlong for supplying me with the answers to Jackson problems when I needed them and Karen Ferris for jazz theory lessons on the Casio in between drawings. Most dearly I thank Sumi Koide for her love and patience.

Lastly I thank the members of my family for their support, especially my father without whose encouragement and expectations this work would have never been begun.

TABLE OF CONTENTS

LIST OF FIGURES

LIST OF TABLES

CHAPTER 1 Introduction

Elastic scattering has proved to be an active testing ground for assumptions based on the fundamental principles of unitarity, analyticity and crossing symmetry and for models of the energy dependence of the total cross section. These assumptions are applied to experimental measurements through the optical theorem, which relates the imaginary (absorptive) part of the elastic scattering amplitude to the total cross section, and by dispersion relations, which connect the small real part of the amplitude to the imaginary part. From measurements of the elastic differential cross section at very small scattering angles, the real part is determined, which may then be compared via these relations to model fits to the total cross section. It is especially fruitful to compare high energy measurements of collisions of different particles types, such as protons and antiprotons, which was the motivation of the measurement performed by Experiment UA6 at CERN, the European Center for Particle Physics, discussed in this report.

In the first particle scattering experiment, Rutherford [1.1] measured the angle of deflection of alpha particles directed at a gold foil. If the energy of the scattered particle is also measured, one has available a constraint with which to establish the elasticity of the collision. The same information may be obtained by measuring the angle and energy of the target, or recoil, particle. Then the momentum transfer squared is directly related to E, the kinetic energy of the recoil particle, by

$$|t| = 2mE \qquad (1.1)$$

where m is the target mass. For measurements of pp or $\bar{p}p$ scattering at low momentum transfer the recoils are of very low energy, so thin targets and sensitive detectors are necessary.

The first use of the recoil technique for the study of small angle pp elastic scattering at high energies took place in the early 60's at JINR in Dubna, USSR using an internal polyethylene foil as a target [1.2]. Later a hydrogen jet was developed to supply target protons to accelerated beams first at Serpukov [1.3] and then at Fermilab [1.4] in the early 70's.

At about the same time, the CERN-Rome Collaboration [1.5] and the Pisa-Stonybrook Collaboration [1.6] measured the pp cross section at the CERN Intersecting Storage Rings (ISR) in the energy range between 23 and 63 GeV and discovered the celebrated rise in the total cross section. The construction of an antiproton facility at CERN enabled the pp scattering measurements made at the ISR to be extended to $\bar{p}p$. Using the "Roman pot" method pioneered by Amaldi et al., the $\bar{p}p$ and pp low |t| elastic differential cross sections were measured at center-of-mass energies $\sqrt{s}$ = 30.7, 52.8 and 62.5 GeV by Amos et al. [1.7]. The optical theorem was then used to demonstrate a rising total cross section for $\bar{p}p$, which was confirmed by measurements of the total interaction rate at $\sqrt{s}$ = 52.8 GeV by Carboni et al. [1.8]. The measurements of ρ, the ratio of the real to the imaginary part of the scattering amplitude, by Amos et al. for $\bar{p}p$ at $\sqrt{s}$ = 30.7 and 52.8 GeV, showed that ρ is positive and rising over ISR energies, as

expected from the behavior of the total cross sections. However, most recently at the Collider energy of $\sqrt{s}$ = 546 GeV, the UA4 Collaboration has found a value of $\rho(\bar{p}p)$ definitely higher than what was anticipated by conventional fits to data on the total cross section and lower energy ρ values [1.9].

Since the closure of the ISR in 1984, no machine has been available with which pp and $\bar{p}p$ interactions from beam-beam collisions may be studied with the same apparatus. But using a hydrogen jet target located between beam intersection points, Experiment UA6 is able to exploit independently both the proton and antiproton beams of the CERN SPS when it is operating in collider mode. Proposed in 1980 [1.10] by a collaboration of CERN, Université de Lausanne, University of Michigan and The Rockefeller University and approved the following year, UA6 studies high P_T phenomena and elastic and single diffractive scattering at low momentum transfer for pp and $\bar{p}p$ at $\sqrt{s}$ = 24.3 GeV.

Because UA6 is essentially a fixed target experiment, high luminosities are available for measuring the elastic differential cross section well into the Coulomb region using the recoil technique. Silicon barrier detectors are used for the energy and angle measurements of the scattered target proton. Although of small size, this type of detector has excellent linearity and energy resolution and has the advantage that it may be operated with little difficulty within the high vacuum of the SPS beam pipe.

The detectors are mounted on a carriage in a movable vacuum chamber perpendicular to the jet/beam intersection point.

For measurement of the Coulomb and interference regions at very low momentum transfer, a continuous solid state detector is used to avoid the restriction to angular resolution imposed by discrete detectors. Such position sensitive detectors were first employed for a measurement of this type with a gas-jet target at Fermilab by the USA-USSR Collaboration [1.11]. The UA6 detector array consists of one position sensitive detector, three sandwiches or "stacks" of discrete detectors for recording larger angle recoils and one stack for monitoring the background. The range of momentum transfer of the position sensitive detector is approximately $0.001 \leq |t| \leq 0.014$ $(GeV/c)^2$ while the stack detectors provide coverage between 0.03 to 0.06 $(GeV/c)^2$. The array can be rotated 180° to intercept recoils from either pp or $\bar{p}p$ collisions and the carriage can be moved to a variety of angles. In addition, four fixed detectors provide a measure of the integrated luminosity used to combine data collected at different angles.

Rates of elastically scattered recoil protons yield the differential cross section, which is normalized using the optical theorem with values of $\sigma_{tot}(pp)$ and $\sigma_{tot}(\bar{p}p)$ derived from other experiments. We have chosen not to normalize on the known Coulomb cross section. Sufficient accuracy cannot be obtained since penetration into the Coulomb region is limited by the intrinsic resolution of the position sensitive detector, although coverage

is excellent over the interference region. From the differential cross section two significant quantities are derived. One is the ratio ρ of the real to the imaginary part of the nuclear scattering amplitude at four-momentum transfer squared (t) near zero. This is found by measuring the interference between the Coulomb amplitude and the nuclear amplitude and is most sensitively determined in the t range where the two amplitudes are approximately equal. At the UA6 energy, recoil protons from collisions within this range have kinetic energy centered around 0.9 MeV and are deflected to an angle θ around 22 milliradians from 90° to the beam. Recoils with these small energies and scattering angles are collected by the position sensitive detector. The other quantity of interest is the nuclear slope parameter b, defined by

$$\frac{d\sigma_n}{dt} = \left\{\frac{d\sigma}{dt}\right\}_{t=0} e^{bt}. \qquad (1.2)$$

In this expression, $d\sigma_n/dt$ is the invariant differential cross section, which exhibits a large forward peak corresponding to the diffractive peak of optical models. The forward peak has been found to shrink with increasing energy, hence b is not constant but varies slowly with energy and momentum transfer. In this experiment the differential cross section is measured at such low recoil energy that b is determined essentially at the t=0 limit.

CHAPTER 2 The Measurement of pp and $\bar{p}p$ Elastic Scattering

2.1 Kinematics and the Differential Cross Section

Elastic scattering, for spinless particles, is fully characterized by two invariants: the square of the total center-of-mass energy s and the four-momentum transfer t defined as

$$s = (p_1 + p_2)^2 \tag{2.1a}$$

$$t = (p_1 - p_1')^2 \tag{2.1b}$$

as shown in Figure 2.1a. Note that for a scattering experiment in this metric, $s > 0$ and $t < 0$. Also of interest is a special class of inelastic interactions, inclusive single diffractive dissociation (SDD), $p(\bar{p}) + p \rightarrow X + p$, where the incident particle is excited to a higher mass state in the scattering process. One must then specify, in addition to s and t, the invariant mass (missing mass), M_x, of all the other particles in the final state (Figure 2.1b):

$$M_x = (p_1 + p_2 - p_2')^2 \ . \tag{2.2a}$$

This study investigates elastic scattering in which the four-momentum transfer is very small compared with the mass of the proton m. The SDD process contributes a background. We use units in which $c = \hbar = 1$.

In the laboratory frame, E_0 is the beam energy, θ is the recoil scattering angle from 90° and $s = 2m^2 + 2mE_0$. Eq. 2.2a becomes

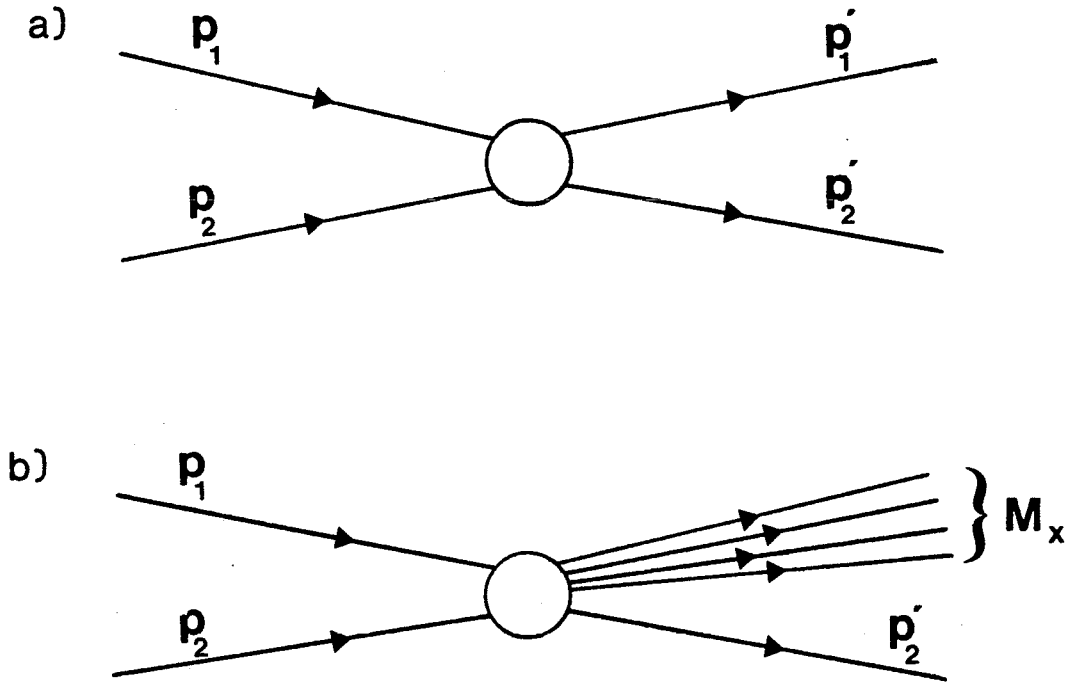

Figure 2.1 Diagrams of kinematic definitions for a) elastic scattering, b) diffractive dissociation.

$$M_x^2 = m^2 + \frac{s|t|}{2m^2}\left\{ -1 + \beta\cdot\sin\theta \left(1 + \frac{4m^2}{|t|} \right)^{1/2} \right\} \qquad (2.2b)$$

which is exact. For high energies, $E_0 \gg m$, and for small momentum transfer, $|t| \ll 4m^2$, the approximate relation

$$M_x^2 \approx m^2 + 2p\sqrt{|t|}\left(\sin\theta - \frac{\sqrt{|t|}}{2m} \right) \qquad (2.3)$$

is quite adequate. Here p = 315 GeV/c is the incident beam momentum. For **elastic scattering**, $M_x^2 = m^2$, which in Eq. 2.3 yields

$$|t| = 4m^2 \sin^2\theta \qquad (2.4)$$

showing how $|t|$ is uniquely determined by the recoil angle.

If the lab scattering amplitude is denoted by F and defined by

$$\frac{d\sigma}{d\Omega} = |F|^2,$$

then

$$\frac{d\sigma}{dt} = \frac{\pi}{p^2}|F|^2$$

and

$$\sigma_{tot} = \frac{4\pi}{p}\,\mathrm{Im}\,F(\theta = 0)\ . \qquad (2.5)$$

This last expression is the **optical theorem** which relates the imaginary part of the forward scattering amplitude to the total cross section. It is derived from the unitarity, or completeness, of the scattering matrix and

expresses the intuitive notion that the depletion of the beam in the forward direction is proportional to everything taken out by scattering into all angles.

Also useful is the invariant amplitude f(t), related to F through the relation $F = p \cdot f$. It follows that

$$\frac{d\sigma}{dt} = \pi |f|^2 \tag{2.6}$$

and

$$\sigma_{tot} = 4\pi \text{ Im } f(0). \tag{2.7}$$

An expression for the invariant differential cross section for elastic scattering at small momentum transfer will now be derived which will be used frequently. The effects of the Coulomb and nuclear fields will first be handled separately, then will be combined to act simultaneously.

The Coulomb amplitude is well approximated by

$$f_c(t) = -(\pm)\frac{2\alpha}{|t|} G^2(t) \tag{2.8}$$

where α is the fine structure constant and the upper sign is for pp while the lower sign is for $\bar{p}p$. G(t) is the proton electromagnetic form factor whose dipole form is

$$G(t) = \left(1 + \frac{|t|}{\Lambda^2} \right)^{-2} \tag{2.9}$$

where $\Lambda^2 = 0.71$ $(\text{GeV/c})^2$ is related to the electromagnetic radius of the proton. The cross section for this process is the familiar Rutherford equation

$$\frac{d\sigma_c}{dt} = \frac{4\pi\alpha^2}{t^2} G^4(t) \ . \qquad (2.10)$$

The nuclear amplitude is known empirically to be well described over a wide t region by

$$f_n(t) = \frac{\sigma_{tot}}{4\pi} (\rho + i) e^{-b|t|/2} \qquad (2.11)$$

where the optical theorem supplies the normalization and the slope parameter b is in general a slowly varying function of both s and t, but is approximately constant at small $|t|$. The parameter ρ is defined as

$$\rho = \frac{\text{Re } f_n(t=0)}{\text{Im } f_n(t=0)} \qquad (2.12)$$

and the nuclear cross section is

$$\frac{d\sigma_n}{dt} = \frac{\sigma_{tot}^2}{16\pi} (1 + \rho^2) e^{-b|t|} . \qquad (2.13)$$

With the simultaneous presence of the Coulombic and hadronic fields, a phase factor $\alpha\phi(t)$ must be introduced to reflect the distortion of the pure amplitudes. The total scattering amplitude becomes

$$f(t) = f_c(t)e^{\pm i\alpha\phi} + f_n(t) \ . \qquad (2.14)$$

The phase was first calculated by Bethe [2.1], and later improved by West and Yennie [2.2] using QED Feynman diagrams. Most recently, the phase was recalculated by Cahn [2.3] following an eikonal approach, with the result

$$\phi(t) = -\left\{ \gamma + \ln \frac{b|t|}{2} + \ln \left\{ 1 + \frac{8}{b\Lambda^2} \right\} + \frac{4|t|}{\Lambda^2} \cdot \ln \frac{4|t|}{\Lambda^2} + \frac{2|t|}{\Lambda^2} \right\} . \qquad (2.15)$$

Here $\gamma = 0.577...$ is Euler's constant and b is the nuclear slope parameter.

The full expression for the differential cross section contains three terms. The first and last represent the pure Coulomb and nuclear contributions respectively and the other the coherent interference of the Coulomb and nuclear parts. The complete form, since $\alpha\phi \ll 1$, is

$$\frac{d\sigma}{dt} = \pi | f_c(t)\, e^{\pm i\alpha\phi} + f_n(t)|^2$$

$$= \frac{4\pi\alpha^2}{t^2} G^4(t) - \frac{\pm\alpha(\rho\pm\alpha\phi)}{|t|} \sigma_{tot} G^2(t)\, e^{-b|t|/2} + \frac{(1+\rho^2)}{16\pi} \sigma_{tot}^2 e^{-b|t|}. \qquad (2.16)$$

Once again the upper sign is for pp and the lower sign for $\bar{p}p$ scattering. Figure 2.2 is a plot of this function fit to small t pp elastic differential cross section data from the ISR at $\sqrt{s} = 53.4$ GeV. The Coulomb and nuclear contributions are also shown separately.

Notice that the interference term in Eq. 2.16 is maximal when $|f_c| = |f_n|$, that is, when $d\sigma_c/dt = d\sigma_n/dt$. If the factor $(\rho \pm \alpha\phi)$ which multiplies the interference term is positive, the interference is destructive for pp and constructive for $\bar{p}p$. Since $\alpha\phi$ can be calculated, and is on the order of 0.02, the presence of the interference term allows the evaluation of ρ, the ratio of the real to the imaginary part of the forward elastic scattering amplitude, provided that σ_{tot} is also known. The Coulomb and nuclear terms of the differential cross section are of comparable magnitude when

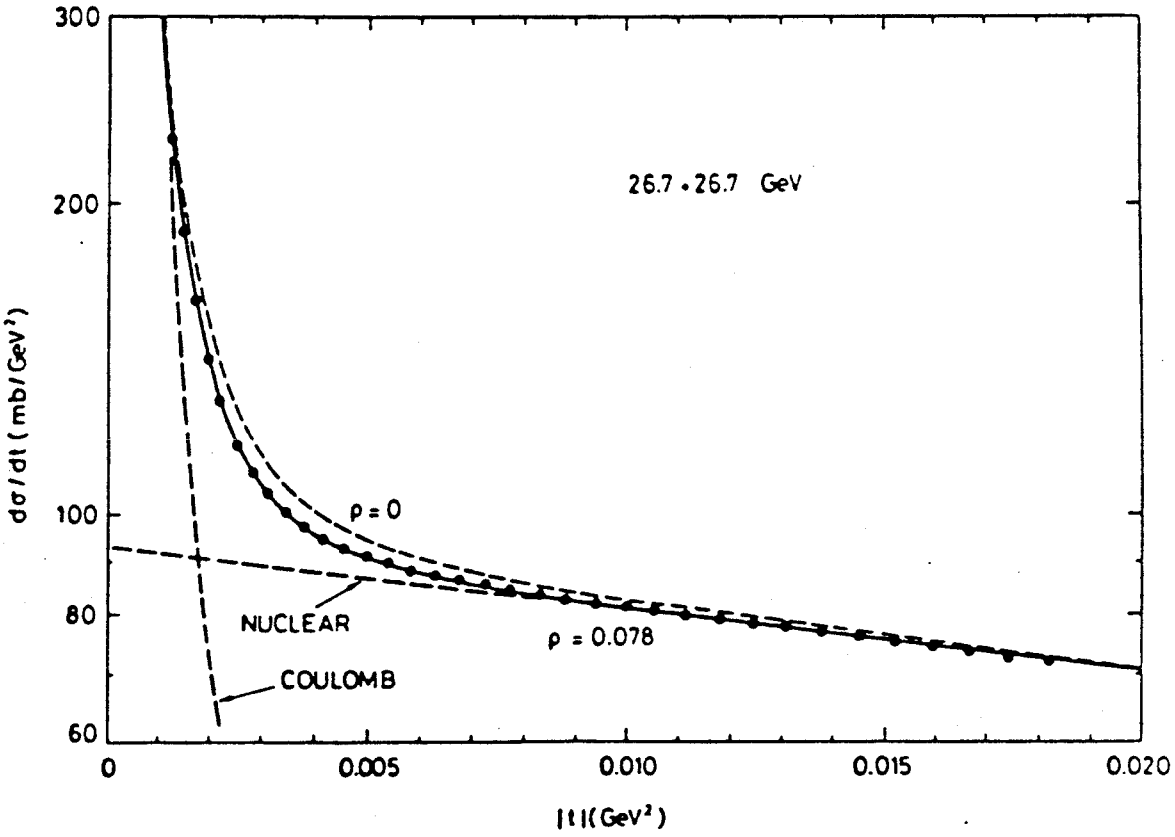

Figure 2.2 Elastic differental cross section for pp at $\sqrt{s}$ = 53.4 GeV (Plot from Ref. 2.4, data from Ref. 2.5). The fit to the data points used Equ. 2.16.

$$|t|_{int} \approx \frac{8\pi\alpha}{\sigma_{tot}} = \frac{0.071}{\sigma_{tot}(mb)} \quad \text{for t in } (GeV/c)^2. \tag{2.17}$$

For $\sqrt{s}$ = 24.3 GeV, this occurs around $|t|_{int} = 0.0017\ (GeV/c)^2$.

2.2 Measurement of Elastic Scattering

The differential cross section cannot, of course, be measured directly. What one measures is a counting rate and its variation by energy or angle. In this experiment, the quantity measured is $\Delta N(t)$, the number of elastic counts/sec/Δt entering the detector within a Δt interval around t, corrected for background and detector inefficiencies. The rate is normalized to get $d\sigma/dt$ as

$$\frac{d\sigma}{dt} = A \cdot \Delta N(t) \tag{2.18}$$

where the normalization factor A includes the luminosity L and the detector solid angle. For the circular "stack" detectors, this becomes in the laboratory frame

$$\frac{d\sigma}{dt} = \frac{\Delta N}{L} \frac{\pi}{2m\ d\Omega \sqrt{|t|}} \tag{2.19}$$

where $|t|$ is the value at the weighted center of the $|t|$ region covered by the detector and $d\Omega$ is the detector solid angle coverage. In the case of the rectangular position sensitive detector the continuous measurement is

finely divided into intervals of Δt based on the energy measurement. For a particular interval

$$\frac{d\sigma}{dt} = \frac{\Delta N}{L} \frac{2\pi}{d\phi\ \Delta t} \tag{2.20}$$

where $d\phi$ is the azimuthal coverage of the detector. For the stack detectors, the relative geometrical acceptance among the different angles of measurement can be calculated and the detector inter-normalization measured by a procedure described in a later section. However, the inter-normalization between the position sensitive detector and the stacks as well as the absolute solid angle coverage could only be approximately determined. Therefore, in the final fit of the data to the functional form of the differential cross section (Eq. 2.16), the absolute normalization to the total cross section for the stacks and for the position sensitive detector will in each case be left as an independent free parameter.

Following kinematic and geometrical considerations, the factor which relates the observed counting rate to the cross section is the luminosity, L, which has units of $[\text{area}\cdot\text{sec}]^{-1}$. For a stationary target like the gas jet, the luminosity is the product of the flux of incoming particles and the area density of the jet. The luminosity varies with beam and jet conditions so it must be monitored with fixed detectors called luminosity monitors. These detectors measure the integrated luminosity which has units of $[\text{area}]^{-1}$. Since the luminosity monitors use the same triggering electronics

as the main detector array, apparatus dead-time will be divided out when data from different runs are combined.

CHAPTER 3 Discussion of Theory

3.1 Asymptotic Theorems

At sufficiently high energies, the features of hadronic scattering can be interpreted in terms of a few general principles of scattering theory, independent of specific models. Asymptotic properties of scattering amplitudes can be derived from the requirements of unitarity, analyticity and crossing symmetry. This approach has led to several theorems which constrain hadronic behavior at high energies.

3.1.1 Froissart-Martin Bound

Before the discovery of the rising total cross section, Froissart [3.1] had established an upper bound on the rate of increase of the total cross section with energy. This bound can be derived from axiomatic field theory [3.2] and states that

$$\sigma_{tot} \leq \frac{\pi}{m_\pi^2} \left[\ln(s/s_0) \right]^2 \approx 60 \text{ mb} \left[\ln(s/s_0) \right]^2 \qquad (3.1)$$

where m_π is the pion mass and s_0 is an unknown scale. It has been proven that this expression gives a minimum upper bound which cannot be further restricted under the original theoretical assumptions.

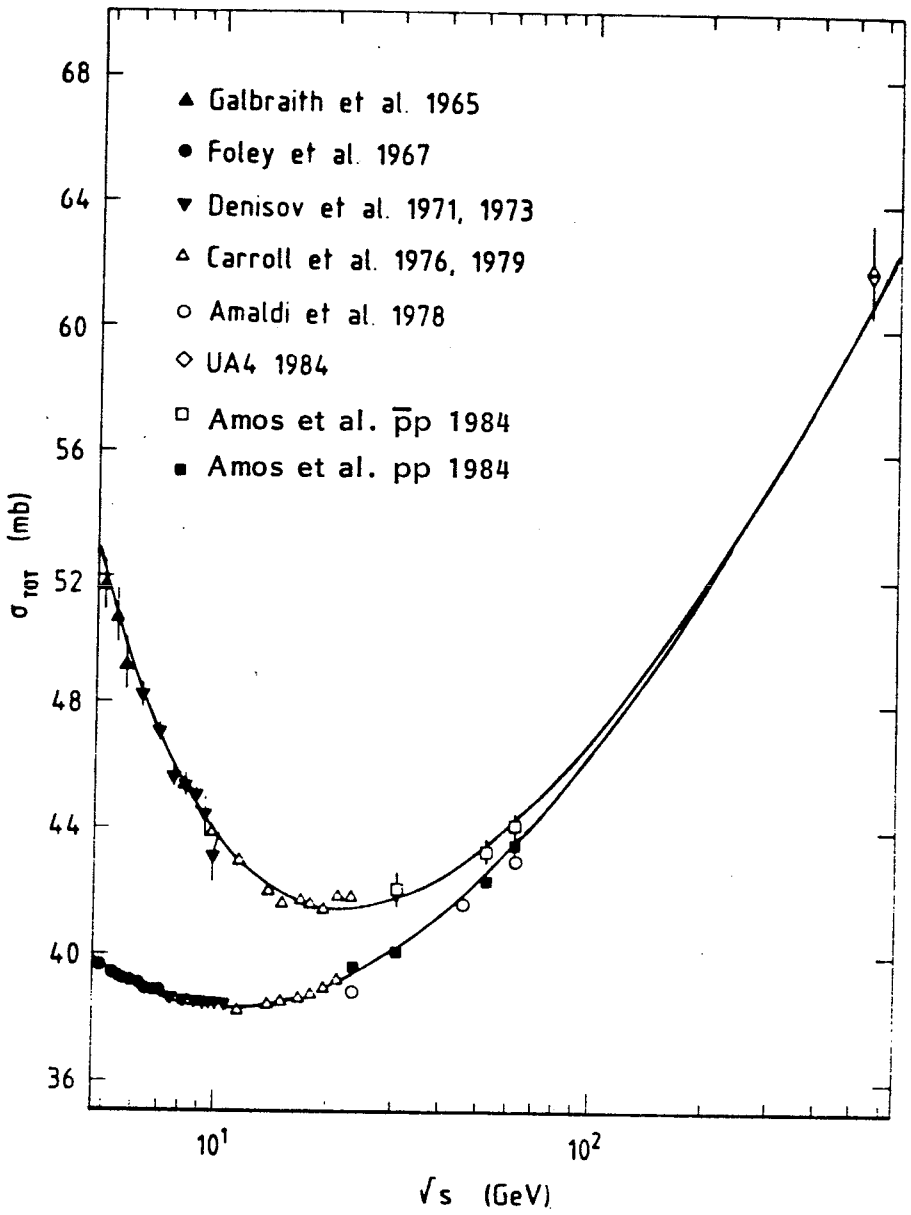

Figure 3.1 Total cross section data for pp and $\bar{p}p$ scattering. The curves correspond to the dispersion relation fit of Ref 3.14.

3.1.2 Pomeranchuk Theorem

One observes that $\sigma_{tot}(pp)$ and $\sigma_{tot}(\bar{p}p)$ approach each other more and more as energy increases (Figure 3.1). When it was thought that the total cross section was descending to a constant, Pomeranchuk [3.3] derived a theorem based on dispersion relations for the forward scattering amplitude that stated that if the total cross sections of particle and antiparticle tend to a constant with increasing energy their difference goes to zero. But this formulation is of no use for dealing with the rising total cross section discovered at the ISR. Instead it was shown [3.4] that if the pp and $\bar{p}p$ cross sections grow as $[\ln(s/s_0)]^{\gamma}$, then their difference

$$\Delta\sigma = \sigma_{tot}(\bar{p}p) - \sigma_{tot}(pp) \tag{3.2}$$

cannot rise faster than $[\ln(s/s_0)]^{\gamma/2}$. This formulation implies that

$$\lim_{s\to\infty} \frac{\sigma_{tot}(\bar{p}p)}{\sigma_{tot}(pp)} \to 1 \tag{3.3}$$

rather than a vanishing $\Delta\sigma$; in fact, $\Delta\sigma$ could even go to infinity as energy increases.

The possibility of a non-vanishing $\Delta\sigma$ has drawn attention to models which include significant odd-under-crossing ('odderon') contributions at high energy. These would cause persistent differences between pp and $\bar{p}p$

scattering as allowed by (3.3). Defining the even/odd-under-crossing amplitudes as

$$f_{\pm} = \frac{1}{2} \left(f(\bar{p}p) \pm f(pp) \right)\Big|_{t=0} , \tag{3.4}$$

which are related to the cross sections $\sigma_{\pm} = \sigma_{tot}(\bar{p}p) \pm \sigma_{tot}(pp)$ by the optical theorem

$$\sigma_{\pm} = 4\pi \, \mathrm{Im} \, f_{\pm}(0) , \tag{3.5}$$

one obtains $\Delta\sigma \sim \mathrm{Im} \, f_{-}(0)$, showing the relevance of odd-under-crossing amplitudes to the cross section difference. In terms of Eq. 3.4, the parameter ρ is then written as

$$\rho(pp/\bar{p}p) = \frac{\mathrm{Re} \, f_{+}(t=0) \pm \mathrm{Re} \, f_{-}(t=0)}{\mathrm{Im} \, f_{+}(t=0) \pm \mathrm{Im} \, f_{-}(t=0)} . \tag{3.6}$$

Models have been studied in which the odd-under-crossing contribution to $\Delta\sigma$ remains constant [3.5] or grows as ln s [3.6] with increasing energy. Experimentally, Im $f_{-}(t=0)$ is now thought to be negligible compared to Im $f_{+}(t=0)$, so an additional odderon model has the amplitude f_{-} affect the behavior of ρ through the real part. With an eye on the UA4 $\rho(\bar{p}p)$ value, Re $f_{-}(t=0)$ has to be negative and of the same order of magnitude as Re $f_{+}(t=0)$ at $\sqrt{s} = 546$ GeV [3.7]. The Fischer theorem [3.8] states that $\Delta\sigma$ must go to zero if asymptotically Re f_{-} and Im f_{-} have the same sign.

Therefore, this model requires Im f_- to be positive which by Eq. 3.5 predicts that $\sigma_{tot}(pp)$ must exceed $\sigma_{tot}(\bar{p}p)$ somewhere above ISR energies.

3.1.3 Cornille-Martin Theorem and Corollaries

The Pomeranchuk theorem was applied to elastic scattering when it was recognized [3.9] that analyticity and unitarity imply that the ratio of the forward elastic differential cross section of particle and antiparticle should tend to unity as energy increases. Cornille and Martin [3.10] have shown that this property may be extended to cover the entire diffraction peak, that is,

$$\lim_{s\to\infty} \frac{d\sigma(\bar{p}p)/dt}{d\sigma(pp)/dt} \to 1 \ . \tag{3.7}$$

A consequence of this theorem is that

$$\lim_{s\to\infty} \frac{b(\bar{p}p)}{b(pp)} \to 1 \tag{3.8}$$

and Block and Cahn [3.11] have shown that

$$\lim_{s\to\infty} \left(\frac{\rho(\bar{p}p)}{\rho(pp)} \right)^2 \to 1 \tag{3.9}$$

leaving the possibility that asymptotically the values of ρ may have opposite sign.

3.2 Dispersion Relations

Results in elastic scattering are often interpreted with the help of dispersion relations which express the real part of an analytic function as an integral over its imaginary part. In particular, when the energy is much greater than the threshold for scattering (far from the poles in the 'unphysical' region) the predictions of the dispersion relations become more reliable and easier to calculate. This assumes that the physical amplitude for elastic scattering, $f(E,t)$, has an analytic continuation to a more general function, $\Phi(E,t)$, in which E and t may take on complex values. The pp amplitude is then a limit of $\Phi(E,t)$ while the $\bar{p}p$ amplitude is another limit of the same analytic function.

Since $\Phi(E,t)$ is analytic on the cut E plane, then Cauchy's integral formula is applicable:

$$\Phi(E,t) = \frac{1}{2\pi i} \int_C \frac{\Phi(E',t)}{E'-E}\, dE' \tag{3.10}$$

where the contour is shown in Figure 3.2. Taking the real part of both sides leaves the relation

$$\text{Re } f(E,t) = \frac{1}{2\pi} \int_C \frac{\text{Im } f(E',t)}{E'-E}\, dE' \ . \tag{3.11}$$

If the forward amplitude (t=0) is considered, then the optical theorem relates the imaginary part of $f(E,t=0)$ to the total cross section where here

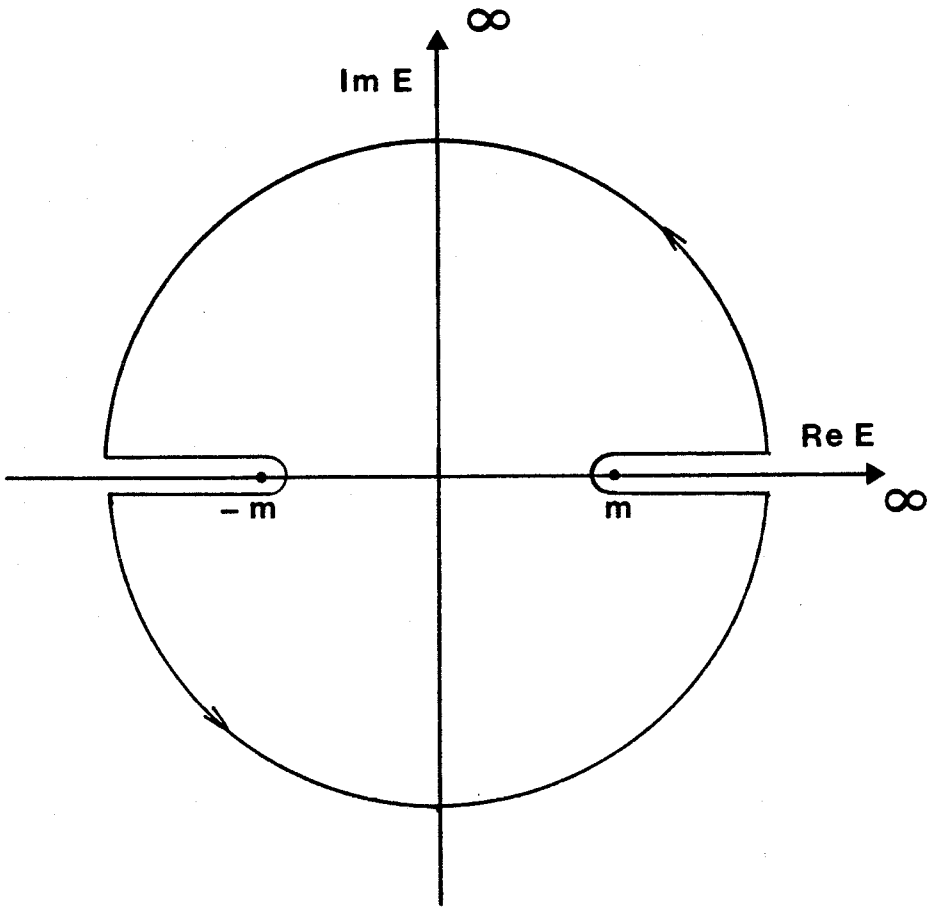

Figure 3.2 Contour of integration in the complex E plane used for evaluation of dispersion relations.

the normalization is Im $f(E,0) \approx (Em/8\pi)\ \sigma_{tot}(E)$. In order to assure convergence on the circle at $|E| = \infty$, a subtraction is made at $E = m$. Crossing symmetry relates Im $f_{pp}(-E)$ to Im $f_{\bar{p}p}(E)$ giving the once subtracted dispersion relations for pp and $\bar{p}p$ [3.12]

$$\text{Re } f_{pp}(E) = C + \frac{Em}{8\pi^2} \int_m^\infty dE' \left\{ \frac{\sigma_{pp}(E')}{E'-E} - \frac{\sigma_{\bar{p}p}(E')}{E'+E} \right\} \tag{3.12}$$

$$\text{Re } f_{\bar{p}p}(E) = C + \frac{Em}{8\pi^2} \int_m^\infty dE' \left\{ \frac{\sigma_{\bar{p}p}(E')}{E'-E} - \frac{\sigma_{pp}(E')}{E'+E} \right\} \tag{3.13}$$

where C is a constant to be determined and the principal value of the integral is implied. If the cross section difference does not go to zero at large E, then the twice subtracted odd dispersion relations must be used.

At high energies where the cross sections are generally smooth, it is possible to obtain a quasilocal connection between the ratio ρ and the total cross section that can be exploited assuming that the cross sections are well described by a simple function. Such a differential dispersion relation is

$$\rho(s) \approx \frac{\pi}{2\sigma_{tot}} \cdot \frac{d\sigma_{tot}}{d(\ln s)} \tag{3.14}$$

which can be used to describe in a qualitative way the relation between ρ and σ_{tot} at asymptotic energies. Thus a constant cross section implies $\rho = 0$, while a rising σ_{tot} results in a positive value of ρ and a decreasing

σ_{tot} in a negative value. For example, for asymptotic behavior which saturates the Froissart bound ($\sigma_{tot} \sim \ln^2 s$), ρ goes to zero from positive values as $\pi/\ln s$. These conditions were rigorously proved in 1965 by Khuri and Kinoshita [3.13].

To apply dispersion relations, one first parametrizes the pp and $\bar{p}p$ total cross sections with a functional approximation. The values of ρ are then predicted, up to a constant, by dispersion relations. Then a chi-squared minimization fit to σ_{tot} and ρ data at the same time constrains the parameters describing the cross sections.

Amaldi et al. [2.5] followed such a course analyzing ISR pp and existing $\bar{p}p$ cross sections up to $\sqrt{s} \sim 15$ GeV using singly subtracted relations (3.12) and (3.13). They used a parametrization of the type

$$\sigma_{\bar{p}p/pp} = C_0 + C_1 E^{-\alpha_1} \pm C_2 E^{-\alpha_2} + C_3[\ln(s/s_0)]^{\gamma} \qquad (3.15)$$

where E is in GeV and s in GeV^2. (The upper sign is for $\bar{p}p$, the lower for pp.) The authors arbitrarily fixed s_0 to 1 GeV^2 and did not fit the available data for $\rho_{\bar{p}p}$. Since then, higher energy measurements have become available for the $\bar{p}p$ system as well. For a fit using dispersion relations with the parametrization of Eq. 3.15, spanning pp and $\bar{p}p$ data from 10 GeV through Collider energies, and with s_0 set to unity as well, Amos et al. [3.14] quote the following results: $C = -30.0 \pm 3.8$, $C_1 = 43.0 \pm 0.6$, $C_2 = 24.8 \pm 0.9$, $C_3 = 0.19 \pm 0.01$, $C_0 = 28.3 \pm 0.2$, $\alpha_1 = 0.41 \pm 0.01$, $\alpha_2 = 0.56 \pm 0.01$, and

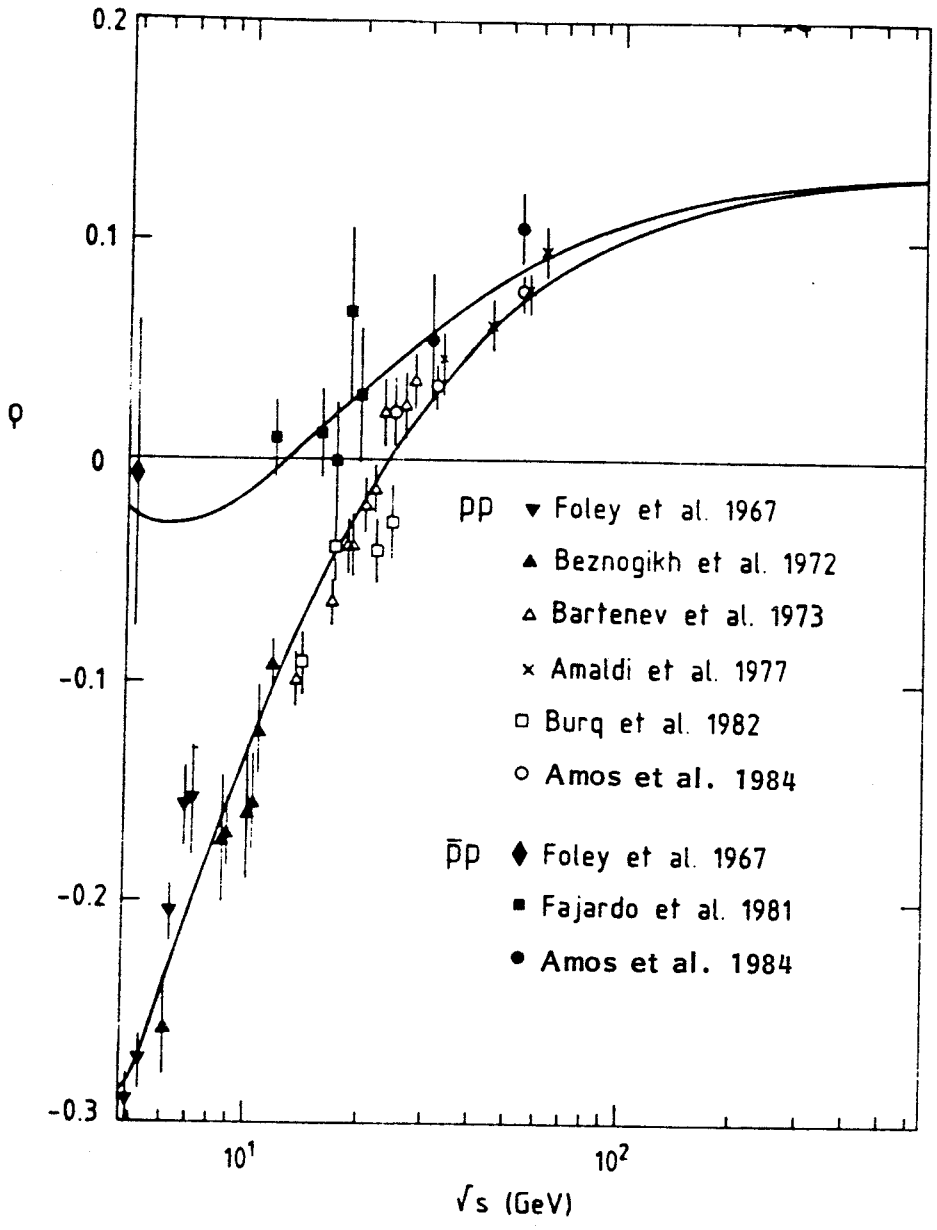

Figure 3.3 Compilation of $\rho(pp)$ and $\rho(\bar{p}p)$ values.

$\gamma = 2.02 \pm 0.01$. These are the curves shown in Figure 3.1 for the total cross sections and in Figure 3.3 for the ρ parameter. Note that the value of γ shows the Froissart bound to be qualitatively saturated but with a coefficient, 0.19 mb, much less than the 60 mb implied in (3.1). In this parametrization,

$$\Delta\sigma = 2C_2 \, E^{-\alpha_2} \tag{3.16}$$

so the value of α_2 suggests the cross section difference may be dropping as $1/\sqrt{s}$. Note that the possibility of odderon terms which are allowed by analyticity were not considered.

3.3 Analytic Parametrizations

By the description of scattering amplitudes via the direct use of analytic functions having the required properties of unitarity and crossing symmetry, it is possible to circumvent the difficulties of integral and differential dispersion relations. Once the functional form of the cross sections has been specified, hence giving the imaginary part of the amplitude, dispersion relations provide only the missing real part. By parametrizing this with an analytic representation, the necessary long numerical integrations may be avoided.

This technique was first used by Bourrley and Fischer [3.15] then applied to more extensive data by Block and Cahn in detailed studies [3.11,

3.16]. The simplest form of their amplitude parametrizations yield the following functional forms for the total cross sections and the ratios ρ:

$$\sigma_{pp/\bar{p}p} = A + \beta\left[\ln^2 \frac{s}{s_0} - \frac{\pi^2}{4}\right] + C\cdot\sin\left(\frac{\pi\mu}{2}\right) s^{\mu-1} \pm D\cdot\cos\left(\frac{\pi\mu}{s}\right) s^{\alpha-1} \qquad (3.17)$$

$$\rho_{pp/\bar{p}p} = \frac{1}{\sigma_{pp/\bar{p}p}} \left\{\beta\pi\ln \frac{s}{s_0} - C\cdot\cos\left(\frac{\pi\mu}{2}\right) s^{\mu-1} \pm D\cdot\sin\left(\frac{\pi\mu}{s}\right) \right\} . \qquad (3.18)$$

For a simultaneous fit to pp and $\bar{p}p$ data through ISR energies they find, setting $\mu = 0.5$, excellent agreement using the following parameter values: $A = 41.30\pm0.28$, $\beta = 0.62\pm0.03$, $s_0 = 294\pm28$, $D = -40.5\pm1.8$, $\alpha = 0.47\pm0.01$ and $C = 8.3\pm5.1$. The authors also tested various odderon terms and found that such a contribution could be at most about 1% in comparison to the constant amplitude A.

Block and Cahn have also examined the forward slope parameter, b. Writing the nuclear differential cross section as

$$\frac{d\sigma}{dt} = \frac{\pi}{p^2}\left| f_+\cdot e^{-b_+|t|/2} + f_-\cdot e^{-b_-|t|/2} \right|^2 \qquad (3.19)$$

where p is the laboratory momentum, they parametrize separately the slopes associated with the even and odd parts of the amplitude as

$$b_+ = C_+ + D_+ \ln(s) + E_+ \ln^2(s). \qquad (3.20)$$

$$b_- = C_- + D_- \ln(s) \ . \tag{3.21}$$

Then by using

$$b(t=0) = \frac{d}{dt} \ln \left. \frac{d\sigma_n}{dt} \right|_{t=0} \tag{3.22}$$

they extract values for the slope as

$$b_{pp/\bar{p}p} = b_+ \pm \frac{\sigma_-}{\sigma_+} \cdot (b_- - b_+) \ . \tag{3.23}$$

Their most recent fit made to data including measurements from Collider energies [3.17] gave the following results: $C_+ = 9.6 \pm 0.8$, $D_+ = 0.34 \pm 0.2$, $E_+ = 0.0089 \pm 0.011$, $C_- = 21.7 \pm 18$, and $D_- = 1.35 \pm 3.0$, all in GeV^{-2}.

CHAPTER 4 Description of the Experiment

4.1 SPS as $p\bar{p}$ Collider

In 1976, the same year as the CERN Super Proton Synchotron (SPS) came into operation, Rubbia, Cline and McIntyre [4.1] proposed to transform the machine into a proton-antiproton collider ($Sp\bar{p}S$) at 270 GeV/c per beam, capable of directly producing the intermediate vector bosons (IVB) $W^{\pm}$ and Z^0 by the interaction of a quark and an antiquark from counter-rotating protons and antiprotons. This conversion, essentially a "short-cut" to IVB production rather than building an entirely new machine, was made possible by the method of limiting the momentum spread of anitprotons produced at a target known as "stochastic cooling" invented by Simon van der Meer in 1968 [4.2] and successfully tested at the ISR in 1975.

Full approval of the Collider project came in 1978, taking advantage of CERN's existing inter-connected accelerator rings (Figure 4.1). A new component, the Antiproton Accumulator (AA), was added to store and cool the antiprotons (Figure 4.2). Additional pumps were needed to improve the vacuum within the SPS beam pipe from 10^{-8} torr to 10^{-9} torr and quadrupole magnets were added to squeeze the beams at the intersection regions. Antiprotons are produced by directing a 26 GeV/c beam from the Proton Synchotron (PS), serving CERN since 1959, onto a metal target, yielding a shower of hadrons. Antiprotons are extracted every 2.4 seconds at 3.5 GeV, the energy of their greatest yield, and transferred to the AA, where they

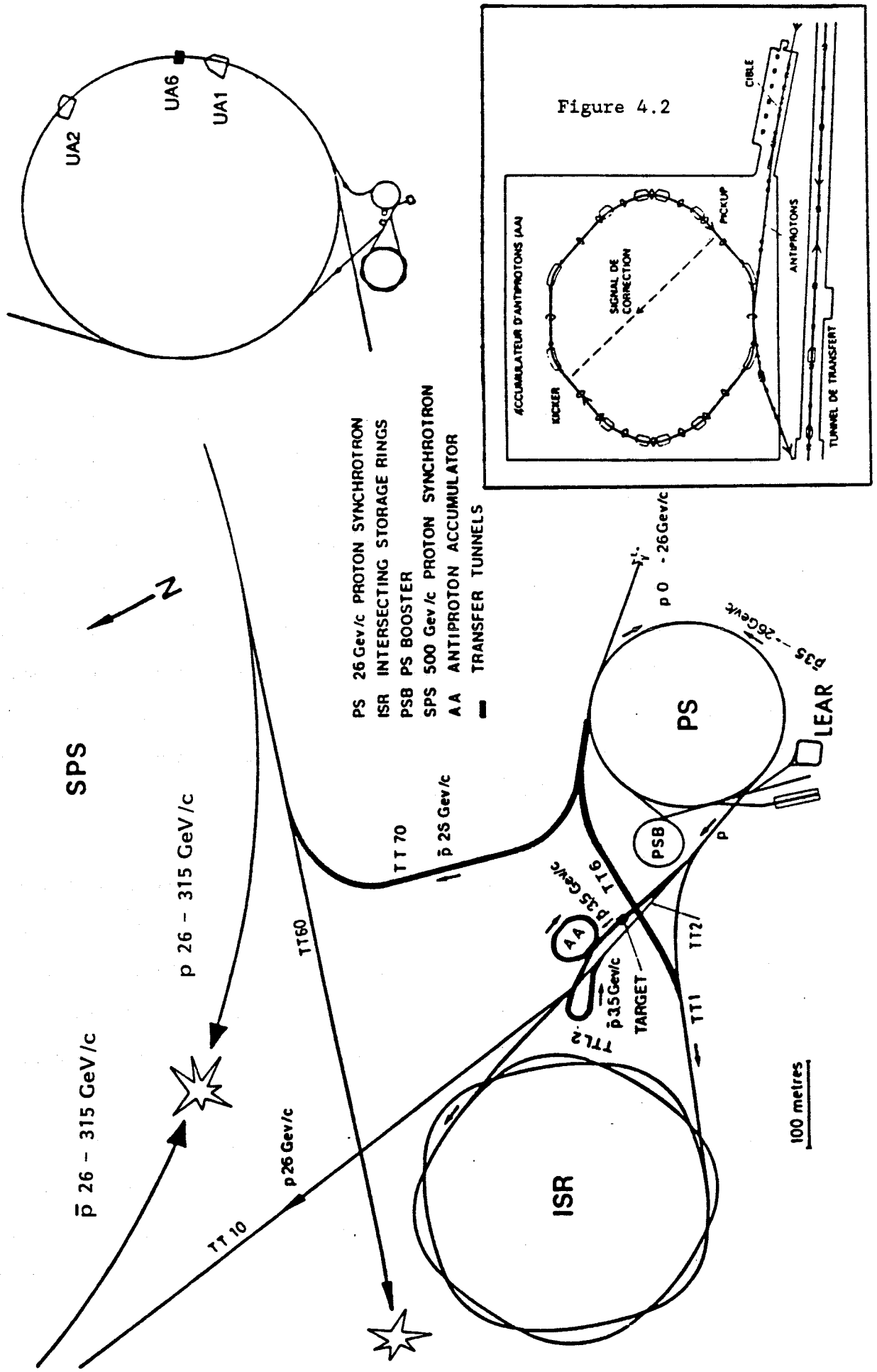

Figure 4.1 and 4.2 CERN SPS in collision mode and Antiproton Accumlator.

join antiprotons previously injected. From each pulse of ~10^{13} protons from the PS, only about 2 x 10^{7} antiprotons are added to the AA. Thus to fill the AA with 6 x 10^{11} particles requires all the beam spills from the PS during a period of about twenty-four hours.

Cooling begins when signals from electrodes in the AA which sense the average position of the antiprotons are sent across the ring where an electric field "kicks" some of then to a more optimal momentum while others are lost (hence the appellation "stochastic"). This process is repeated over a period of two seconds reducing the momentum spread from 0.75% to 0.1%, then this bunch is "stacked" within the ring with the other previously cooled bunches.

When the AA is filled, antiprotons comprising the dense core are extracted and sent back to the PS which accelerates them to 26 GeV/c. They are then injected into the Sp$\bar{p}$S which has already been filled with protons circulating in the opposite direction and both beams are accelerated to 315 GeV/c, the Collider energy since 1984. The beams thereupon consist of three packets each of ~10^{10} antiprotons and ~10^{11} protons of about 4 ns in duration separated by 7.68 μs colliding at six well-defined points.

4.2 General Description of Experiment UA6

At two of the interaction points of the counter-rotating proton and antiproton beams of the CERN Sp$\bar{p}$S ($\sqrt{s}$ = 630 GeV/c) are the large experiments

UA1 and UA2, between which UA6 (Underground Area, Number 6) works as a fixed-target experiment at $\sqrt{s}$ = 24.3 GeV/c when the accelerator operates in collision mode [4.3]. It is situated as seen in Figure 4.1 in the medium straight section (MSS) 514 of the SPS tunnel. Since this is not an intersection point, the beams pass at different times, the $\bar{p}$ bunch following the p bunch about 690 ns later. Figures 4.3 and 4.4 give a global view in perspective and in projection of the experimental installation. UA6 is really two separately triggering experiments which simultaneously use the same internal cluster-jet target. One experiment consists of a double-armed magnetic spectrometer of a length of about 10 meters downstream from the jet interaction point [4.4]. The other is the recoil arm of solid state detectors mounted on the jet housing perpendicular to the beam-crossing point.

Each arm of the magnetic spectrometer is composed of the following: an electromagnetic calorimeter with a triggering hodoscope, a transition radiation detector [4.5], a dE/dx proportional wire chamber, a magnet with a 2.2 T·m field integral and a set of five multiwire proportional chambers for charged particle tracking. To allow the comparison of pp and $p\bar{p}$ interaction with the same apparatus, the spectrometer may be dismounted and turned 180° during a period of three to four weeks. Among the reactions studied are the e^+e^- pair continuum, J/ψ production and large-p_T π^0 [4.6] and single γ production [4.7]. The spectrometer has no relevance to the elastic scattering measurement and will be discussed no further.

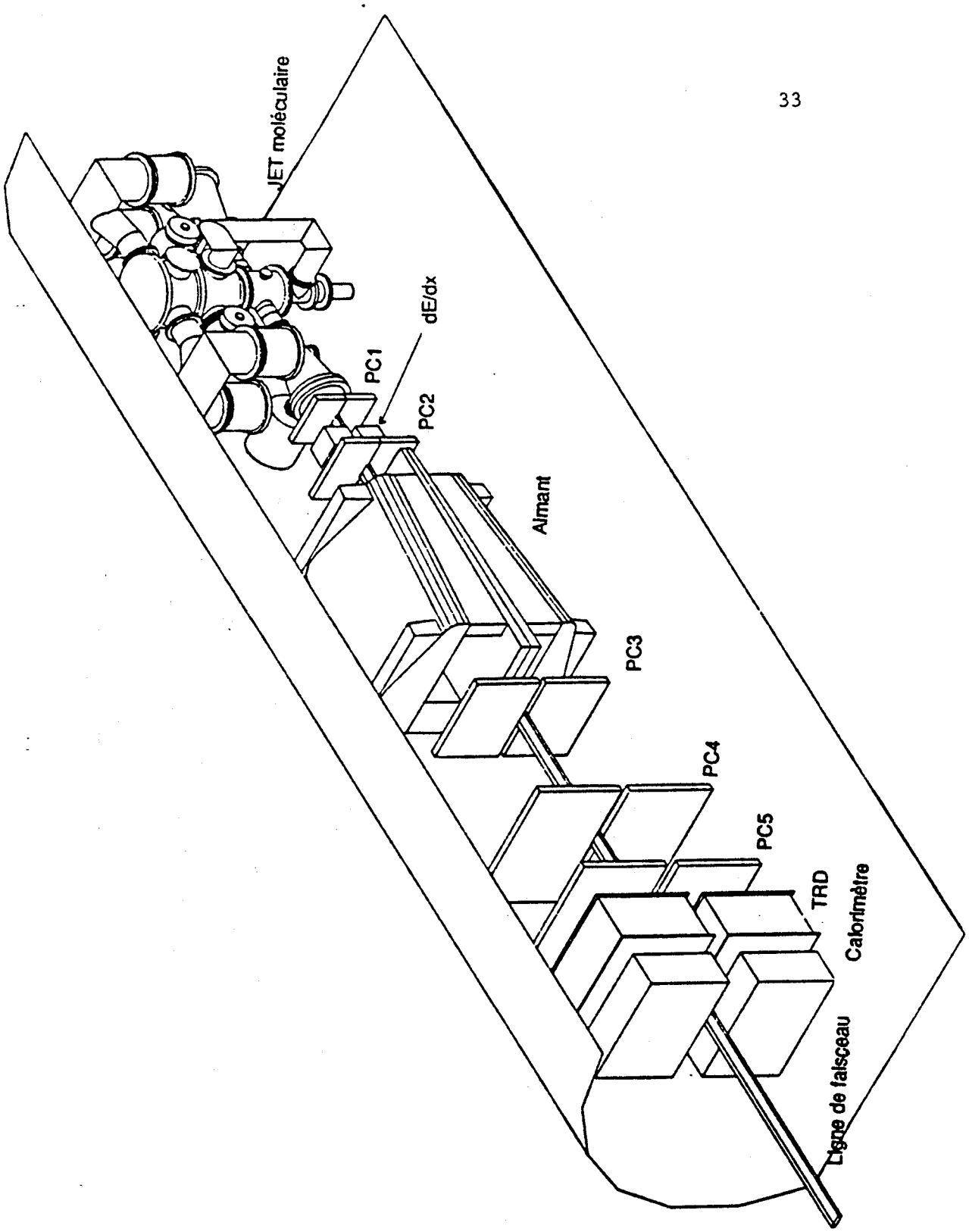

Figure 4.3 Experiment UA6 perspective view.
Jet target and magnetic spectrometer in the SPS tunnel.

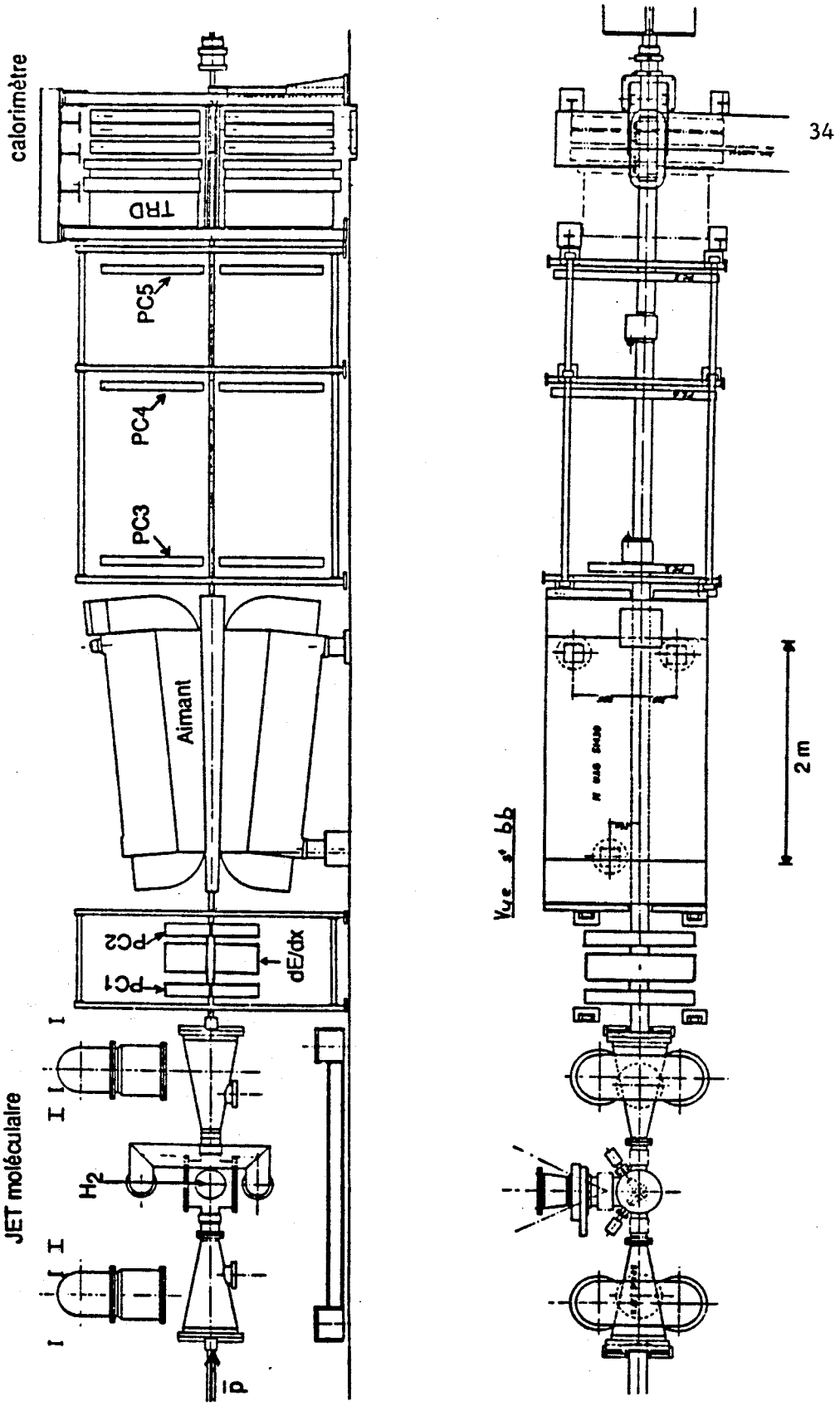

Figure 4.4 Side and top views of Experiment UA6 (projection view).

4.3 The Hydrogen Cluster-Jet Target

The UA6 target is a low density jet [1.10] of molecular hydrogen that crosses through the colliding beams and is immediately pumped away. This method has several advantages in comparison to conventional fixed target experiments:

i) the accelerated particles are used efficiently;

ii) the parasitic operation means that no specific beam allocation is normally required;

iii) source size is small and well defined, about 8 mm along the beam axis and 3 mm across;

iv) the low density of the target makes multiple Coulomb scattering negligible and allows detection of very low energy secondary particles such as recoil protons;

v) a high luminosity is obtained by multiple traversal of the beam particles.

The jet is operated at densities up to $\rho_{jet} = 4.0 \times 10^{14}$ nucleons/cm^3 with typically 4.0×10^{10} antiprotons circulating in three bunches giving an instantaneous luminosity

$$L_{p\bar{p}} = \rho_{jet} \cdot \ell_{jet} \cdot N_{\bar{p}} \cdot \nu_{rev} = 5.5 \times 10^{29} \text{ cm}^{-2} \text{ s}^{-1}$$

where $\ell_{jet} = 0.8$cm is the length of the jet interaction and the beam revolution frequency is $\nu_{rev} = 4.34 \times 10^4$ s^{-1}. The pp luminosity is about a factor of 10 higher.

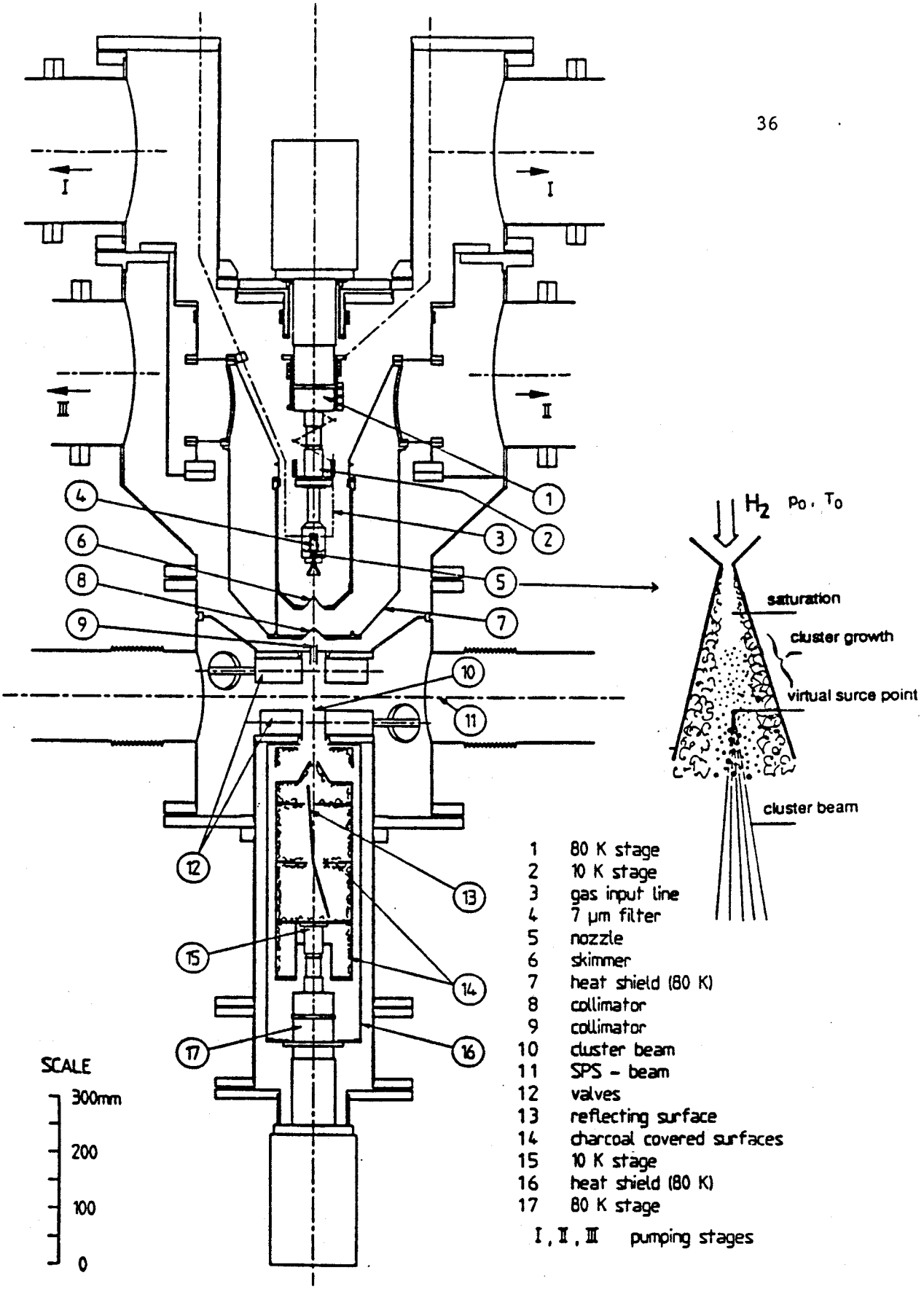

Figure 4.5 The molecular hydrogen cluster-jet target and nozzle.

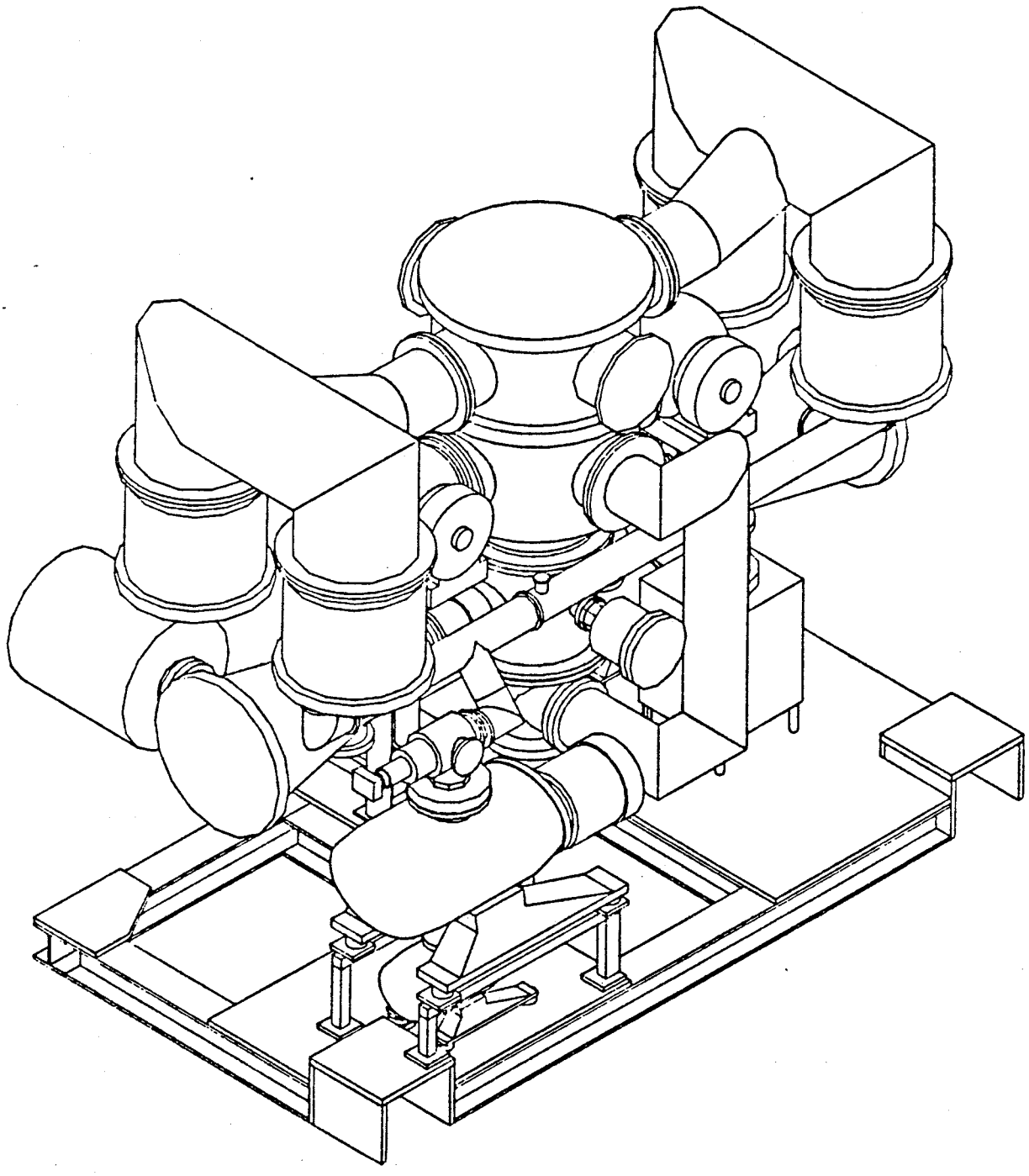

Figure 4.6 Perspective view of jet housing and turbomolecular pumps.

The principle of operation of the condensed molecular jet as invented by E. W. Becker and collaborators [4.8] is illustrated by Figure 4.5. Gas enters the throat of the nozzle (diameter ~0.1 mm) through a palladium filter with an input pressure p_0 of a few atmospheres and a temperature T_0 of 20-30° K, then expands adiabatically, decreasing in pressure and temperature. As saturation condition is reached, small clusters are formed and continue to grow as long as they remain in the divergent part of the nozzle. After leaving the nozzle, the clusters of about 10^6 molecules form a beam with a divergence of about half the solid angle of the nozzle, and consisting of about 2 to 10% of the injected gas.

A system of rectangular diaphrams extracts this central core, which has the required shape at the crossing of the accelerator beams. Owing to their great mass, the clusters are scattered practically not at all by background gas, and the jet keeps a well defined boundary.

Since only a small fraction of the total gas input goes into useful target material, the rest has to be pumped away. The differential stages of jet production use four large turbomolecular pumps comprising most of the jet housing schematic of Figure 4.6. After passing through the beams, the jet is dumped into a cryopump, which keeps the vacuum of the $Sp\bar{p}S$ to the required 2×10^{-7} mbar in the vicinity of the jet. (The lowest pressure in the $Sp\bar{p}S$ is 10^{-9} mbar while in the jet it is 10^{-2} mbar.) The cryopump is usually regenerated after ten to twelve hours of use, a procedure which requires four to six hours.

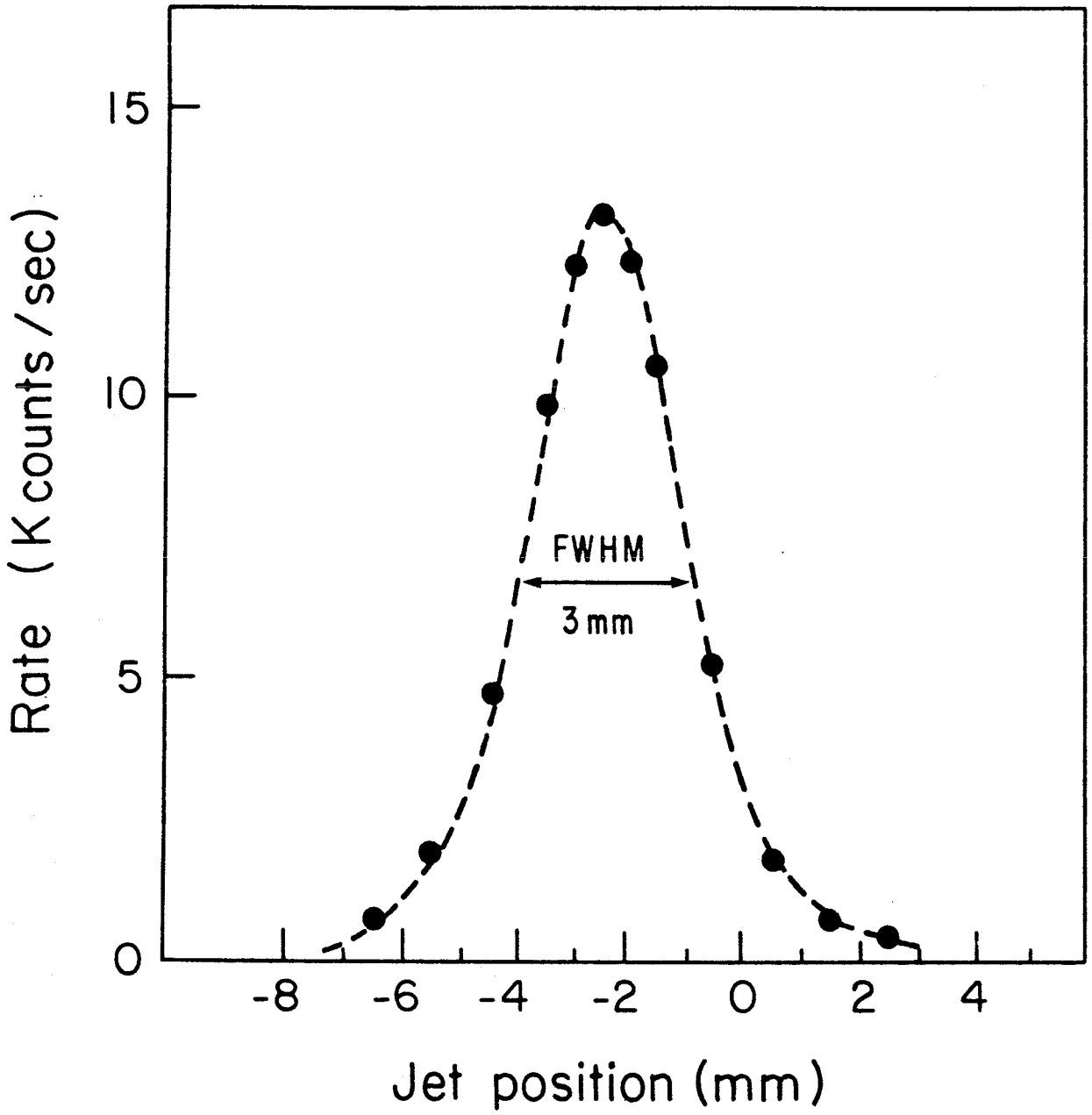

Figure 4.7 Profile of the zone of interaction between the hydrogen jet and the proton beam of the $S\bar{p}pS$.

The jet can be displaced up to 10 mm transverse to the beam in each direction so that the jet/beam interaction position can be optimized for the highest rate. The result of such a scan is given in Figure 4.7 which also then shows a profile of the zone of interaction as a function of the jet position across the beams. The profile is obtained by measuring the rate of triple coincidences in a scintillation counter telescope pointing to the interaction region.

4.4 The Scattering Experiment

Within a moveable vacuum chamber mounted to the jet housing at 90° with respect to the beams is the array of solid state detectors used to measure the elastic and single diffractive differential cross-sections for $p\bar{p}$ and pp as pictured in Figure 4.8. The array consists of a position sensitive detector at lowest t and three sandwiches or stacks of two surface-barrier detectors each at higher t. A fourth stack is available for a running measurement of background particles. Directly opposite is a smaller, fixed vacuum chamber with four solid state detectors, two each facing the proton and antiproton directions, used to provide a continuous luminosity measurement for both the cross-section measurements and the double arm spectrometer experiment. Each vacuum chamber has its own pumping system and can be sealed off from the beam pipe vacuum by means of remote controlled gate valves.

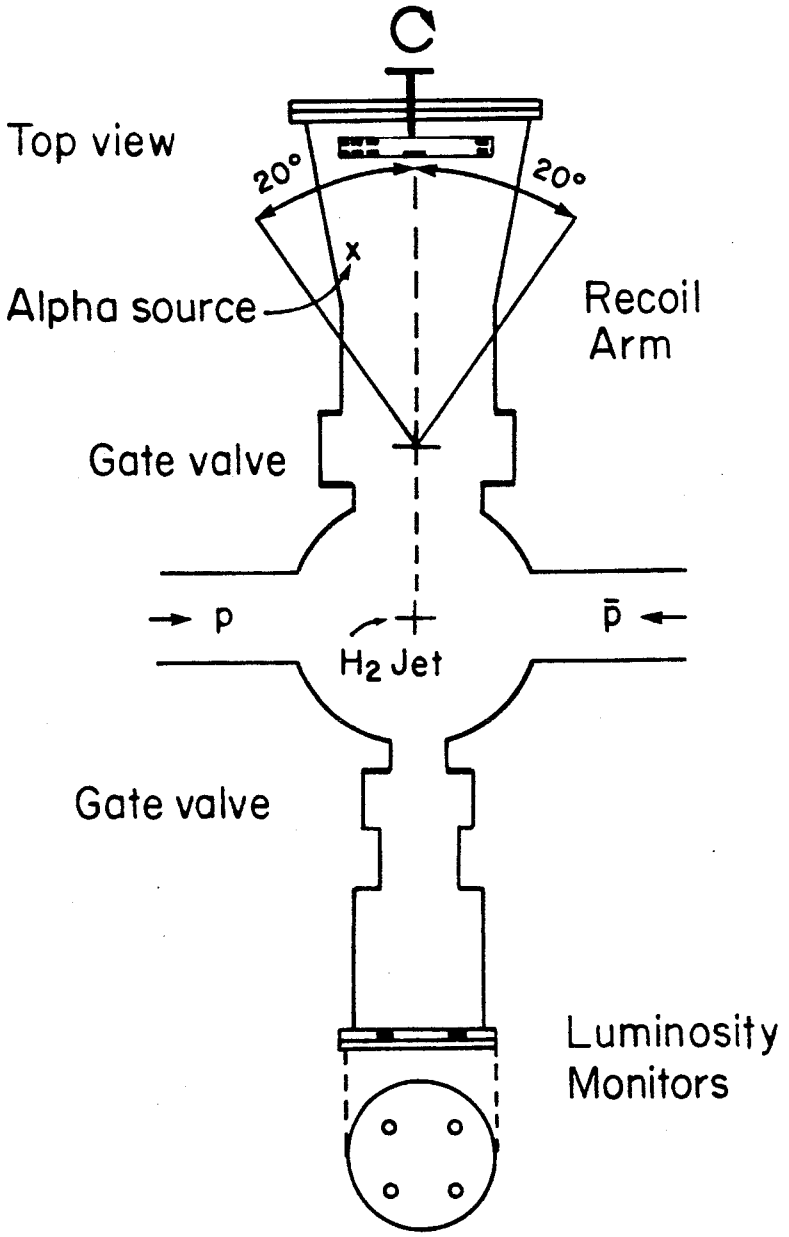

Figure 4.8 Top view of moveable recoil arm and fixed luminosity chamber.

4.4.1 The Solid State Detectors and Recoil Arm

A solid state, or, more precisely, a surface-barrier charged particle detector, is a diode with a very thin evaporated gold (40 $\mu g/cm^2$) contact on an etched n-type, single-crystal silicon wafer [4.9]. The gold evaporation forms the front rectifying contact of the diode and the rear ohmic contact is composed of 40 $\mu g/cm^2$ of evaporated aluminum. When a reverse-bias voltage is applied to the diode an electric field is created which sweeps out any free charge carriers. The region where the field is present is known as the depletion region, which varies according to the applied voltage and the thickness of the detector. The voltages of the detectors in this experiment (Table 4.1) were set to give full depletion of the sensitive depth as specified on the data sheet which accompanied each detector.

Table 4.1 Individual stack detector parameters

Detector	Sensitive Thickness (microns)	Operating Bias (Volts)	Active Area (Nominal) (mm^2)
DE1	1507	200	100
DE2	1499	200	100
DE3	1510	200	100
E1	2982	610	100
E2	3054	450	100
E3	2963	900	100
BDE	1494	350	25
BE	4903	3200	25

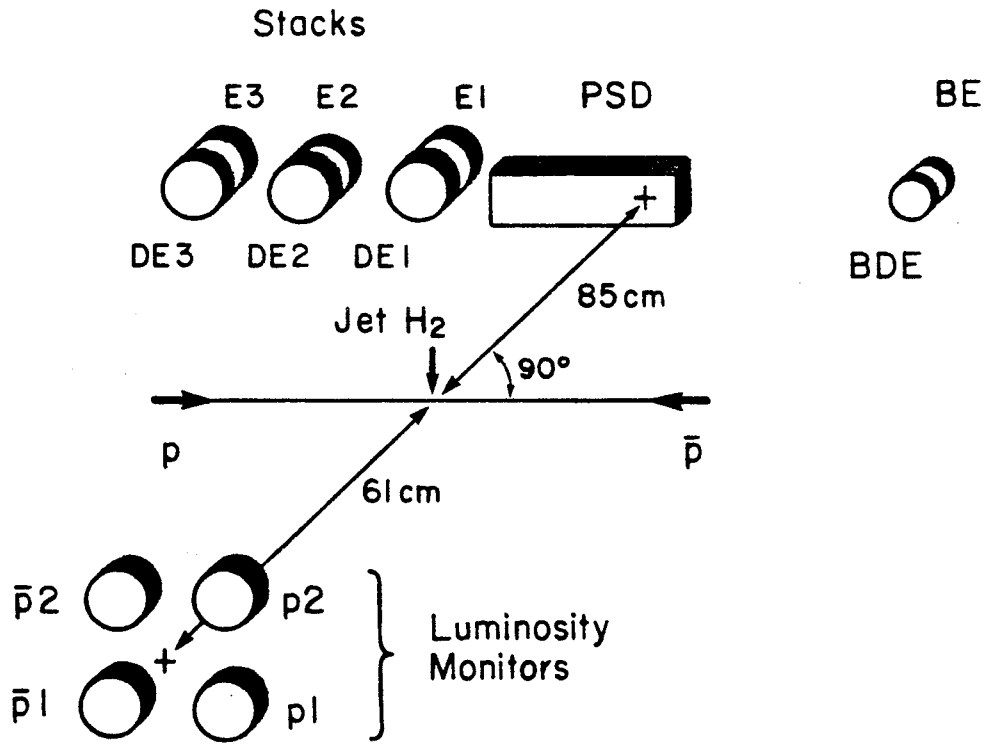

Figure 4.9 Schematic layout of the semiconductor detectors.

When an incident charged particle enters the depletion region, a number of electron-hole pairs are created proportional to the energy lost in the detector (3.6 eV/pair at room temperature). A current pulse is induced when these charge carriers are swept out by the electric field which is integrated by a charge sensitive pre-amplifier. The output voltage pulse, shaped by a filter amplifier, has an amplitude proportional to the energy lost by ionization by the particle in the detector.

The position of the detectors relative to the jet is shown schematically in Figure 4.9. The array of recoil detectors is mounted on an aluminum bar which is in turn mounted on a spindle extending through the mounting plate. By means of a precision stepping motor remote controlled from the experimental control room, the arm may be rotated 180° to intercept recoils from either pp or $p\bar{p}$ scattering. In Figure 4.9, the arm is shown in the $p\bar{p}$ position.

The entire recoil arm chamber may be pivoted from a point 30.5 cm from the interaction point to any angle between 90° and 110° to allow data collection at a variety of angles. The chamber moves along a track beneath it and accordion folds in the chamber walls near the base allow it to bend. It is directed from the jet control barrack where a precise position read-out allows the chamber to be returned repeatedly to the same position. Both the recoil arm and the smaller fixed monitor chamber on the other side may be sealed off from the $Sp\bar{p}S$ vacuum with gate valves. During beam filling and scraping the gate valves are kept closed and may be opened only after

satisfying interlock conditions (satisfactory chamber pressure and SPS Control Room approval).

A ^{241}Am alpha source is mounted outside of the path of the incident recoil protons on the inside top surface of the recoil arm chamber (Figure 4.8) for use in energy calibration of the DE detectors and the PSD. A small motor, controlled remotely, turns the source toward the detector array for calibration and away for running with beams, where the angle of rotation is carefully adjusted so that alpha particles can travel through both open gate valves to the other chamber to provide a running calibration of the luminosity monitors. In addition, a source is mounted in a fixed position behind each E detector so that these detectors are calibrated with the alpha particles entering through the rear window.

4.4.2 The Position Sensitive Detector

The most crucial element of the solid state detector array is the position sensitive detector (PSD). A PSD [4.10] is in most respects like an ordinary solid state detector, but in addition to providing information about the energy of an incident particle, it also locates the point of entry into the detector. While in an ordinary semiconductor detector both front and back contacts are good conductors, in a PSD one contact is made resistive.

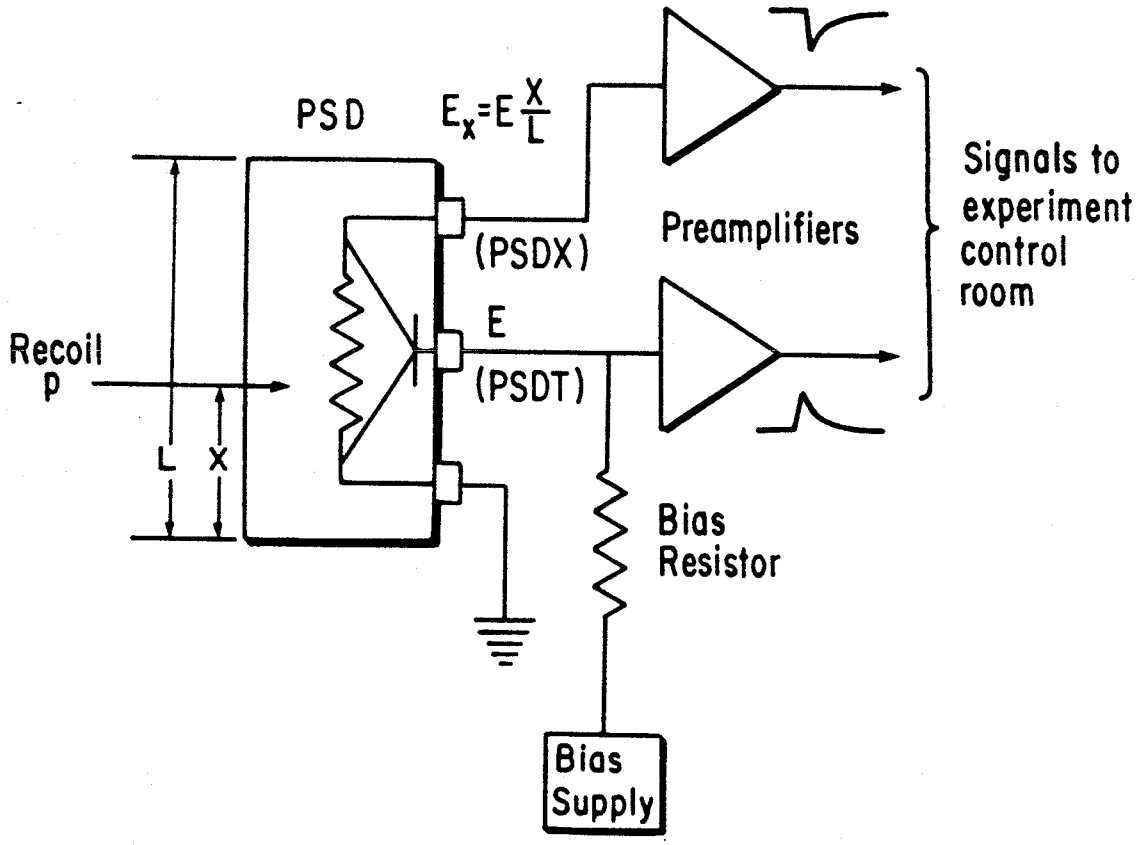

Figure 4.10 Position sensitive detector connections. The signal proportional to position (PSDX) emerges inverted with respect to the full energy signal (PSDT).

Our PSD was assembled by Jack Walton of Lawrence Berkeley Laboratory into an Ortec PSD case. A commercial PSD could not be used because a faster charge collection time was needed than was available. The resistive entrance window (7 mm x 47 mm) is an evaporated palladium film 100-150 Å thick covering a thin layer of SiO_2, giving an approximate silicon equivalent energy loss of 20 $\mu g/cm^2$ [4.11]. Bias is applied through a resistor in the total energy signal (PSDT) pre-amplifier (Figure 4.10). The current draw of this and all the other solid state detectors is measured periodically and as it rises due to radiation damage the bias is also raised to compensate for the voltage drop across the bias resistor. This assures that the full sensitive depth of the detectors remains depleted.

4.4.3 Range and Mass Formulae

The average range through silicon of an incident charged paricle of kinetic energy E (MeV) has been parametrized [4.12] with good accuracy over a large range of energies as

$$R(mm) = 0.004 + \zeta E^{\beta} \qquad (4.1)$$

with $\beta = 1.73$. The factor ζ depends on the mass of the incident particle (m_r) by

$$\zeta = 0.0133/(m_r/m)^{\beta-1} \qquad (4.2)$$

where the mass of the proton is m = 938.3 MeV. From Eq. 4.1 and the nominal detector thicknesses of Table 4.1, the maximum stopping power for recoil protons can be calculated. This is about 15.4 MeV for the DE detectors, 22.9 MeV for the thickness of the E detectors alone and 29.2 MeV for the full stack thickness of DE and E together. Based on initial calibration values, the amplification level of the signal amplifiers (Section 4.5) were set so that these maximum energy ranges would correspond to slightly less than the full 0 - 2048 channel scale of the ADCs.

For a particle penetrating the front detector and coming to rest in the back detector of a stack pair, two separate energy loss measurements are available from which the mass of the incident particle may be determined from Eqs. 4.1 and 4.2. The sum of the energies registered in the two detectors gives the total kinetic energy of the particle while the value from the front detector alone gives a measurement of dE/dx energy loss, hence the label of the front detector, DE. If E_{DE} is the energy recorded in the front detector and E_E the energy recorded in the back, then for a particle stopping in the rear detector the ratio of its mass to the proton mass is

$$\frac{m_r}{m} = \left\{ \frac{0.0133}{\text{Thik(DE)}} \cdot [(E_{DE} + E_E)^{\beta} - E_E^{\beta}] \right\}^{\frac{1}{\beta-1}} \qquad (4.3)$$

where Thik(DE) is the thickness of the front detector involved as listed in Table 4.1.

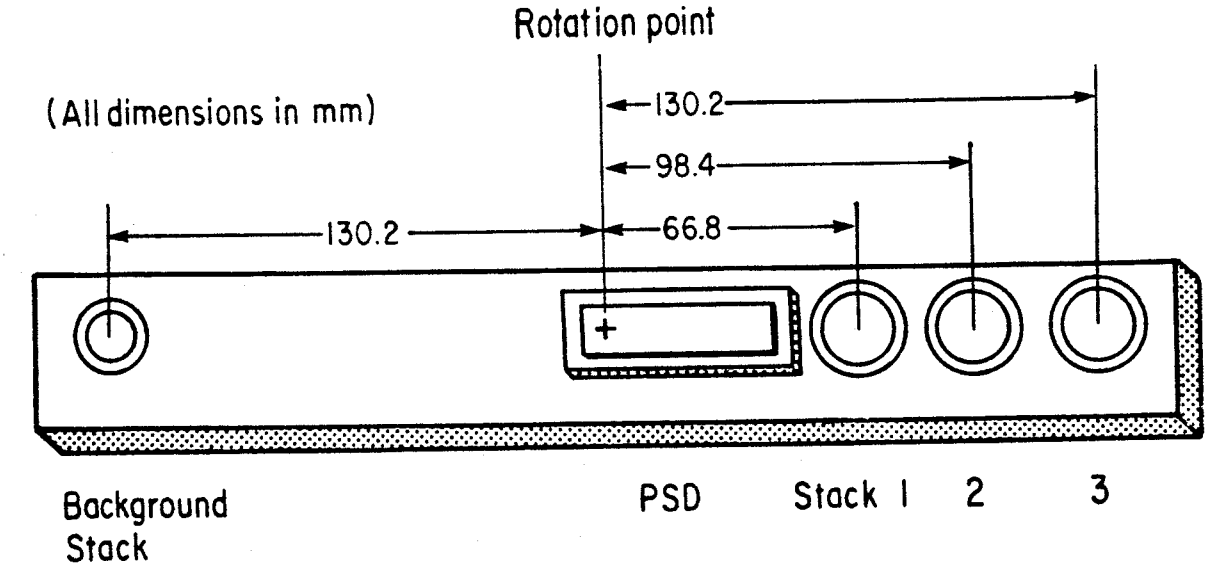

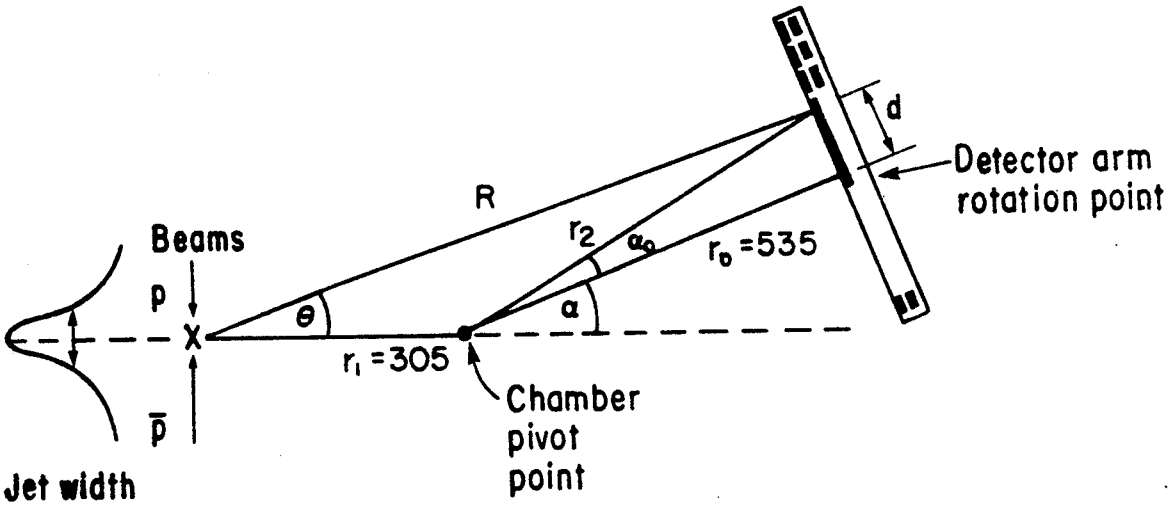

Figure 4.11 Layout of recoil detectors and angle relations.

4.4.4 Angle Relations

Figure 4.11 shows the distances separating the detectors and demonstrates the relation between the chamber pivot angle (α) and the recoil angle (θ) from 90^0. If r_0 is the imaginary axis from the chamber pivot point to the detector arm rotation point, then the angle from the axis to any distance d along the arm is $\alpha_0 = \tan^{-1}(d/r_0)$.

The recoil angle is therefore

$$\theta = \tan^{-1}\left\{ \frac{r_2 \sin(\alpha+\alpha_0)}{r_1+r_2\cos(\alpha+\alpha_0)} \right\}, \qquad (4.4)$$

where $r_2 = (r_0^2 + d^2)^{1/2}$; and the distance travelled by the recoil proton to the detector surface is

$$R = \frac{r_2 \sin(\alpha+\alpha_0)}{\sin\theta} . \qquad (4.5)$$

In the case of the PSD of length ℓ, the distance from the pivot point is obtained from the detector signals labelled PSDT and PSDX by

$$d = \left\{ \frac{PSDX}{PSDT} \cdot \ell \right\} - 7 \text{ mm} \qquad (4.6)$$

since the low-angle edge of the detector extends 7 mm beyond the pivot point.

4.5 Event Read-out and Trigger Electronics

The signals from the detectors pass to the outside of the vacuum chamber (Figure 4.12) via ceramic bulkhead connectors of mixed MHV and BNC type. The attaching cables are insulated with teflon tubing and were tested before installation for satisfactory out-gassing properties in high vacuum. While it was desirable to make the cables as short as possible so as to limit the detector capacitance, it was also necessary to have sufficient length to allow the detector array arm to rotate 180°, a feature which also required judicious cabling choreography. Pre-amplifiers, mounted directly onto the back of the chamber, convert the charge pulses originating in the detectors into proportional voltage pulses for passage to a patch panel then via long cables to the Experiment Control Room on the surface. Bias voltage for each detector is supplied from the Control Room where, additionally, a tail-pulse generator provides a test pulse. The pulse is fanned-out via a resistive divider on the patch panel to the test inputs of all the pre-amplifiers. With the intention to control ground loops, the grounds to the pulser and the bias voltage lines are interrupted at the patch panel with resistors giving each detector a one-point direct ground connection to the Control Room electronics through the signal cable.

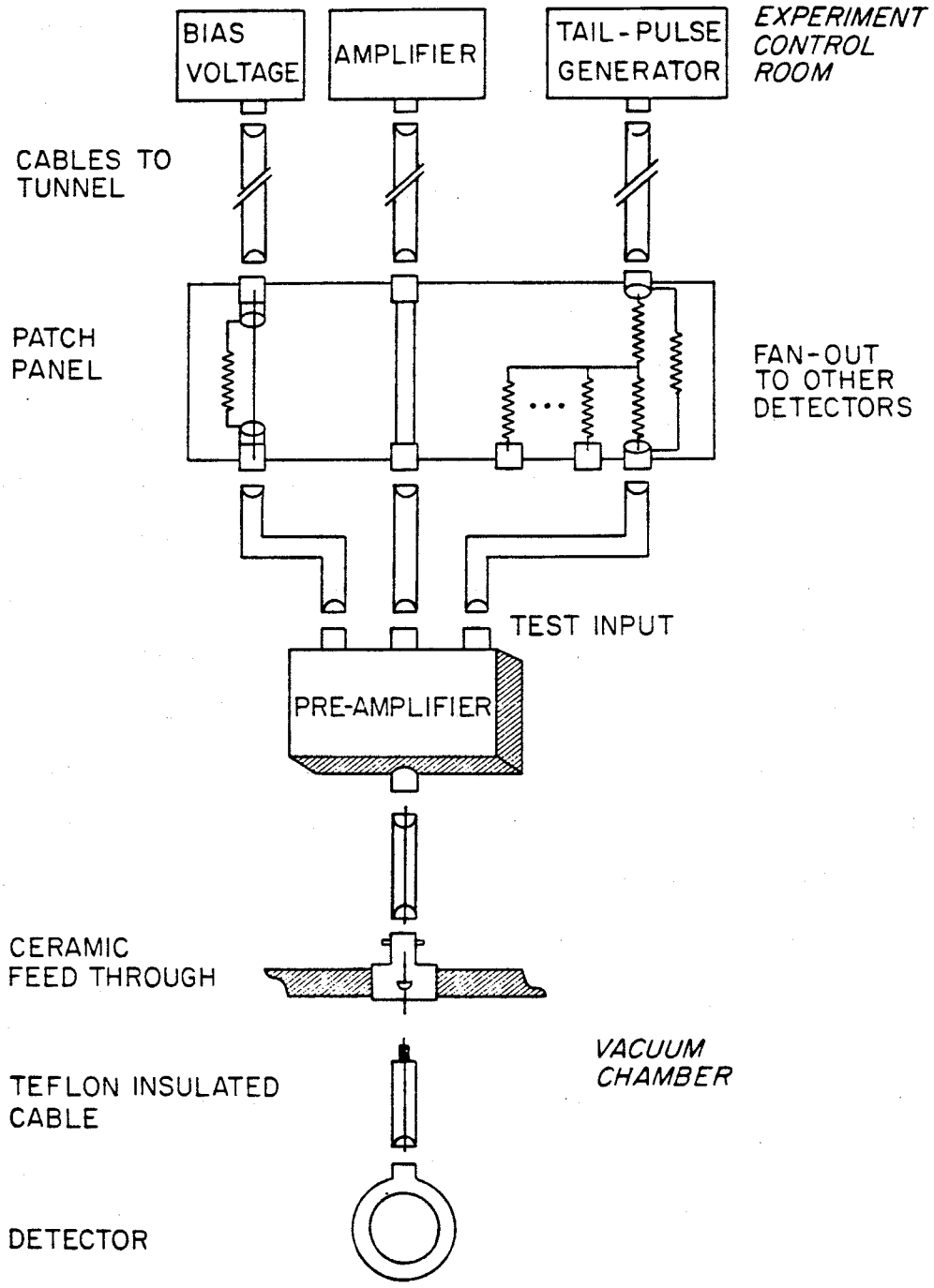

Figure 4.12 Connections between the detectors and the read-out electronics.

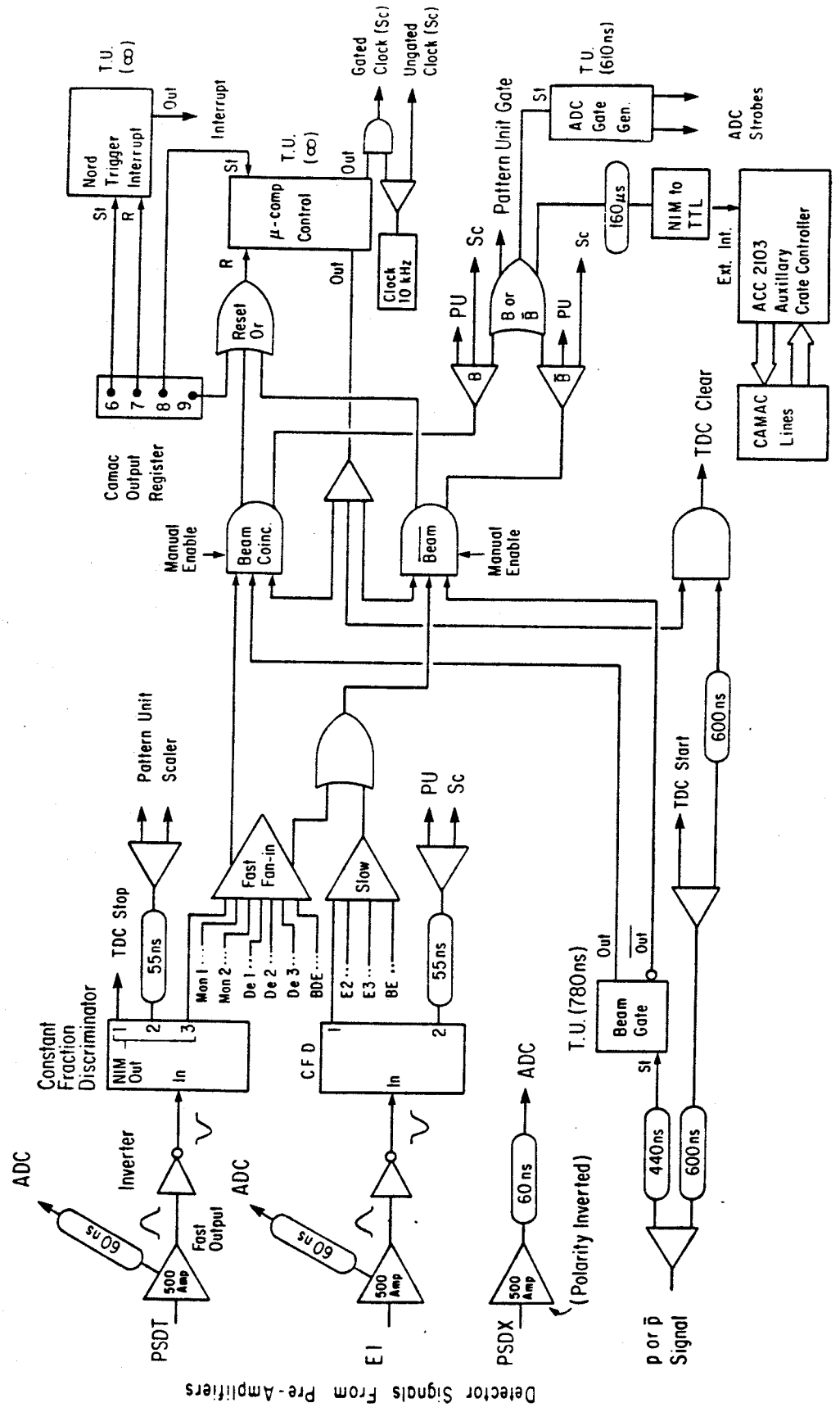

Figure 4.13 Event read-out and triggering system.

Figure 4.13 shows the detector read-out and trigger logic and is described in the rest of this section. The signal from each detector is amplified and shaped in a modified Mechtronics Model 500 amplifier. The first RC network in the amplifier shortens the normally long time constant decay of the pre-amplifier output to reduce pile-up effects and provides pole-zero cancellation to prevent baseline undershoot. The signal is then integrated and clipped a second time for an improved signal-to-noise ratio. One of the two originally identical amplifier output channels was modified with the addition of an Ultra Fast FET Operational Amplifier to send off the signal to the triggering electronics as quickly as possible. The unmodified output delivers the signal to a peak-sensing Analog-to-Digital Converter (ADC) channel. All the detector signals are of positive polarity, as required by the ADC, with the exception of PSDX (Figure 4.10) so the amplifier polarity for that channel is inverted. Also, since the PSD is triggered only from its PSDT output, the amplifier for the PSDX signal needs no Fast Output signal.

If there is a signal from a detector above the pre-set threshold level of the Constant Fraction Discriminator (CFD), the discriminator issues a NIM-level logic pulse indicating such presence. The CFD requires input of negative polarity so the detector signal must first be inverted. The constant fraction technique reduces the relative spread in time of the different sized pulses coming from the solid state detectors to permit more optimal timing measurements to be made. Each input signal is divided so that a portion is delayed and subtracted from a fraction of the undelayed

signal. The resulting bi-polar constant-fraction signal has a baseline crossover with reduced dependence on the input signal amplitude. Since the shaping delay required for this particular detector configuration is unusually long (400 ns), there is some slewing of the time measurements, especially toward lower signal amplitudes, but this is easily corrected during analysis as described in a later section.

Two different set-ups are used for triggering depending upon whether normal data collection or a calibration run is intended. In data-taking mode, only the front (DE) detectors of the stacks, the luminosity monitors and the PSDT signal are in the trigger. Depending on the type of data being collected the amplifier channels Mon 1 and Mon 2 are connected to luminosity monitors p1 and p2 for proton running or to $\bar{p}1$ and $\bar{p}2$ for antiproton running. The modified Fast Outputs are fanned together, as are separately the unmodified ("slow") outputs of the back (E) detectors of the stacks. (In Figure 4.13 only the amplifier inputs of PSDT and E1 are shown, the others being identical.) The "Beam" coincidence unit is manually enabled while the "$\overline{\text{Beam}}$" unit is disabled allowing only the "fast" signals to trigger when the Beam Gate indicates the simultaneous passage of a beam bunch. For a calibration run the coincidence enables are reversed so that any detector can trigger but only when there are no beam particles passing. Normally, calibrations are performed during collider down periods but this feature permits the option of calibration during machine running.

Electrostatic couplers upstream and downstream from the jet target sense the passage of the p and $\bar{p}$ bunches. The more intense p bunch is much more clearly discernable so it is used to provide a window 600 ns later in which to look for the $\bar{p}$ bunch. The experimenter chooses either the p or $\bar{p}$ signal depending upon the type of running desired. A TDC Start occurs with every beam bunch passing of the chosen type then any TDC channel is stopped if a Fast Output signal of the corresponding detector fires a discriminator. If no detector triggers following the beam bunch passing, the TDC is reset by the TDC Clear signal before the next bunch comes along.

A scaler channel associated with each detector is incremented each time it satisfies the discriminator conditions regardless of whether or not it goes on to trigger event recording. In addition, scaler channels keep track of the number of times the beam and beam coincidences are satisfied. Two scaler channels count the pulses from a 10 kHz quartz clock, one channel unrestricted and the other interrupted whenever the apparatus is busy reading an event. The ratio of these channels is proportional to the apparatus livetime. All scaler channels are two 16-bit computer words in length and are set to zero at the start of a run. The channel pattern of the scaler words is given in Table 4.2. A Pattern Unit module encodes the trigger pattern of each event into a word for which the bit pattern is shown in Table 4.3. (Note that the detectors associated with PU bits 9-12 are not in the trigger.)

Table 4.2 Scaler channels

Scaler Word	Channel
0	P1
1	$\overline{P1}$
2	P2
3	$\overline{P2}$
4	DE1
5	DE2
6	DE3
7	BDE
8	PSDT
9	E1
10	E2
11	E3
12	BE
13	Beam
14	$\overline{\text{Beam}}$
15	Ungated Clock
16	Gated Clock
17-23	(nc)

Table 4.3 Pattern Unit bits

PU Bit	Trigger
0	Mon 1
1	Mon 2
2	Mon 3
3	(nc)
4	DE1
5	DE2
6	DE3
7	BDE
8	PSDT
9	(E1)
10	(E2)
11	(E3)
12	(BE)
13	Beam
14	$\overline{\text{Beam}}$
15	(nc)

nc = no connection

4.6 The Data Aquisition System

The data aquisition system is based on a NORSK-500 computer possessing two central processing units (CPU): the 16-bit ND-100-CPU and the 32-bit ND-500-CPU. Data aquisition is shared with the other detector systems of Experiment UA6 which have separate trigger electronics in the manner schematised in Figure 4.14. All the input-output devices (floppy disk, 75 Mbyte hard disk, two 6250 Bpi tape drives, printer, terminals and the CAMAC System Crate) are connected to the input-output bus of the ND-100-CPU. Communication between the ND-100-CPU and the ND-500-CPU is accomplished through the three registers of the "Mail Box" and through the shared memory. The interface between the computer and the experiment is the CAMAC System Crate with data lines connecting it to the CAMAC Branch Crates containing the read-out electronics.

So as to contribute minimally to the total deadtime of the computer data aquisition, the recoil arm events are first written locally into a buffer controlled by a 16-bit microprocessor known as the Auxiliary Crate Controller (Model ACC 2103 by SEN Electronique). Whenever the trigger conditions are satisfied, the TTL pulse to the ACC External Interrupt initiates the ACC to write the Pattern Unit word, all TDC and all ADC channels into the ACC buffer. The buffer is full when 38 events have been written, the first of which is always a "Scaler Event," a dump of the current contents of the scaler modules. The ACC then signals the central trigger electronics that it is ready to be read out. The VIP signal, sent

to the CAMAC System Crate, interrupts the ND-100-CPU which proceeds to read the ACC as if it were an "event" and to write it to tape.

The data aquisition program DAS functions on the NORSK-500 under the operating system SINTRAN-III/VSE while the program ANL permits a preliminary analysis of a sampling of the data on-line.

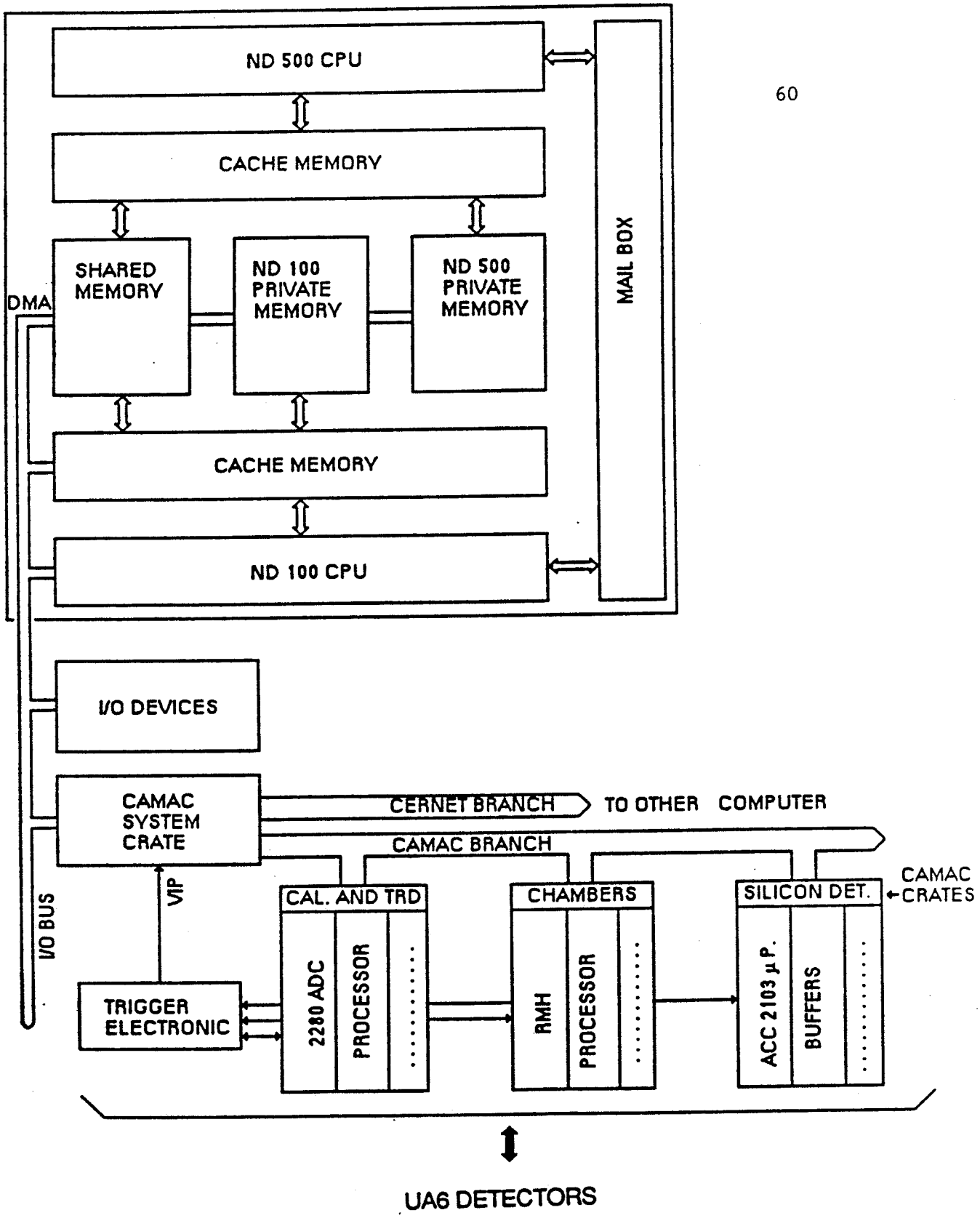

Figure 4.14 Simplified schematic of the hardware data aquisition system.

CHAPTER 5 Data Collection

5.1 General Strategy

A salient feature of the recoil arm apparatus is the ease in moving the detectors to different angles and in switching their orientations between intercepting recoils from pp and $\bar{p}p$ collisions. This allows scattering rates at a selection of momentum transfer values to be measured with the same detectors and enables $\bar{p}$ and p running to be intermixed, thereby controlling to some extent systematic uncertainties.

As described in Section 4.4.1., alpha sources for calibration are mounted permanently beneath the rear E detectors of the stacks. The sources for E1 and E2 are fixed directly on the moving arm, but for E3 and BE, equidistant from the center at the ends of the arm, the sources are mounted onto the stationary bulkhead plate as in Figure 5.1. In this way the arm can be rotated between the proton and antiproton positions, returning to the same horizontal orientation by monitoring the rate of the alpha particle hits in the E3 and BE detectors and stopping where the rates are maximal.

The ability to rotate the detector array also was essential in finding the approximate "center" position of the vacuum chamber corresponding to $\theta = 0°$ (as in Figure 4.11), that is, where the point of rotation of the detector array arm is perpendicular to the beams at the jet/beam intersection point. This is required for knowing to what value of θ a

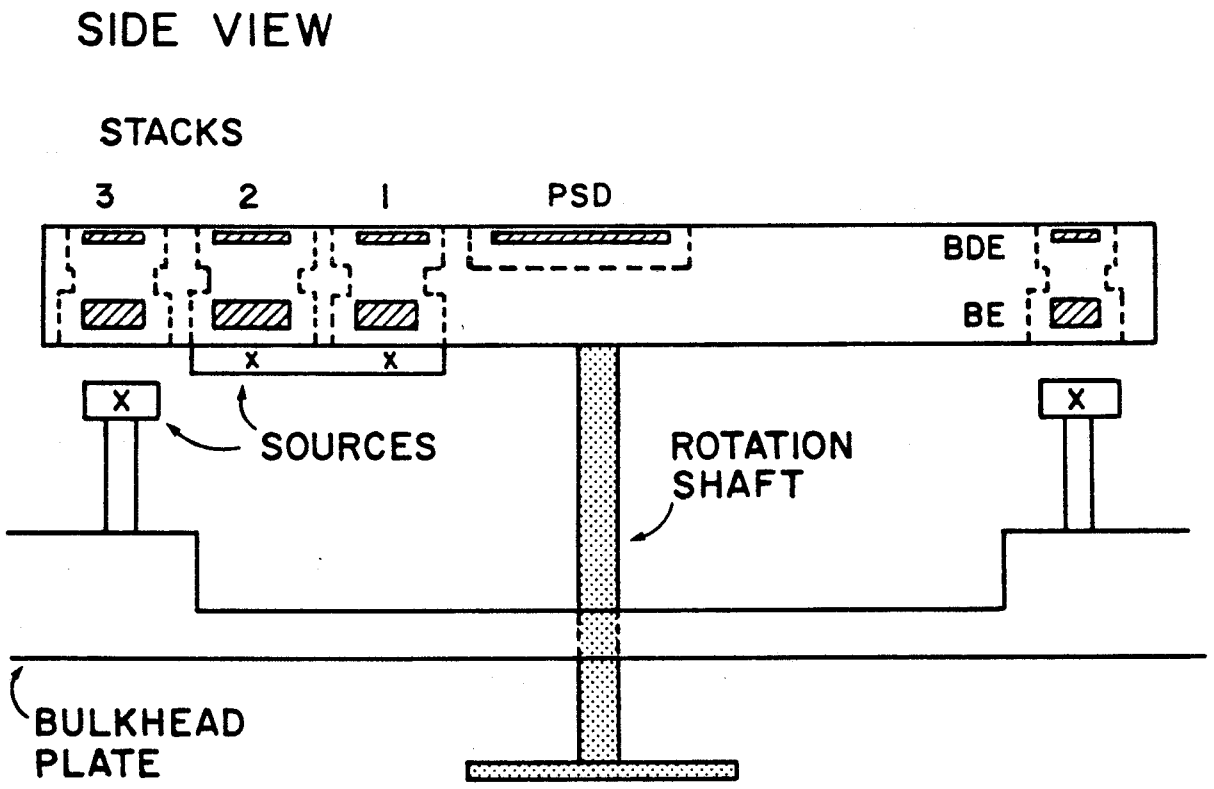

Figure 5.1 Rotatable detector array arm showing location of fixed alpha sources for calibration of the back detectors.

particular value of the chamber pivot angle (α) corresponds. The center position is determined while running with beams and jet by rotating the detector arm back and forth between the p and $\bar{p}$ sides (and of course changing the trigger) while adjusting the chamber pivot angle until the elastic scattering peak is at the same energy on both sides. This procedure is repeated at the beginning of a Collider running period or anytime the jet housing is moved or rotated.

5.2 History of Running

5.2.1 Installation and Early Running Periods

The rotating arm and detector assembly and the fixed luminosity vacuum chamber were constructed at Rockefeller during 1982 while the large, moveable vacuum chamber was built at CERN. Following tests in a specially constructed test chamber, installation in the SPS tunnel began in February 1983 followed by a first look at jet/beam collisions with the luminosity monitors in May. The recoil arm detectors were first installed in June. Cabling and assembly of the read-out electronics continued into 1984 as the rest of the UA6 magnetic spectrometer was constructed.

The major data taking period was originally planned to be during the November-December 1984 Collider Period, but significant problems led to the abandonment of this data for the recoil arm in the approximately 500 runs on 200 magnetic tapes when it became clear that the data collected during 1985

were greatly superior in quality. For one thing, the running period was too short (less than six weeks) to resolve all the serious apparatus difficulties and still collect sufficient data for a worthwhile measurement.

But the 1984 run was sullied mainly by the restriction placed upon UA6 during this period by the CERN management responding to objections from Experiment UA1 limiting the intensity of the jet to 10% of its maximum potential. This meant that only a fraction of the anticipated luminosity could be accumulated and with a poorer signal-to-noise ratio. In addition, E1 was unusable for almost the entire running period, and DE2 and BDE repeatedly gave problems. There were also serious problems with the fixed luminosity monitors. As it turned out, the jet housing was twisted by about 12 mrad so that the scattering angle to the p monitors was not the same as the angle to the $\bar{p}$ monitors. In fact, the angle to the proton monitors was so small that the peak was practically buried within the detector electronic noise while the antiproton monitor angle was so large that a majority of the recoil protons penetrated through the detector. Several inoperable TDC channels also meant that no time information was able to be recorded for the luminosity monitors. With these problems, it was impossible to extract sufficiently accurate figures for the luminosity, especially in the case of proton running.

Following the 1984 Collider Period these hardware problems were addressed. The detector array arm and mounting plate, which are always removed from the tunnel during SPS fixed target operation to avoid radiation

damage to the silicon, were brought to the Experiment Control Room for tests and modifications. At this time it was discovered that a film of an unknown substance was deposited on the front surface of the PSD, so it, and additionally BDE, were replaced with spare detectors. The problem with E1 was traced to a cabling error during installation in the tunnel and corrected (a BNC cable had been used to connect the E1 bulkhead feedthrough connector, of the MHV variety, to the pre-amplifier). DE2 simply needed the center tines of its feedthrough connector tightened for better contact. It was also determined that the inoperable TDC channels were missing because they were not being written into the buffer by the ACC. This was rectified by adding the 160 μs delay shown in Figure 4.13 to the signal to the ACC External Interrupt. Also, the jet housing was turned back so that the luminosity monitors were better centered perpendicularly to the beams. Additional shielding was added to cover the signal patch panels for the recoil arm detectors and the monitors so as to reduce electronic pick-up in the tunnel.

The silicon array was re-installed in February for a special run during March in which the Collider was run at 100 GeV and cyclically ramped up to 450 GeV for a few seconds in the endless quest for higher energies. The beam intensities turned out to be so small that few usable data were collected, but the detector performance was found generally to be greatly improved.

5.2.2 1985 Running Period

All results reported in this document were obtained from data collected during the Collider Period from September through December 1985. For this period an agreement had been worked out with CERN management and UA1 to permit the UA6 jet to operate at full intensity.

Two significant breakdowns interrupted data collection during this period but generally the modifications and repairs performed during the shutdown were successful. Two weeks into running one of the molecular turbopumps on the jet seized, again turning the jet housing and requiring nine days to repair. A new center position for the chamber pivot point angle then had to be determined, and since the runs taken up until then were mostly concerned with testing the apparatus, they were ignored in the PSD analysis. A bad PSDX pre-amplifier also invalidated seven days of PSD data until it was replaced. A third amplifier/discriminator channel was added to allow one $\bar{p}$ luminosity monitor to take data while the rest of the semiconductor detectors operate on the proton trigger, thus continuing the luminosity measurement for the rest of UA6.

Data collection proceeded typically as follows. After the value of the chamber position readout corresponding to the center ($\alpha = 0°$) was determined, the chamber could be pivoted by a certain amount in one direction so that each detector could accept recoils from, say, pp scattering at a particular scattering angle (θ). Then the detector array

could be rotated 180° and the chamber pivoted by the same amount in the opposite direction from $\alpha = 0°$ where the detectors could accept $\bar{p}p$ data at approximately the same scattering angle. The relationship between α and θ is given by Eq. 4.4, where the distance d to the stack centers is shown in Figure 4.11. Generally the arm was left at a particular angle in the set-up for $\bar{p}p$ scattering for one or two days of running then moved to a new angle, with a source calibration run in between when there was no beam. Twice during the Collider Period the arm was moved over to the pp position where it was attempted to accumulate about the same amount of data, but with shifts between angles much more frequent due to the increased proton beam intensity. Some running was also done at higher values of α for the single diffractive measurement using the stack detectors but the results of that analysis will not be reported here.

General features of the Run Sets used for the PSD analysis are summarized in Table 5.1. Run Sets are defined as groups of runs of the experiment (usually one run per magnetic tape) taken successively at the same angle and analyzed, as explained in a later section, with the same cut parameters. For the most part, a Run Set was continuous over a particular fill of the Collider so that the background conditions would remain similar, but some Run Sets overlap two or three fills, especially if they were short. A short-hand is used for labelling the Run Sets using a "P" for proton and "Pb" for antiproton running. The middle figure indicates the nominal α angle ("h" is 1/2°) and the final number gives the sequential order of the Run Set during the Collider Period. In this way each Run Set can be

Table 5.1 General features of Run sets included in the PSD analyses for pp and $\bar{p}p$.

Run Set	Nominal α	Integrated Luminosity	Jet Intensity	Number of Runs	Beam Intensity ($\times 10^{10}$ particles) At Start	At End
P01	0°	53 nb^{-1}	100%	7	42.5	39.0
Ph1	1/2°	80	95%	8	43.9	39.5
P11	1°	52	100%	7	39.0	33.6
P22	2°	135	98%	11	42.0	35.5
Pb04	0°	55	100%	36	6.13	4.71
Pb05	"	70	100%	47	6.21	4.66
Pbh1	1/2°	33	95%	7	2.28	2.1
				9	3.9	3.5
				3	4.57	4.44
Pbh2	"	30	97%	11	3.43	2.77
				20	4.55	3.36
Pbh3	"	49	100%	32	6.15	5.01
Pb11	1°	39	97%	34	4.64	2.73
Pb12	"	49	100%	44	5.19	3.92
Pb21	2°	74	96%	9	4.32	3.70
				16	5.19	4.51
				14	5.19	4.4
Pb22	"	33	100%	11	3.42	3.07
				13	4.45	4.12
Pb23	"	44	100%	28	5.23	4.36
Pb24	"	49	100%	22	5.86	4.81

uniquely identified. For example, Pb04 refers to the fourth time that the anti-proton trigger was run with the chamber pivot at 0°. Obviously, due to various considerations, not all Run Sets were included in the analysis.

The other entries in Table 5.1 give a rough comparison among the Run Sets. The Integrated Luminosity is the figure given by the luminosity monitors (before inter-normalization using the PSD) as explained in Chapter 7. The number of runs comprising a Run Set is shown, but each run is not necessarily of the same length, and the jet intensity is given as the percent of approximate maximum intensity. The beam intensity, or the number of particles in the three bunches of either the p or $\bar{p}$ beam, reduces over time as particles are lost. The approximate values at the beginning and end of the Run Sets are given as measured by the SPS Control Room.

Other running under special conditions was carried out to make various checks and comparisons. Pulser runs without beams to test ADC linearity and TDC slewing were written to tape. The detector array was also rotated 90° to a vertical position and operated with the proton trigger so that all the stacks could intercept recoils from the same angle simultaneously. With the arm in that position the vacuum chamber was moved to an angle such that the elastic recoils would stop in the front (DE) detectors, then moved to a larger angle so that they would stop in the back detectors. In this way the relative acceptance of the DE and E detectors in Stacks 1, 2 and 3 could be determined. Some running was also performed with the jet steered out of the

beam to help assess background, but so little running was done as to be inconclusive.

5.2.3 Data Compaction

Approximately 1100 "raw" tapes were written by Experiment UA6 during the 1985 Collider Period interspersing the scattering experiment data with magnetic spectrometer events on the tapes. Using the CERN mainframe computers, the scattering data written in the compacted Auxiliary Crate Controller (ACC) structure (see Section 4.6) were extracted from the raw tapes and written onto 95 Condensed Data Tapes (CDT) of density 1600 Bpi. During this procedure the ACC event structure was disassembled and the 38 original events in an ACC dump were written as separate entries in EPIO format. Most of the CDT writing was done with a modified version of the standard UA6 analysis program but some CDTs were written more easily using the CANOPUS system of P. T. Cox. These condensed tapes were shipped to Rockefeller for analysis and copies were stored in the tape vaults at CERN.

5.3 Possible Sources of Systematic Error

While collecting data for the experiment some characteristics of the detector signals were noted that were thought might contribute to the uncertainty of the final measurement. From the initial installation of the experiment, a noise pick-up was evident on all the detector output signals when monitored with an oscilloscope. The source of the noise was traced to

a particular set of the vacuum pumps for the jet and also to some of the magnets of the SPS. The noise was especially evident on the PSDX signal where it was 3-4 times more intense than on its partner PSDT. Much effort went into shielding both the pre-amplifier connections and the pumps themselves, and into testing various grounding configurations for the detector signals. Some reduction was obtained, but in the end the noise contributed little to the uncertainty of the rate and to the energy measurement, especially in the case of the stacks where the noise level was insignificant compared to the size of a pulse from a particle detection. The additional spread in the position measurement of the PSD was also not important compared to the spread at a particular energy due to the jet width.

Pick-up from the beam itself was sometimes more serious. A pulse in time with the 7.68 μs frequency of the proton bunch passing was always evident on all the detectors when the Collider was running, but its amplitude varied widely. Usually it was very small, but sometimes at the start of a machine fill the pick-up on one or more of the detectors would be so great as to exceed the discriminator threshold and cause the channel to fire wildly. The particular detectors affected by this would vary and the amplitude of the pick-up associated with each of the three proton bunches would typically be different. As a machine fill stabilized, sometimes after as much as an hour or two, the amplitude would reduce drastically. The pick-up was thought by a consultant from the SPS Control Room to be related to the electrostatic induction on the vacuum pipe walls due to the "tails"

on the sides of the beams, since even a minor "external scrape" of the beams could cause a dramatic reduction. When this pick-up was large, the affected data was ignored in analysis.

Most of the systematic error on the final fit parameters originates from analysis considerations, which are discussed in the document sections which follow. These include the absolute t-scale, set by the calibration, and the rates associated with each value of t, which are dependent upon the data cuts, corrections for geometrical and nuclear collision losses and the subtraction of background and inelastic contributions. Finally the results are uncertain by the errors on the parameters from other external measurements (such as the total cross section) provided as input for the fit.

CHAPTER 6 Energy Calibration and Data Corrections

Before beginning the task of analysing the scattering data, an energy calibration file was created by analysing the calibration runs. Moreover, the consistency of certain electronic signals had to be checked and, if necessary, compensated for in the analysis program. The Pulser runs enabled the ADC linearity to be verified and TDC slewing to be corrected. In addition, special corrections to the PSD position and time signals had to be applied. These corrections were included in the main analysis program and are described in this section.

6.1 Source Calibration File

Four stationary and one rotatable ^{241}Am alpha sources mounted as previously described (Section 4.4.1) determine the detector energy scales. For a calibration run, the rotatable source was turned with the remote control motor so that it faced all the front detectors. It was then verified that alpha particles were hitting the detectors on the extreme ends of the arm, DE3 and BDE, and the trigger was switched to the configuration for calibration (Section 4.5). Hits were collected and written to tape until all detectors had sufficient peaks, usually within a few minutes. The rotatable source was then turned away from the recoil arm side and toward the luminosity monitors in preparation for running with beams.

As one of the first exercises at the start of analysis, the ADC value of the center of the alpha peak for each detector for every calibration run was assigned to the source energy (5.486 MeV). From this, the energy corresponding to the ADC value recorded for each recoil proton could be determined assuming linearity of the ADC scale. ^{241}Am has an extremely narrow line width but the peaks were not symmetric, possessing a low-leading tail probably due to detector edge effects. The peak centers were found from histograms of the ADC values of all the detectors by a program which fit a Gaussian to a narrow range around the very top of the peak. In Figure 6.1 is shown a typical example of the alpha peaks of a calibration run and the final fits determining the centers. The center values for each run were written into a calibration file along with the sigma of the final fit and its χ^2 value and with an assigned range of run numbers over which the calibration was assumed valid. This file was referenced by the main analysis program for each run.

Generally the calibration of a detector remained fairly constant. For instance, throughout the entire 1985 data collection period the PSD calibration never varied by more than 0.25% between adjacent calibrations and varied less than 0.7% overall. However, a couple of the stack detectors infrequently exhibited very large shifts between calibrations for reasons not understood. Fortunately these large shifts were not gradual but happened entirely within one run so that the run number range could be recorded in the calibration file and particular runs ignored. The DE detectors, however, did have a tendency to drift sometimes up to 2-3%

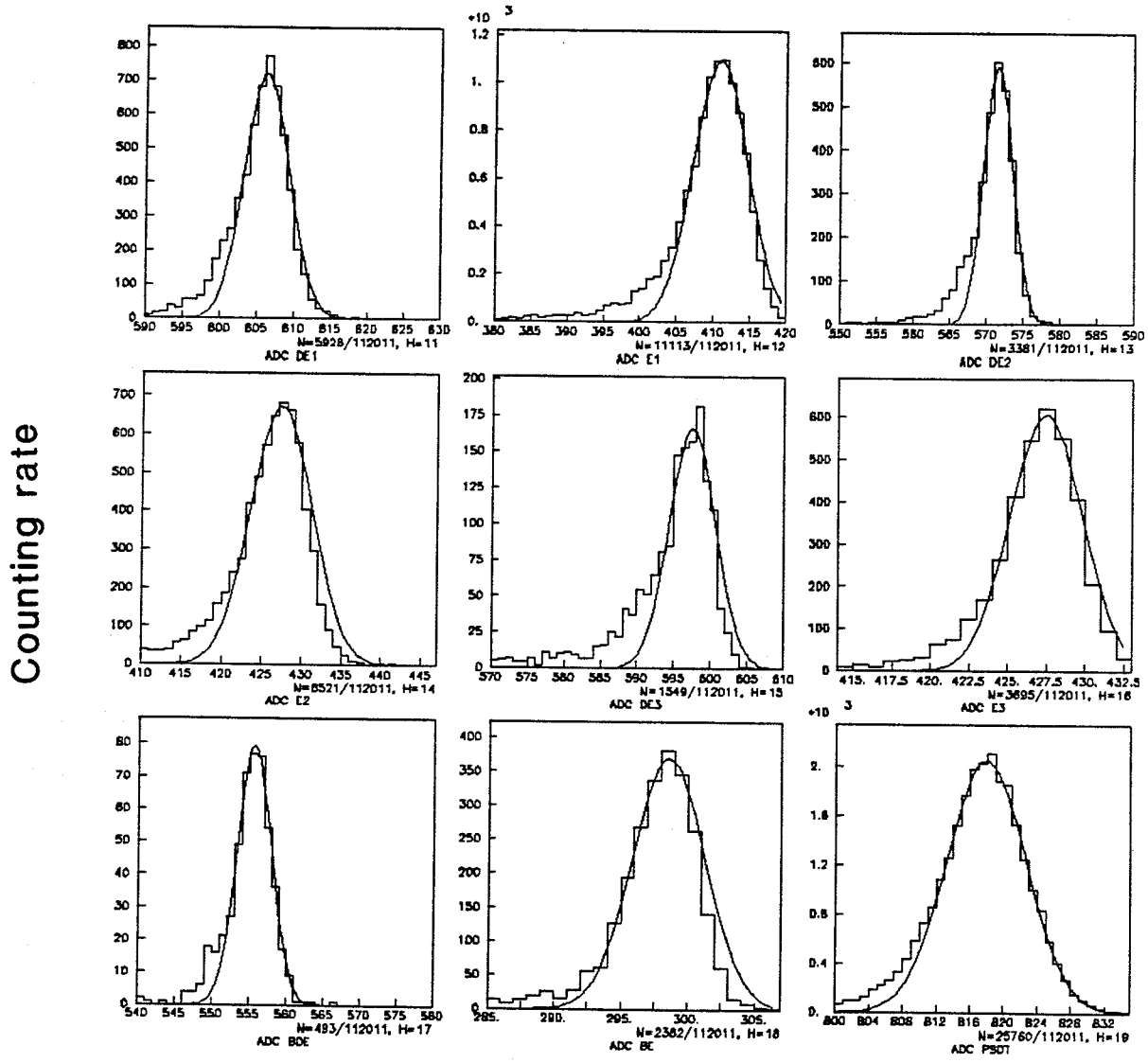

Figure 6.1 Alpha source calibration peaks with Gaussian fits to the center channels.

between calibrations. Because the E detectors were very stable it was possible to correct a Run Set for this drift using the recoil mass formula (Eq. 4.3) as explained in the following chapter.

To obtain the true particle energy from the detector response, one must account for not only the calibration factor, C, but for ΔE, the energy lost in the detector intrance window and for the energy lost into atomic processes, Γ, as in the relation

$$E = \Delta E + C \cdot N + \Gamma \qquad (6.1)$$

where N is the ADC channel measurement for the event. The energy lost in the window is a combination of energy lost in the metal surface electrode and the energy lost in the so-called "dead-layer," that is, any inactive volume of silicon through which the incident particle passes. Γ is the average energy expended by the particle in non-ionization collisions. These additional losses are insignificant for incident protons with $E > 1$ MeV so had to be accounted for only in the PSD analysis.

In Section 4.4.2, the approximate equivalent silicon energy loss of the PSD entrance window was given as 20 $\mu g/cm^2$. Assuming this amount of loss, the silicon range formula of Eq. 4.1 was used to derive a relation for its correction. Calculated values for the average energy expended in non-ionization processes for protons of $E < 1$ MeV were listed in Ref. 6.1. We parametrized these as

$$\Gamma(\text{MeV}) = 0.0014 + 0.00054 \ln(E') \qquad (6.2)$$

where E' is the particle energy in MeV before the correction. Even for the lowest energy particles discernable in the PSD at E = 0.5 MeV, these corrections totalled less than 1.5%.

6.2 Pulser Checks and TDC Slewing Corrections

The special Pulser runs were taken before the main data collection began by setting the Tail-Pulse Generator (see Figure 4.12) at several voltage levels from 0.3 to 7.0 V. The Pulse Generator was able to mimic the shape of the detector charge pulse entering the pre-amplifiers and to provide a uniform NIM-level trigger pulse for the TDC Start. At each voltage level enough events were accumulated to provide clear peaks in the ADC and TDC channels of all the detectors under full bias.

An immediate plotting of the centers of the ADC peaks (found by a Gaussian fit) versus Pulser voltages turned up a couple irregularities in the pre-amplifiers or their connections which were corrected. After this, line fits to the Pulser points gave correlation coefficients very close to +1.0 for all channels, verifying ADC linearity. The widths of the Pulser peaks, indicated by the sigmas of the Gaussian fits, also varied little as the Pulser voltage was changed. Under bias voltage the Pulser widths of the detectors in the stacks were typically ~0.1% of the full ADC scale and for PSDT was ~0.2%. This is the baseline energy resolution from detector noise.

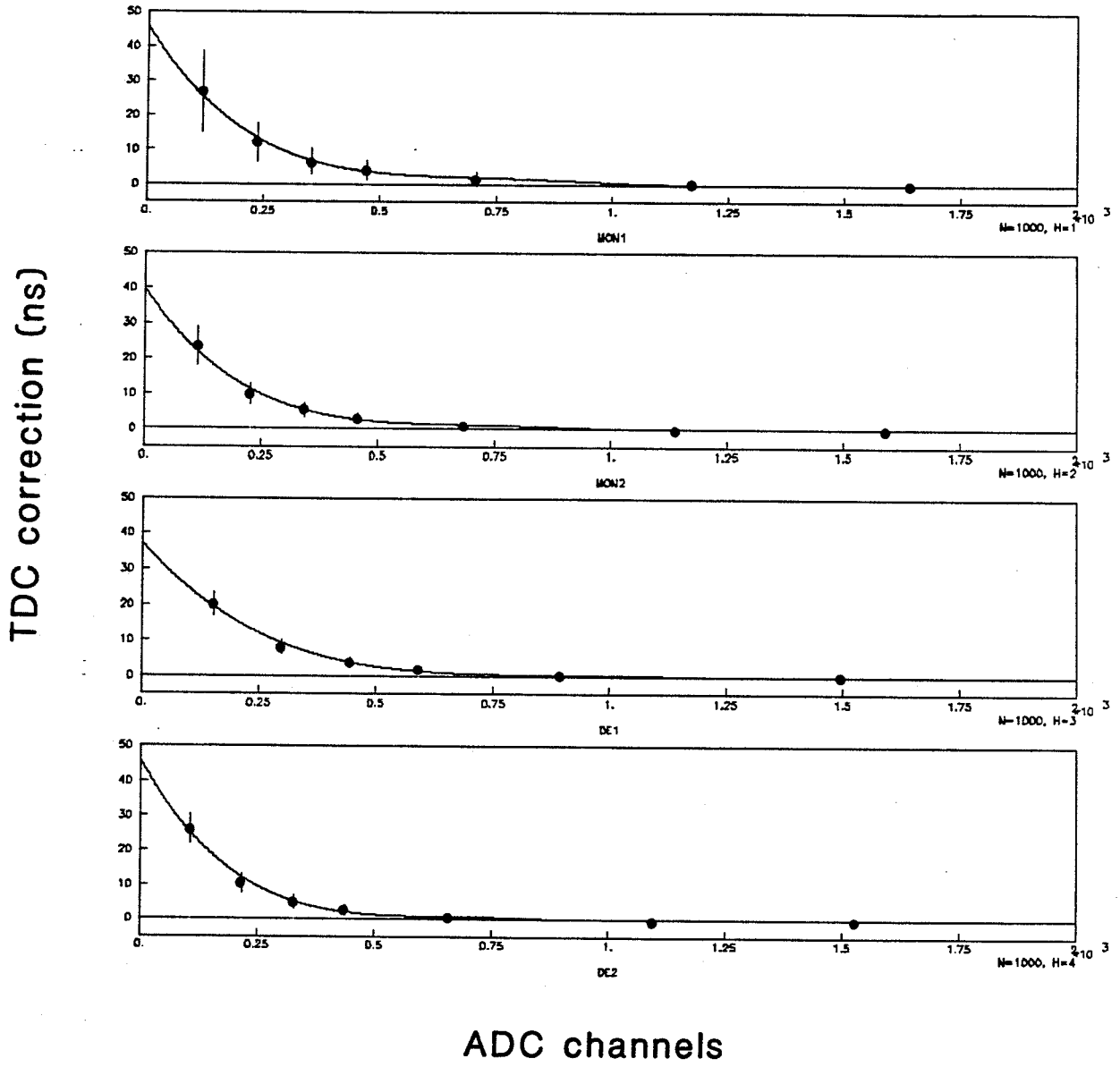

Figure 6.2 TDC slewing corrections from pulser runs. The time scale gives the difference measured by the TDC of equally delayed pulser signals at different voltage levels. The error bars represent the width of the measured time distribution. The curves represent fits made to these measurements used for the slewing correction.

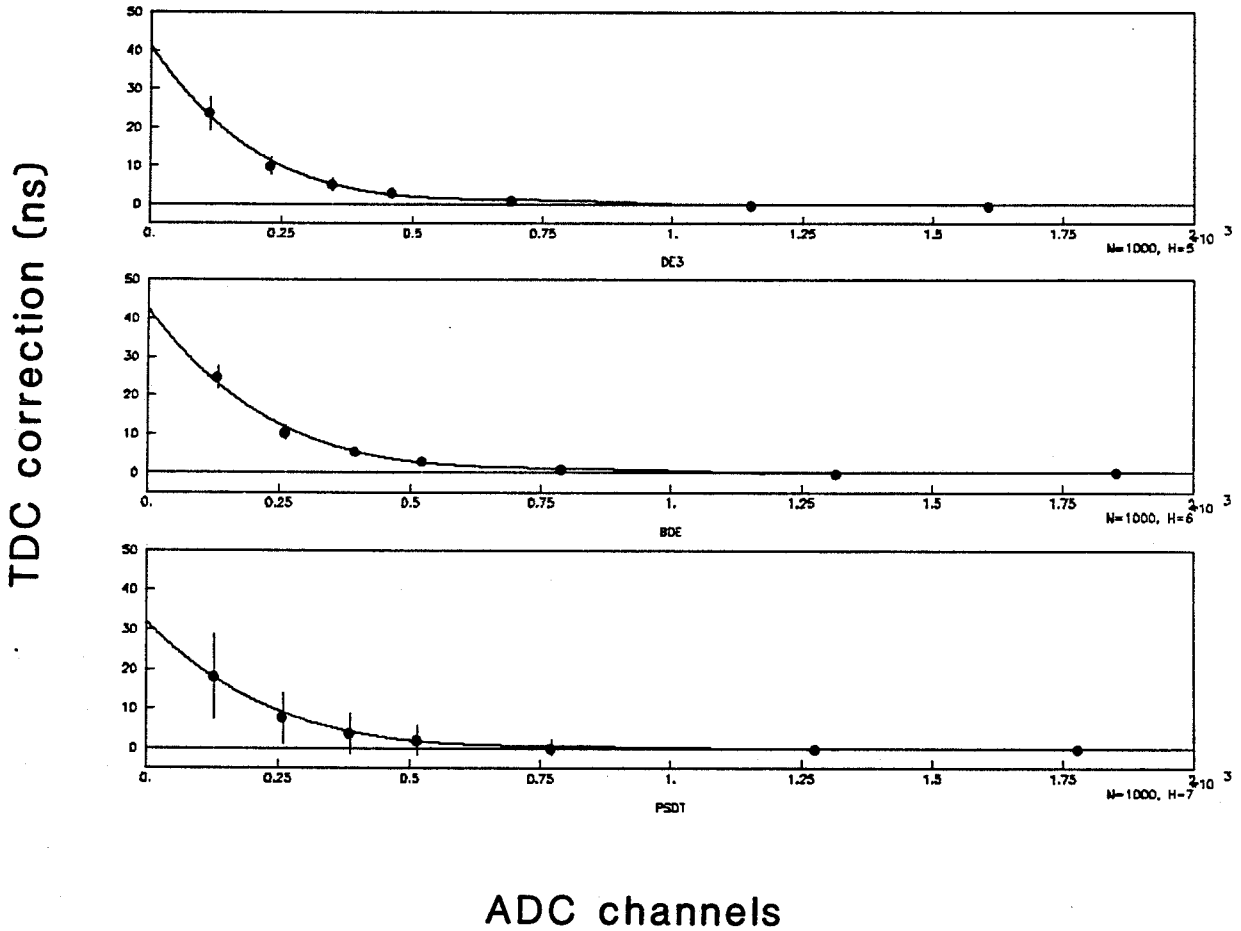

Figure 6.2 (continued)

The TDC channels, however, were strongly non-linear and had poorer resolution at lower Pulser voltages as seen in Figure 6.2. The figure also shows the polynomial fits used to correct for this slewing. These fits were incorporated into the analysis program and gave the amount to be subtracted from the TDC value associated with the raw ADC number of an event. Because the poorer TDC resolution influenced only the pulses of lowest voltage, it was important only for the PSD analysis, which therefore required TDC cuts strongly dependent upon energy for the data at lowest |t|.

6.3 PSD Position Non-linearity

Figure 6.3 shows the position distribution of events in the elastic peak from pp running after the detector array arm had been rotated 90° to a vertical direction (some of the special running discussed in Section 5.2.2). The chamber pivot angle α had been chosen so that the recoils would deposit all their kinetic energy into the PSD. Presumably, since the entire length of the PSD was oriented at the same angle θ from 90°, the whole active area should have been subjected to a uniform exposure of elastic recoils at the same energy. But as the figure shows, the uncorrected position signal looks anything but uniform. The rate is greatest in the middle and tapers off toward both ends whereas, instead, it should be constant all across.

One explanation for this would be if the active area of the PSD were physically smaller toward the ends. Indeed, the PSD holder does not

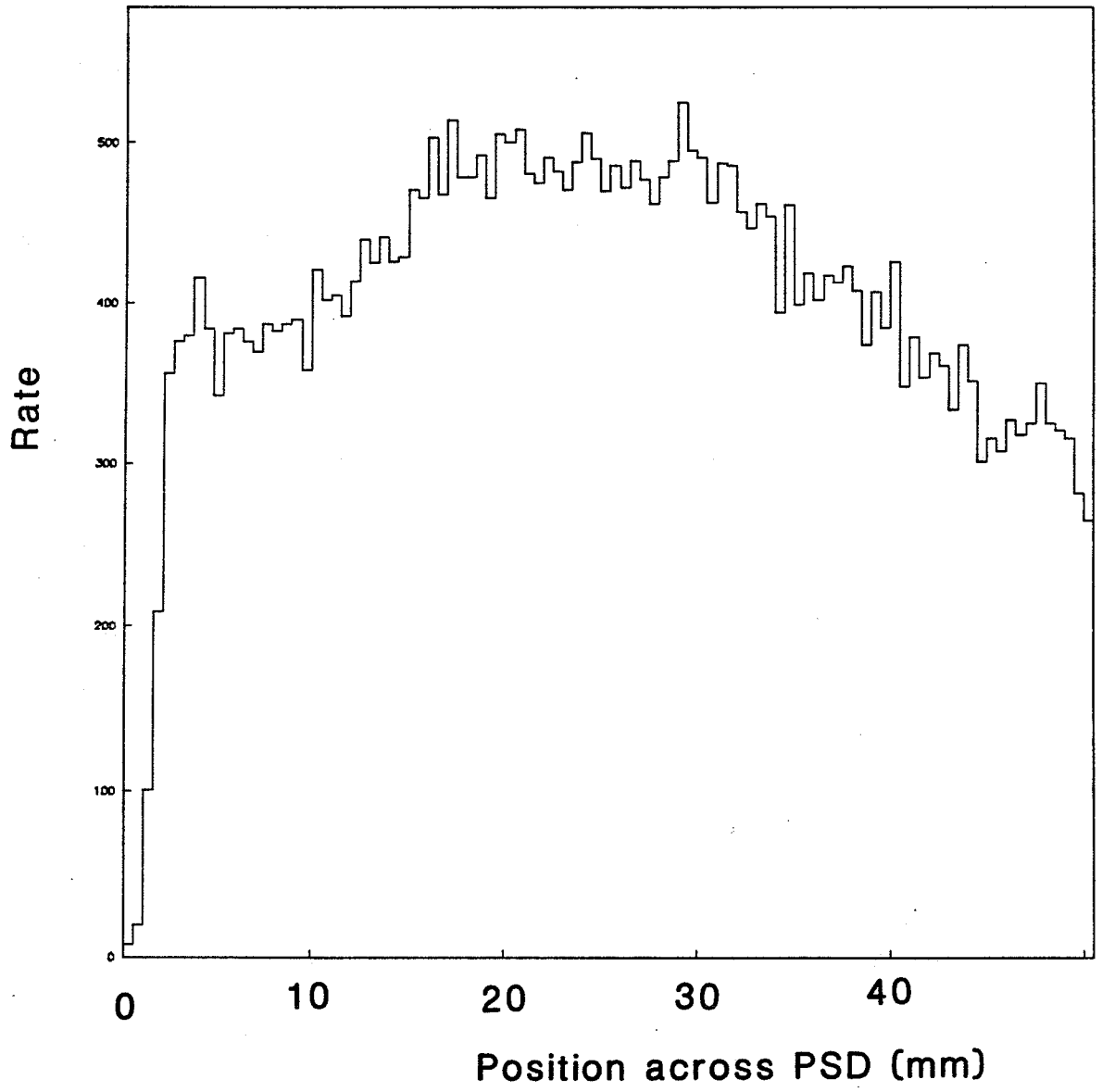

Figure 6.3 Uncorrected position distribution of elastic events from running while the detector arm was in a vertical orientation.

completely cover the silicon surface so the active area is somewhat irregular where it is attached along the edge. Using a microscope attachment on a milling machine with a precision electronic read-out, what looked to be the active area width was measured at 1 mm intervals along the length. The active area indeed was a few percent wider in the middle, but only by about 1/5 as much as would be necessary to explain the non-uniformity of Figure 6.3.

Another possibility is that the varying rate is attributable to a non-linearity in the position signal, so that equal divisions of the ratio which gives the position measurement really correspond to unequal areas of the physical active area. This could be caused by a non-uniformity in the resistive window which the PSD maker claims is to be expected to some extent since the layer was applied as an evaporated film. Figure 6.4 reports the results of an alpha source scan of the PSD which gave evidence for this assessment and shows how the non-linearity was corrected.

In order to perform the scan, the solid state detector array arm was removed from the tunnel and installed onto the test vacuum chamber which was set up in the Experimental Control Room. A special device was designed to be mounted to the side of the PSD so that a ^{241}Am source, similar to the one used for calibration, could be moved along a few centimeters above the detector. The source was mounted in a holder and collimated to a width of about 0.5 mm. Runs were taken with the electronics in the usual configuration for calibration at several positions along the PSD at

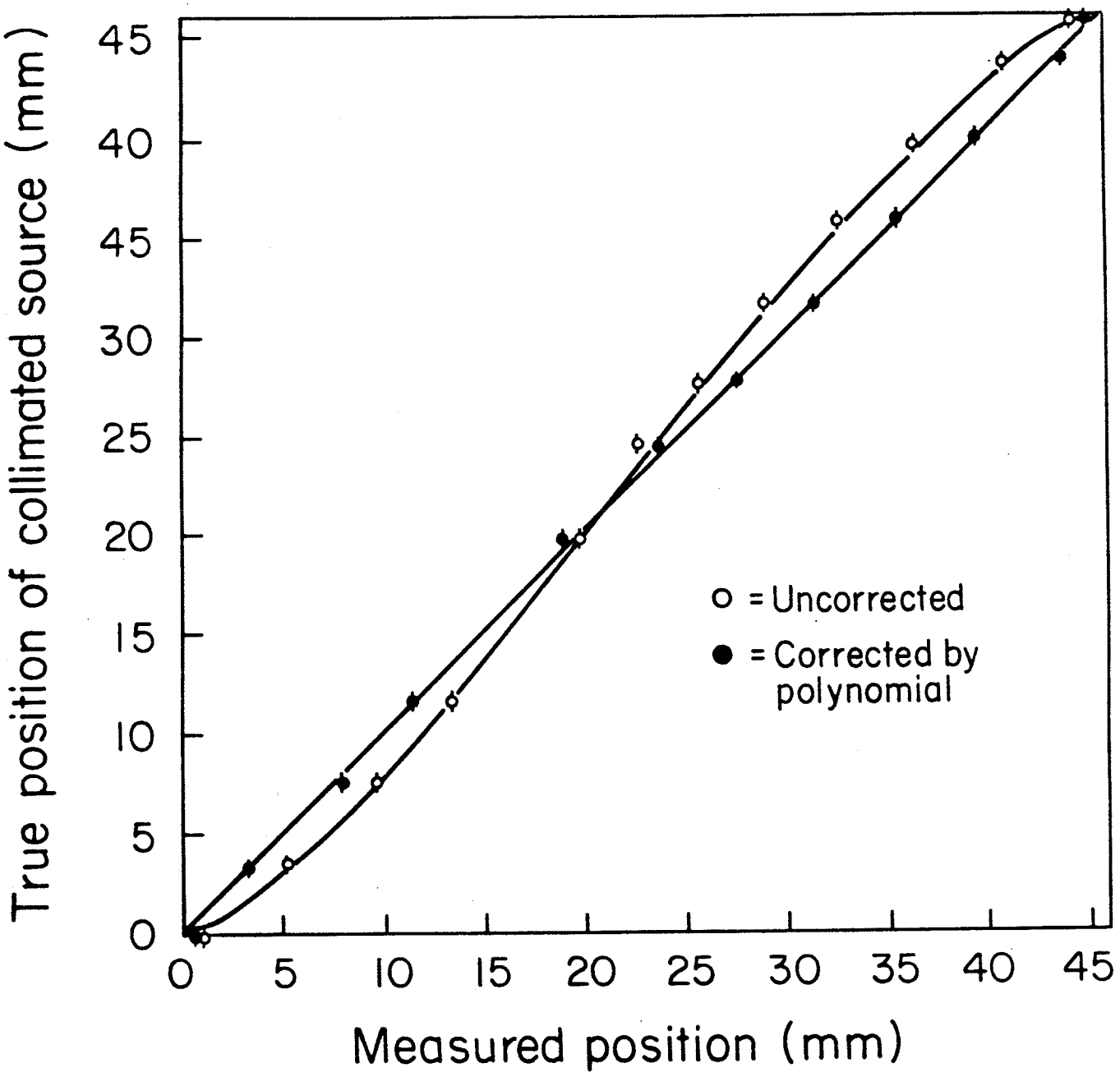

Figure 6.4 Results of a scan of the PSD with a collimated alpha source. Open circles show the non-linearity of the correspondence between the measured and the actual positions of the source. The curved line is the polynomial fit to the uncollimated data of Figure 6.5 which was used to correct the measured collimated postions as shown by the dark circles.

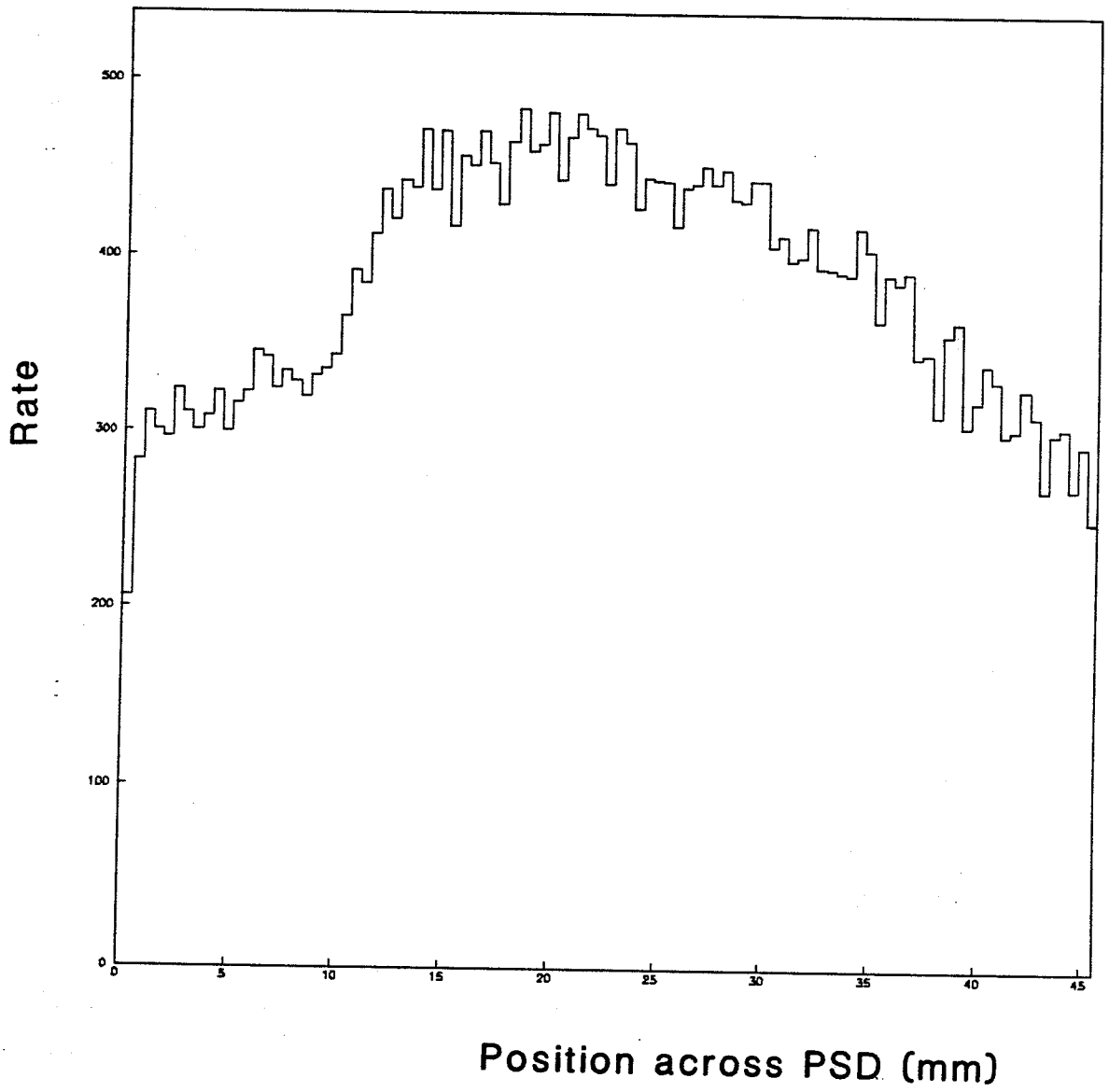

Figure 6.5 Position spectrum of the uncollimated alpha source with full PSD coverage.

intervals of 5 mm. Although the PSDT (energy) scale was very stable, varying by less than 0.8% across the detector, the distortion of the PSDX (position) signal by up to 30% near the ends resulted in a disagreement between the measured and actual positions. The open circles show the correlation between the measured position and the actual position of the source on the test mount. The points demonstrate that particles entering toward the ends are recorded as striking more toward the center than they actually did.

The spectrum in Figure 6.5 was the basis for a polynomial fit used to correct for this non-linearity during analysis. This uncollimated source scan, performed outside tunnel in the test set-up, was chosen so as to reduce the influence of the electronic noise of the tunnel environment on the position signal and in so doing, to isolate the effect of the non-linearity. The correction function $x_{true} = f(x_{measured})$ is shown plotted as the curved line in Figure 6.4. The dark circles show the effect of this correction on the measured collimated source positions; the straight diagonal is drawn to indicate what one would expect for true linearity. That the effect and correction are independent of particle type can be noted in Figure 6.6 where the correction has been applied to the position spectrum of Figure 6.3 (elastic peak events from the arm in a vertical position). Here the uniform position spectrum of protons is "straightened out" with a correction based upon alpha particles. Lastly it must be stressed that the energy signal, and therefore the t scale, was untouched by this correction,

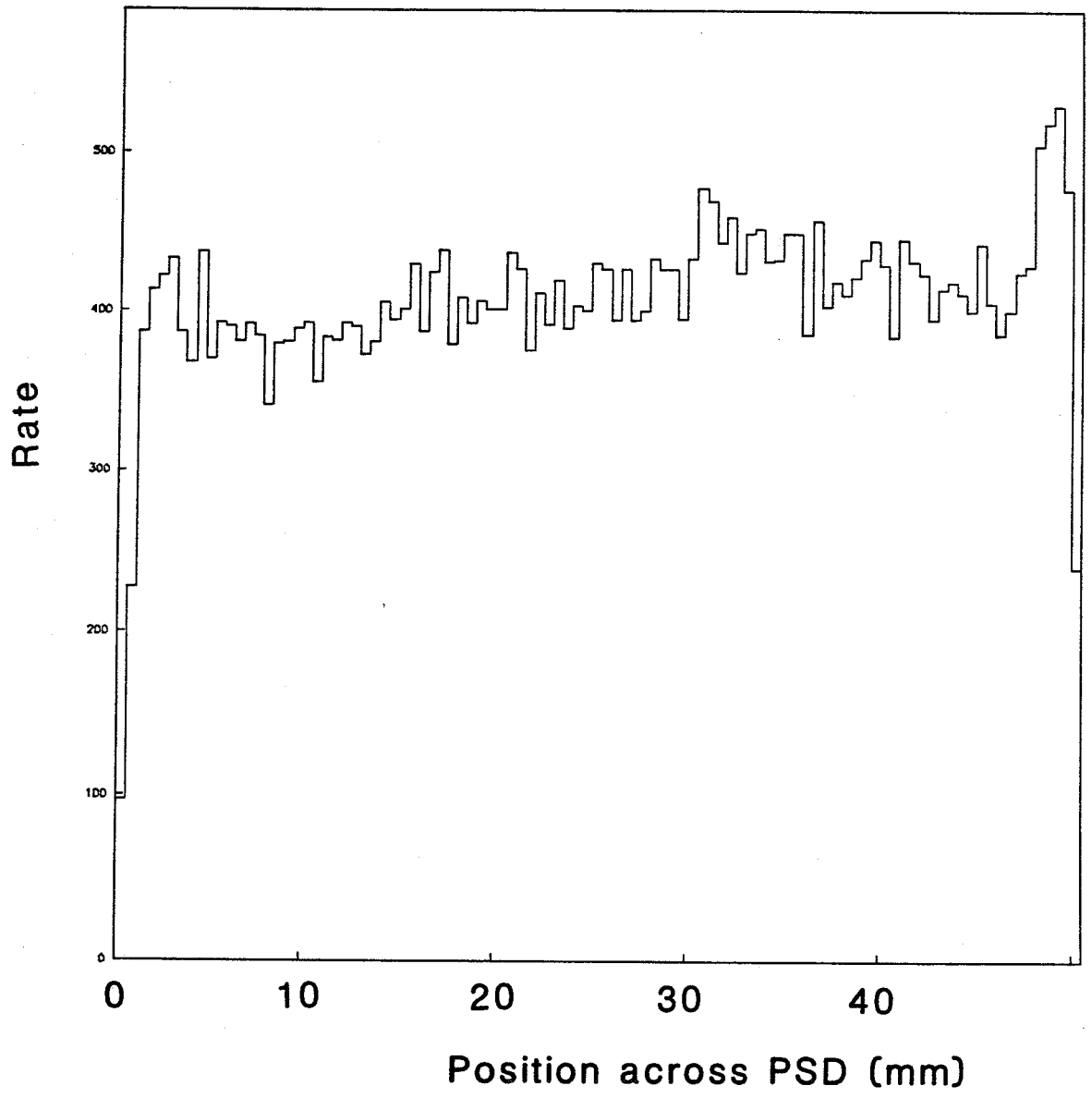

Figure 6.6 Arm vertical data of Figure 6.3 corrected for position non-linearity.

which was performed to increase the reliability of the background subtraction.

6.4 Adjustment of TDC Signal of PSD

In addition to the analysis corrections for TDC slewing and the position non-linearity, the PSD required another small correction to its TDC signal. Probably due to the charge collection properties of the PSD, a particle entering the active area toward one end or the other would register a time-of-flight about 9 ns faster than a particle incident to the center. This is evident in Figure 6.7a which shows two scatter plots of PSD position versus the TDC read-out (with an arbitrary ns scale). Each plot contains events from a different narrow range of energy; the elastically scattered recoils create the localized blobs. The wide band beneath consists of higher energy (hence faster) secondaries in time with the beam passing that penetrate the detector leaving only a small part of their energy. These particles actually arrive at identical times but the PSD distorts their distribution following their entry point, as is made evident by the slight curve in the band.

This distortion was removed during analysis in order to improve the accuracy of TDC cuts in separating these background secondaries from the elastic recoils. A simple quadratic function adjusted the TDC value of an event based on the position measurement before any cuts were performed, resulting in the improvement seen in Figure 6.7b.

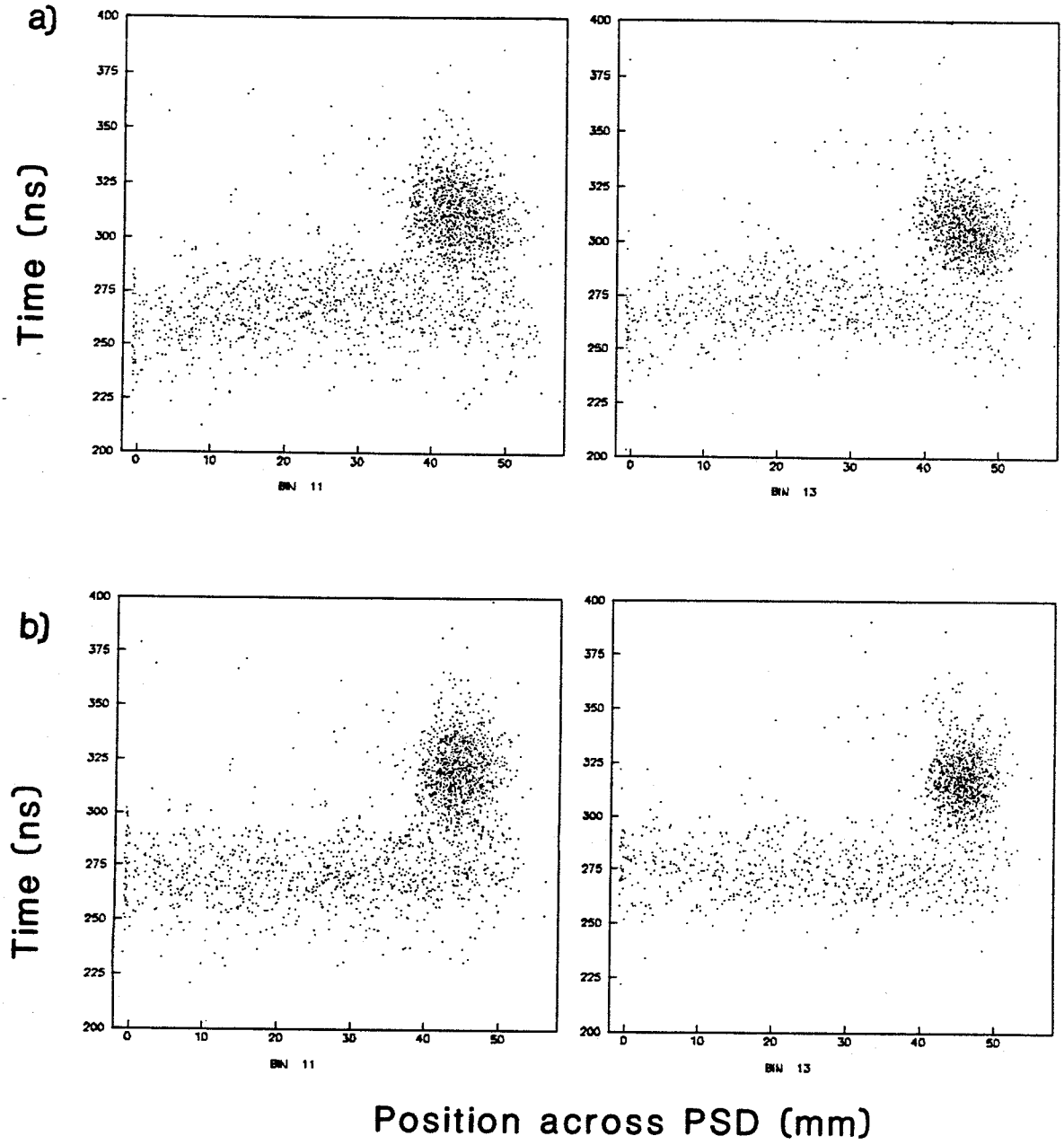

Figure 6.7 a) Uncorrected time versus position for uncut PSD events within two narrow energy bands, b) the same data with the TDC signal corrected for position.

CHAPTER 7 Determination of Luminosity

The luminosity monitors not only gave the normalization with which Run Sets at different angles were combined for the elastic scattering measurement, but also provide the absolute luminosity for the spectrometer arm experiment. For the data collection period of the measurement reported here, several different silicon detectors were employed as luminosity monitors. Therefore even to provide the relative normalization for a Run Set, in addition to the rate of elastic recoils, the solid angle coverage and t range of the particular detectors in operation at that time had to be known.

7.1 Data Collection and Analysis

As mentioned earlier, the pair of detectors used to monitor pp collisions (p-monitors) were not precisely symmetric with the $\bar{p}$-monitor pair with respect to 90° to the beams. Also, anytime the vacuum chamber bulkhead containing the monitors was removed, say to change a detector, all the detectors, even if unchanged, would, when returned, end up at a slightly different angle. It was therefore essential to keep a running energy calibration of the monitors (Section 4.4.1) by which to verify their t acceptance range for each Run Set. During data collection, sufficient alpha particle hits would be accepted by the Beam trigger to enable the energy calibration constants to be determined. Examples of the raw ADC spectra showing the alpha peaks for a proton and an antiproton monitor are shown in

Figure 7.1. TDC information was used to reduce the low energy electronic noise peak above threshold and the spurious background, of which there was very little above the noise. The scattering angle to the detectors was small enough so that the inelastic contribution beneath the elastic peak was not significant.

On rare occasions, the measured pressure in the luminosity vacuum chamber would fluctuate to a level high enough to trip the interlock which would cause the gate valve to close, blocking recoils to the luminosity monitors. When this occured the run would be halted, the valve re-opened and data collection resumed. Runs during any part of which this valve was closed were not included in the analysis. This was verified by keeping track of the ratio of hits in the analyzed detector to hits in the monitors on a run by run basis.

For reasons that were never entirely clear, at various times during the data collection period, the noise signal as monitored by an oscilloscope increased substantially on several of the monitors and remained high permanently. In the attempt to reduce this noise and because of other problems the detectors were sometimes replaced with new ones. The specifications of the devices occupying each of the four luminosity monitor slots is given in Table 7.1. As it turned out, this troublesome noise increase did little but degrade the resolution of the TDC signal, which because of the small backgrounds, did not significantly affect the luminosity determination.

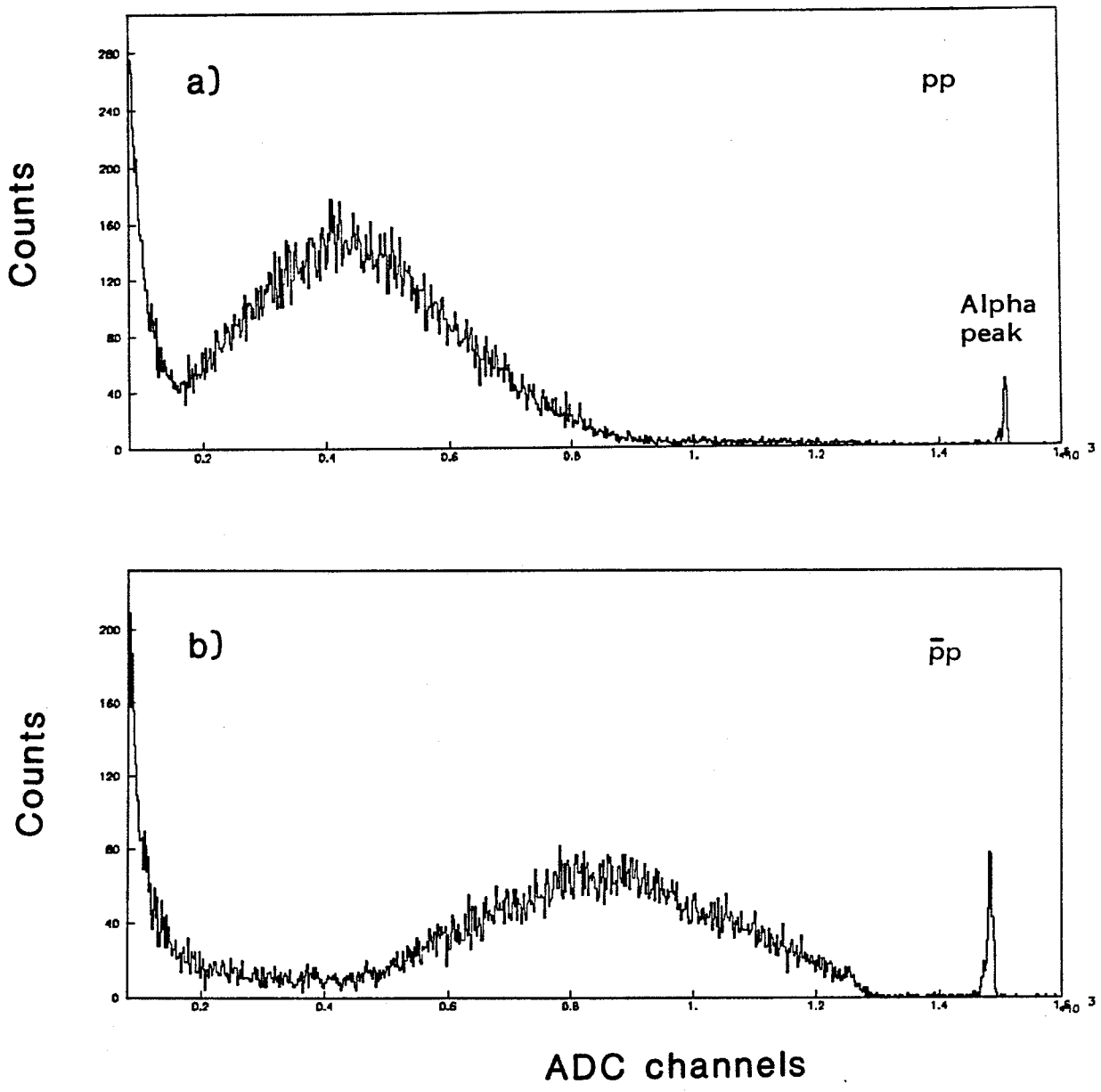

Figure 7.1 ADC spectrum of luminosity events before time cuts, a) proton monitor, b) antiproton monitor. Thin peak is the 5.5 MeV alpha source.

Table 7.1 Luminosity Monitor history

The letters in the chart refer to the detectors in the list below.

Date	Run Number	p1	p2	$\bar{p}1$	$\bar{p}2$
7.9.85	2007 ↓	A	B	C	D
18.9	2132				
---------- Jet housing turned - angle changed ----					
28.9	2144 ↓				
29.10	2572				
31.10	2599 ↓			e	
6.11	2760				
6.11	2763 ↓	f		g	h
19.11	2943				
22.11	2944 ↓	i		j	
23.12	3420				

Detector Specifications

	Serial Number	Nominal Area	Measured Area (mm^2)	Sensitive Depth
A	24-508G	50 mm^2	47.89	.2 mm
B	24-508A	"	48.39	.2
C	24-508D	"	47.14	.2
D	24-508I	"	47.44	.2
e	23-089I	25 mm^2	25.26	.185
f	23-089F	"	24.21	.199
g	23-089G	"	25.58	.200
h	23-089H	"	24.48	.195
i	25-591A	"	28.59	.192
j	25-591I	"	29.37	.190

The nominal area as given on the data sheet supplied by the manufacturer with each detector was either 50 or 25 mm^2. The true active area of this type of silicon barrier detector, however, is determined by how much silicon remains exposed after an epoxy fillet is laid down around the edge by hand. To provide values for the absolute luminosity or to compare relative luminosities determined using different detectors, the active areas had to be accurately measured. Inspired by a suggestion from the manufacturer to try using a microscope [7.1], the active area of each monitor detector used in this analysis was measured using a Bridgeport milling machine with a digital read-out equipped with a 50x centering magnifier. These values are included in Table 7.1. The accuracy is believed to be about 0.5% on the area measurements, which deviate by up to 22% from the nominal figures.

To complete the solid angle determination, the distance from the jet/beam intersection point to the surface of the monitors was measured using a specially made device and found to be 618.3 ± 1.0 mm.

7.2 Calculation by Monte Carlo Integration

To a first approximation, the integrated luminosity associated with N background-corrected elastic recoils into a monitor of solid angle $d\Omega$ is given by

$$L = \frac{\pi N}{(d\sigma/dt)\ 2\ m\ \sqrt{|t|}\ d\Omega} \qquad (7.1)$$

where the elastic differential cross section is evaluated at $|t| = 2mE_{peak}$, E_{peak} being the center of the energy distribution of the events. This assumes that $E_{peak} = 2m \sin^2\theta_c$ where θ_c is the angle to the center of the detector, and that $\frac{d\sigma}{dt}(E_{peak})$ gives the constant differential cross section across the energy range of recoils reaching the detector.

But the obvious asymmetry of the peaks in Figure 7.1 is a result of how $d\sigma/dt$ varies by $|t|$. This is especially important for the p monitors, which ended up at a smaller angle from 90° than the $\bar{p}$ monitors due to the slight twist in the jet housing and thereby cover a range that has a stronger Coulomb contribution. Also ignored in Eq. 7.1 is the enlarged distribution in $|t|$ of recoil protons reaching the monitors due to the width of the jet/beam interaction area. This width was measured by examining the position spectrum of recoils entering the position sensitive detector within a narrow slice of $|t|$. The jet width was found to be well represented by a Gaussian distribution with a FWHM typically 5.2 mm, but this would vary depending upon beam or jet conditions.

A simulation program was written with two purposes in mind: to study the energy distribution of elastic recoils in a luminosity monitor so as to help subtract the remaining background and to calculate the luminosity with precision. Given the energy corresponding to the recoil angle to the center

of the detector and the number of elastics, the program performs three Monte Carlo integrations over jet width, the detector area and the rate variation by |t| based on the differential cross section. The program creates a histogram of the energy distribution of the generated events that can be directly compared with the data. Examples of two such comparisons are shown in Figure 7.2

The program generates each elastic recoil from an origin distributed by a Gaussian with the appropriate FWHM. The recoils are given a |t| distribution following Eq. 2.16 using values for σ_{tot}, b and ρ for pp and $\bar{p}p$ at $\sqrt{s}$ = 24.3 GeV based on parametrizations of measurements made at other energies. Each generated proton is then rejected if it would not hit within the circular shape of the detector. The higher angle of the $\bar{p}$ monitors meant that recoils in the higher energy tail of the elastic peak had sufficient energy to penetrate the typically 0.2 mm thickness of the detector silicon. In that case the full energy of the penetrating particle would not be recorded by the monitor. This had the result of "folding in" the higher energy events to lower values. This effect was reproduced in the generating program following the parametrization of charged particle range in silicon of Eq. 4.1 so as to ensure accurate peak shape for comparing the energy histograms.

Excellent peak shape reproduction was achieved by the simulation program (Figure 7.2). In practice, for determining the luminosity for a Run Set, the rate N was adjusted until the generated spectrum matched the data

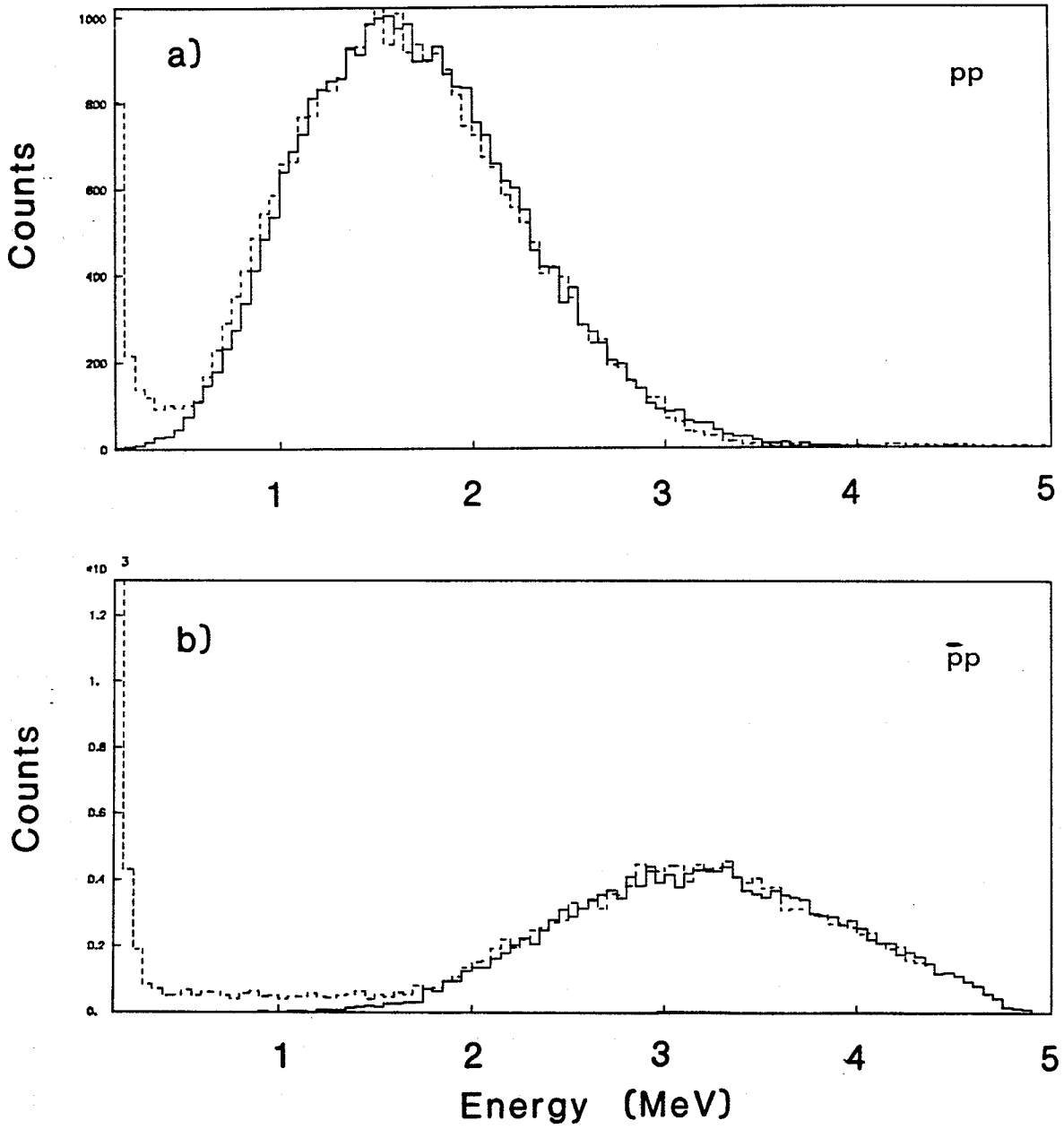

Figure 7.2 Luminosity peaks after time cuts with Monte Carlo simulation peaks superimposed, a) proton monitor, b) antiproton monitor.

over an energy range beginning at a high enough value so that the background was known to be minimal. In this way, the luminosity formula becomes

$$L = \frac{\pi}{2\ m} \sum_{i=1}^{N} \left[\frac{d\sigma}{dt}(t_i)\ \sqrt{|t_i|}\ d\Omega_i \right]^{-1} \qquad (7.2)$$

(where $d\Omega_i$ is used because each generated particle actually sees a slightly different solid angle). Generally excellent agreement was obtained between p1 and p2 or $\bar{p}1$ and $\bar{p}2$ when data from both monitors were available for a Run Set.

CHAPTER 8 Stack Analysis

A solid state detector will either stop a recoil proton or register its traversal. In the first case, the total kinetic energy, E, is recorded while in the latter case dE/dx is recorded. With the use of two detectors, a thin one for dE/dx followed by a thicker detector in which the particle stops, very clean particle identification is possible as discussed in Section 4.4.3. A limiting factor in this approach is that the energy of useful recoils is restricted. For the stack detectors used for this experiment the usable energy range is roughly $15.4 < E < 29.2$ MeV. But in this way the measurement of the elastic differential cross section by the PSD ($0.001 \leq |t| \leq 0.014$ $(GeV/c)^2$) is extended by the stacks to include points within the range $0.03 < |t| < 0.06$ $(GeV/c)^2$ where the Coulomb contribution is insignificant, assuring a more secure measurement of the slope of the forward diffractive peak.

Data collection took place at pivot angles (α) such that only Stacks 1 and 2 had usable elastic peak energies. At each α position of the moveable carriage, only one of these two stacks was placed at an elastic scattering angle, θ, where the elastic peak was predominantly within the back E detector. At the lower end of the θ range some fraction of recoils would stop in the front DE detector, reducing the elastic count in the E detector. Then at the larger angle limit events with energies in the higher energy tail of the elastic peak would penetrate the E detector and leave reduced energy signals but would still be counted as elastics.

Because the front and back detectors in a stack had the same size active areas and the vacuum chamber did not pivot from the interaction point (Figure 4.11), the acceptance of a particular stack for recoils stopping in the E detector had a non-trivial dependence upon the scattering angle. The acceptance relative to angle was carefully calculated for each measurement point after its central scattering angle was determined using a computer simulation of the energy spectrum that is described below. The relative acceptance among the stacks was measured using the data collected while the detector array was rotated to the vertical position as previously described in Section 5.2.2.

For the analysis of the stack data points, a great deal of use was made of a Monte Carlo (MC) program designed to simulate the elastic peaks in the detectors. The MC was used to estimate and correct for losses to the elastic rate and to verify the precise scattering angle pointing to the center of the stack for a particular Run Set. The corrections included that for uncounted protons that stop in the DE detector and for recoils involved in reactions with silicon nuclei. A separate Monte Carlo program based on a functional parametrization was used to estimate and subtract the inelastic background of recoil protons originating from single diffractive dissociation. The procedure for determining the elastic counting rate for the stacks and the corrections incorporated in the MC programs are described in the rest of this chapter.

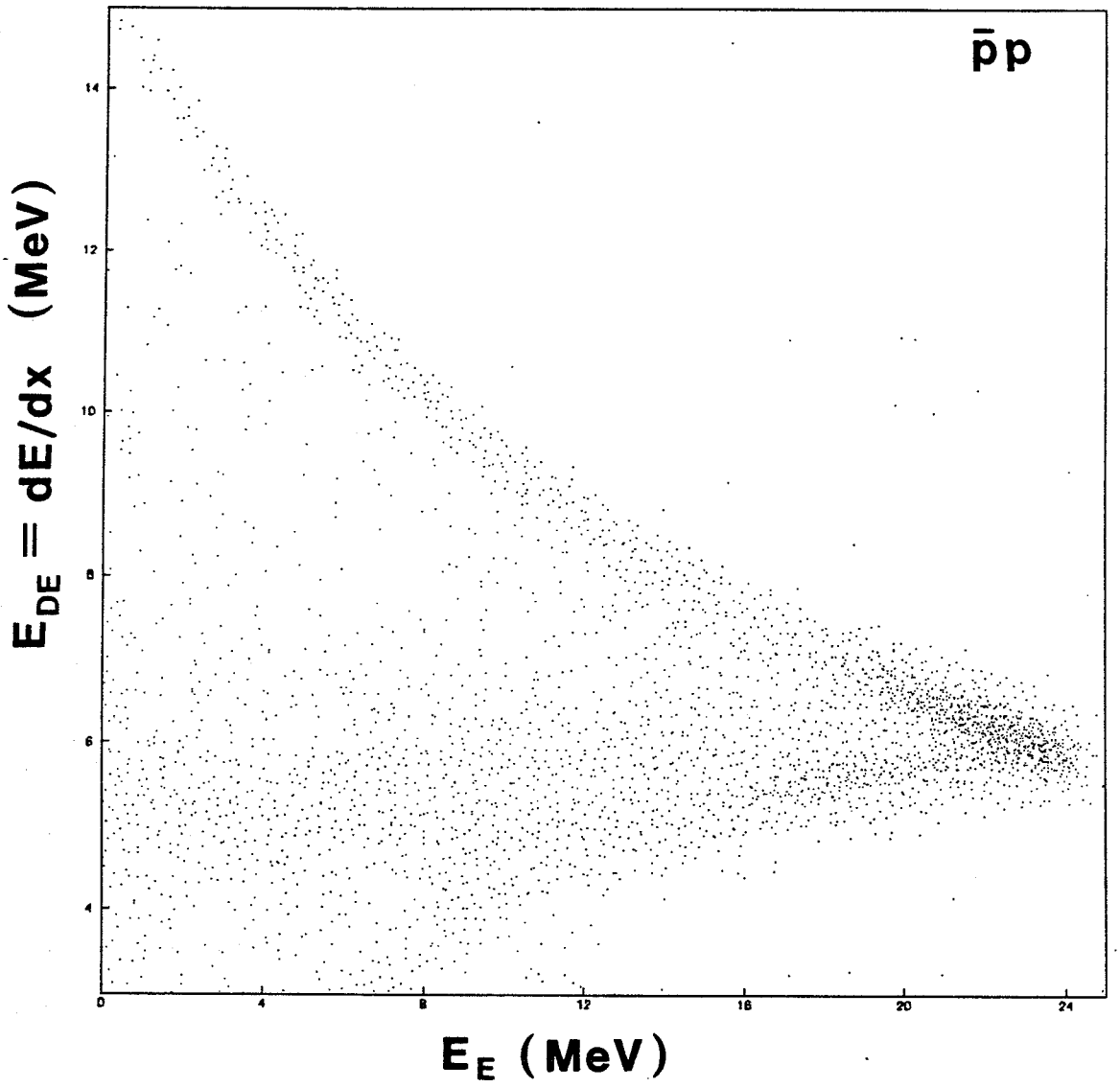

Figure 8.1 Energy measured in the back detector (E) versus energy in the front detector (DE) for Stack 2 at an angle (θ) where a fraction of the elastic $\bar{p}p$ recoils penetrate the E detector.

8.1 Proton Identification

Figure 8.1 shows a scatter plot of E_E, the energy recorded in the back, versus E_{DE}, the energy recorded in the front detector of Stack 2 at θ = 7.1°. The band of elastic and SDD recoil protons is easily identifiable. At this angle, a portion of the elastic recoils are energetic enough to traverse the back detector, hence the bend in the proton band at the E detector energy limit around 24.5 MeV. The protons in this folded-back portion are harder to separate from background.

The recoil protons which stop in the back detector are isolated by the mass ratio formula, Eq. 4.3, as shown in Figure 8.2a,c for two sample angles. Analysis of each stack point began with inspection of the m_r/m peak after loose TDC cuts and the requirement that $E_E > 0.05$ MeV. Often the m_r/m peak would be centered, as expected, within 1% of unity, but for some points there was disagreement by up to several percent. This was due to the occasional slow drift of the DE1 or DE2 calibration as mentioned in Section 6.1. When needed, the DE counter calibration was given a small correction to bring the peak into agreement with unity. This was necessary to ensure that the cut on the mass ratio was consistent among the Run Sets and that the total energy distribution would be correct.

The low leading tail visible on the m_r/m distribution of Figure 8.2a is due primarily to protons that lose some energy unrecorded by the detectors, probably for the most part in passing through the epoxy fillet around the

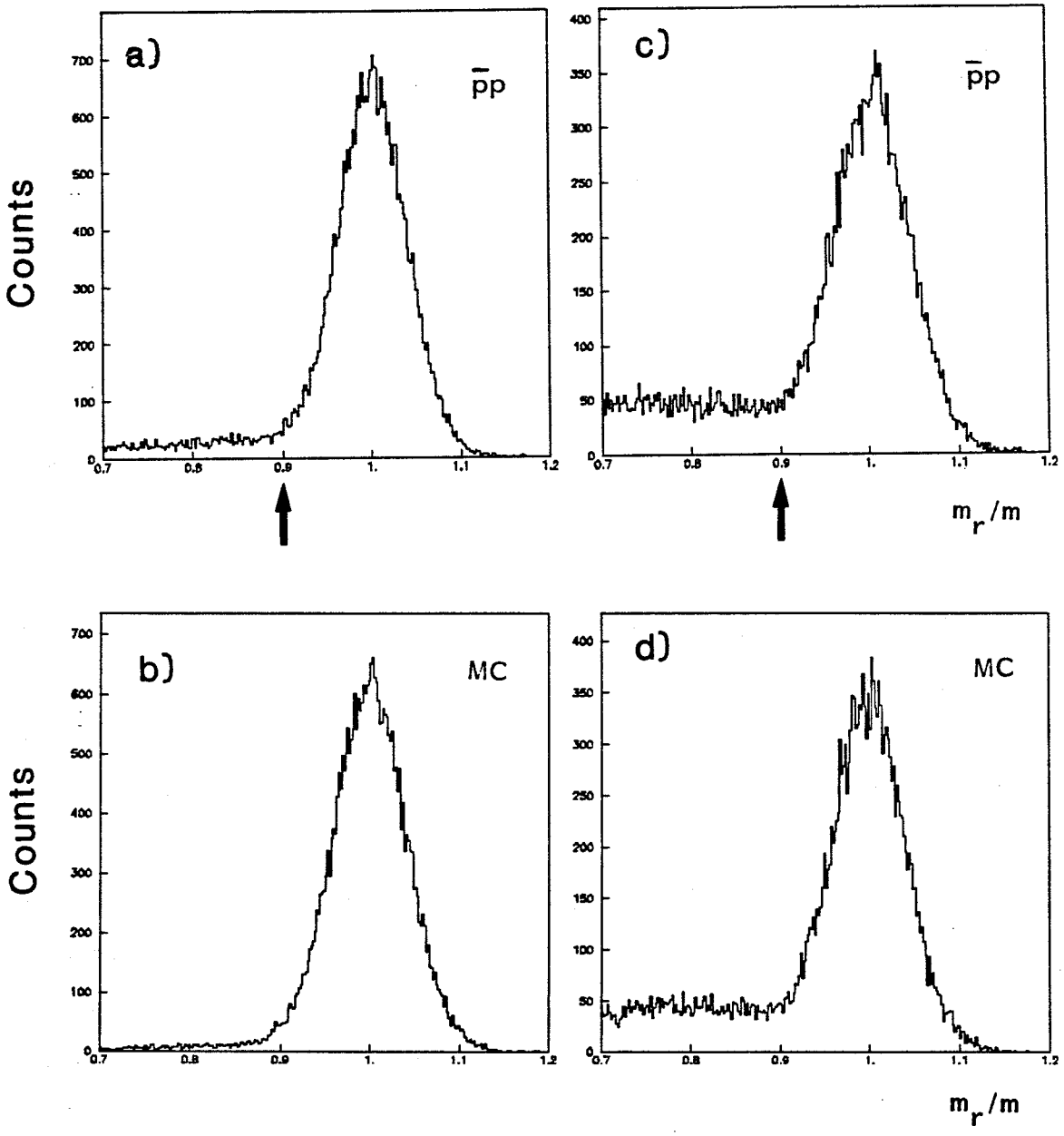

Figure 8.2 Ratio of measured mass to proton mass (m_r/m). a) $\bar{p}p$ data at $\theta = 6.8°$, b) sum of Monte Carlo simulations for elastics and inelastics at this same angle, c) $\bar{p}p$ data at $\theta = 7.1°$, d) MC at same angle. Arrows mark the value of the mass ratio cut.

edge of the silicon active area. This is referred to as an edge effect. In Figure 8.2c showing data at a higher scattering angle, the edge effect tail is supplemented as a result of the recoil protons that traverse the E detector. At all angles, a cut was made removing this tail with $m_r/m < 0.9$ as shown in the figure. The MC was used to correct for losses induced by this cut, important only at the largest angle points. Sample recoil mass ratio distributions generated by the MC are shown in Figure 8b,d.

8.2 The Monte Carlo Program and Acceptance Determination

The data that remained after imposing the mass ratio cut were very clean. In fact there were always so few events in the BDE/BE stack designed to monitor the spurious background that it was unnecessary to use the counting rate in that stack in the background estimate for the other stacks. For the final elastic rate determination it remained only to correct for losses and subtract the recoils originating from SDD.

The MC program proceeded in much the same manner as the program described in Chapter 7 to calculate the luminosity. Again, elastic recoils were generated following a Gaussian jet width and given a reasonable $|t|$ distribution (practically flat at these larger angles) then retained if they reached the back detector and passed the same cuts as were applied in analysis to the data being studied.

Due to the chamber pivot angle and less importantly to the finite width of the origin, recoils were not incident perpendicularly to the stacks. This meant that the active area of the front DE detector as seen by the incoming particles was reduced slightly as an ellipse. Also, the effective thickness of the DE detector that the particles had to traverse to reach the E detector was increased over the nominal thickness of Table 4.1 since the incident paritcles enter the detector at an angle. A representative value of this effective thickness is given for each available angle in the pp and $\bar{p}p$ stack analysis in Table 8.1, but in the MC the effective thickness was re-calculated depending on the angle of each generated event. The proton was then tested for passage through the DE detector using Eq. 4.1.

The separation of the front surface of the DE detector from the front surface of the E detector was measured to be about 15.1 mm. The effective active area of a stack, therefore, was given by the overlap of the DE area projected through this distance onto the E detector along the generated angle of scattering, θ. Calculated in this way and assuming the nominal 100 mm^2 detector area, the effective stack acceptance areas and the resulting solid angles are listed in Table 8.1. These values, it should be remembered, are relative, and for the final values of the differential cross section represented by each point, the overall normalization will be left a free parameter. The relative variation of acceptance by scattering angle of the three stacks is plotted in Figure 8.3 as a percentage of the solid angle coverage of the E detector at $\theta = 0°$.

Table 8.1 Angles of stack measurement points, weighted |t| values and angle-dependent parameters.

θ (°)	Stack Number	[1]E (MeV)	[2]Wtd. |t| (GeV^2)	[3]Pen. dep. (μm)	Stack Effective Thickness DE(μm) (MeV)		E(μm) (MeV)		Stack Accp. (mm^2)	dΩ (10^{-4}sr)
pp										
5.62	1	18.00	.0344	1979	1509	15.39	2987	22.85	91.8	1.249
5.68	1	18.39	.0351	2054	1509	15.39	2987	22.85	91.7	1.247
5.97	1	20.32	.0388	2439	1510	15.39	2987	22.85	90.9	1.237
6.49	2	23.97	.0457	3244	1502	15.34	3060	23.17	89.6	1.204
6.76	2	25.99	.0496	3732	1502	15.35	3061	23.17	88.8	1.192
7.05	2	28.30	.0540	4323	1503	15.35	3061	23.17	87.8	1.178
$\bar{p}p$										
5.83	1	19.38	.0370	2247	1509	15.39	2987	22.85	91.3	1.242
5.85	1	19.50	.0372	2272	1510	15.39	2987	22.85	91.3	1.241
6.18	1	21.75	.0415	2744	1510	15.39	2988	22.85	90.4	1.229
6.20	1	21.86	.0417	2768	1510	15.39	2988	22.85	90.3	1.228
6.76	2	26.04	.0497	3744	1502	15.35	3061	23.17	88.8	1.192
7.07	2	28.40	.0542	4350	1503	15.35	3061	23.18	87.8	1.177
7.10	2	28.66	.0546	4419	1503	15.35	3061	23.18	87.6	1.176

[1]Recoil kinetic energy associated with angle θ to center of stack.

[2]Associated momemtum transfer weighted as explained in the text.

[3]Penetration depth in silicon for protons of this energy.

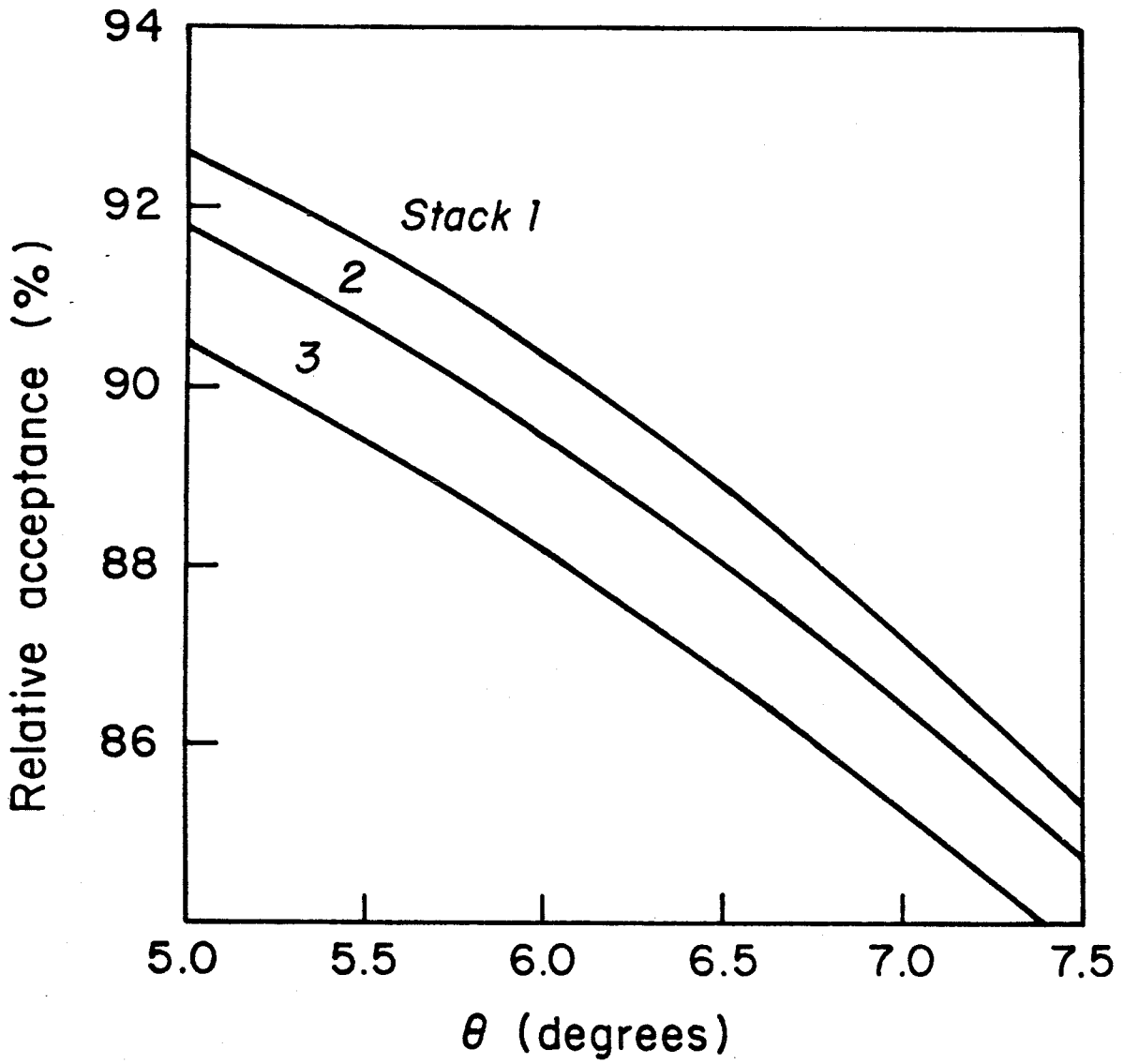

Figure 8.3 Relative acceptance by scattering angle of Stacks 1, 2 and 3 as a percentage of the solid angle coverage of the rear (E) detector at $\theta = 0°$.

The relative acceptance among the stacks was determined using the pp runs taken with the detector array turned 90° to a vertical position and the carriage moved to an angle where elastic recoils would come to rest in the back detector. The results are presented in Table 8.2. The counting rates for each stack were determined following the usual analysis procedures and are given as a relative percent of the rate in Stack 1. Although the stacks were all at the same scattering angle so as to simultaneously intercept the same energy recoils, their different distances from the detector arm rotation point (Figure 4.11) meant that each had a different solid angle coverage originating from geometry alone. These were calculated and are also presented in the table as a percentage of the first stack coverage. Correcting the rate measurements for these differences gave the relative rate correction factors of the last column, for which the listed errors are statistical. Since only points from Stacks 1 and 2 were used in the elastic scattering measurement, the practical effect of this correction was that the elastic recoil rates for those angles that used Stack 2 had to be increased by 1.0%.

Table 8.2 Relative acceptance of stack detectors measured with the array in vertical position. Measurements of Stacks 2 and 3 are relative to Stack 1.

Stack Number	Raw counting rate (%)	Comparative eff. solid angle (%)	Relative rate correction factors
1	(100)	(100)	(1)
2	93.6 ± 0.7	94.5	1.010 ± 0.011
3	91.0 ± 0.7	89.1	0.980 ± 0.010

8.3 Nuclear Correction

A recoil proton involved in an interaction with a silicon nucleon before it has slowed to a stop by ionization losses will have a smaller than normal detector pulse height. Due to the mass cut, events where the recoil particle undergoes a nuclear interaction in the detector will often be lost to the measured counting rate. A statistical simulation of this effect was included in the MC and thereby contributed to the overall loss correction. In the energy region of a few MeV, the nuclear interaction cross section is relatively independent of energy. A relationship useful for estimates of the macroscopic interaction cross section, Σ, for incident protons is given by

$$\Sigma = 0.032/A^{1/3} \quad cm^2/g \tag{8.1}$$

where A is the atomic number of the absorber [8.1]. In the case of silicon this becomes $\Sigma = 0.00309 \quad mm^{-1}$. The fraction, f, of recoil protons that undergo a nuclear interaction in one of the detectors is then

$$f = 1 - e^{-s\Sigma} \tag{8.2}$$

where s is the range of the recoil particle in millimeters. In any stack, less than 1.5% of the recoils would be involved in a nuclear interaction and typically half of these would not be counted. In the MC program, the appropriate fraction of events depending on the generated range was randomly

assigned a shorter penetration depth, and the simulated measured energy recalculated accordingly.

8.4 Detector Resolution and |t| Value Determination

Events generated in the MC that survived the entry into the back detector were added to histograms of the mass ratio, m_r/m, and of the DE energy, E energy and measured total energy in the following manner. (Each of these histograms had the same specifications as the corresponding histogram of the cut data from the particular stack and Run Set under study.) If a recoil was generated at angle θ that would successfully land within the acceptance of the back detector, its total energy was then $E = 2m \sin^2\theta$. Then if E was less than required to exceed the effective DE thickness (Table 8.1) the generated recoil was counted toward the correction for that portion of events in the data that stopped in the front detector. Provided that E exceeded this amount, the remaining energy was tested for penetration of the back detector and if it indeed penetrated, the reduced energy using Eq. 4.1 was assigned to E_E, the generated energy in the back detector. Otherwise, the majority of particles stop in the rear detector and $E_E = E - E_{DE}$. Next, to give a width to the generated m_r/m distribution, the detector resolution was simulated by giving independent fluctuations to E_{DE} and E_E following Gaussian distributions with standard deviations equal to a common proportion of the square root of the detector thickness. This proportion was varied as necessary so that the MC would match the width of the mass ratio peak from the data of the Run Set under analysis. In this

way, the MC program could accurately correct for any inefficiency in the mass ratio cut as the m_r/m peak width varied depending on the run conditions.

In the same way as in the MC program for determining the luminosity, the jet width FWHM was also chosen in the simulation to give the best agreement with the data. Generally there was close correspondence between the jet FWHM called for by the luminosity peaks and that called for by the stack energy peaks for the same Run Set. Finally through several iterations of the MC program, the scattering angle pointing to the center of the stack was determined that led to the most accurate simulation of the energy peaks[1]. The values of θ along with the corresponding central elastic energy, E, are given in Table 8.1 for the Run Sets used in the stack analysis. However, since for elastic recoils, the detector |t| coverage varies across the solid angle by the square of the angle (Eq. 2.4), a small correction to the |t| value corresponding to the data point must be introduced by finding the weighted center of the back detector acceptance area. The final weighted |t| values to which the differential cross section measurements were associated are given in the table.

---

1. Found in this way, the central scattering angle was usually somewhat different from the angle that would have been suggested simply by finding the center of the total energy peak, which is distorted from symmetry by the various losses, traversals and the varying cross section across the solid angle coverage.

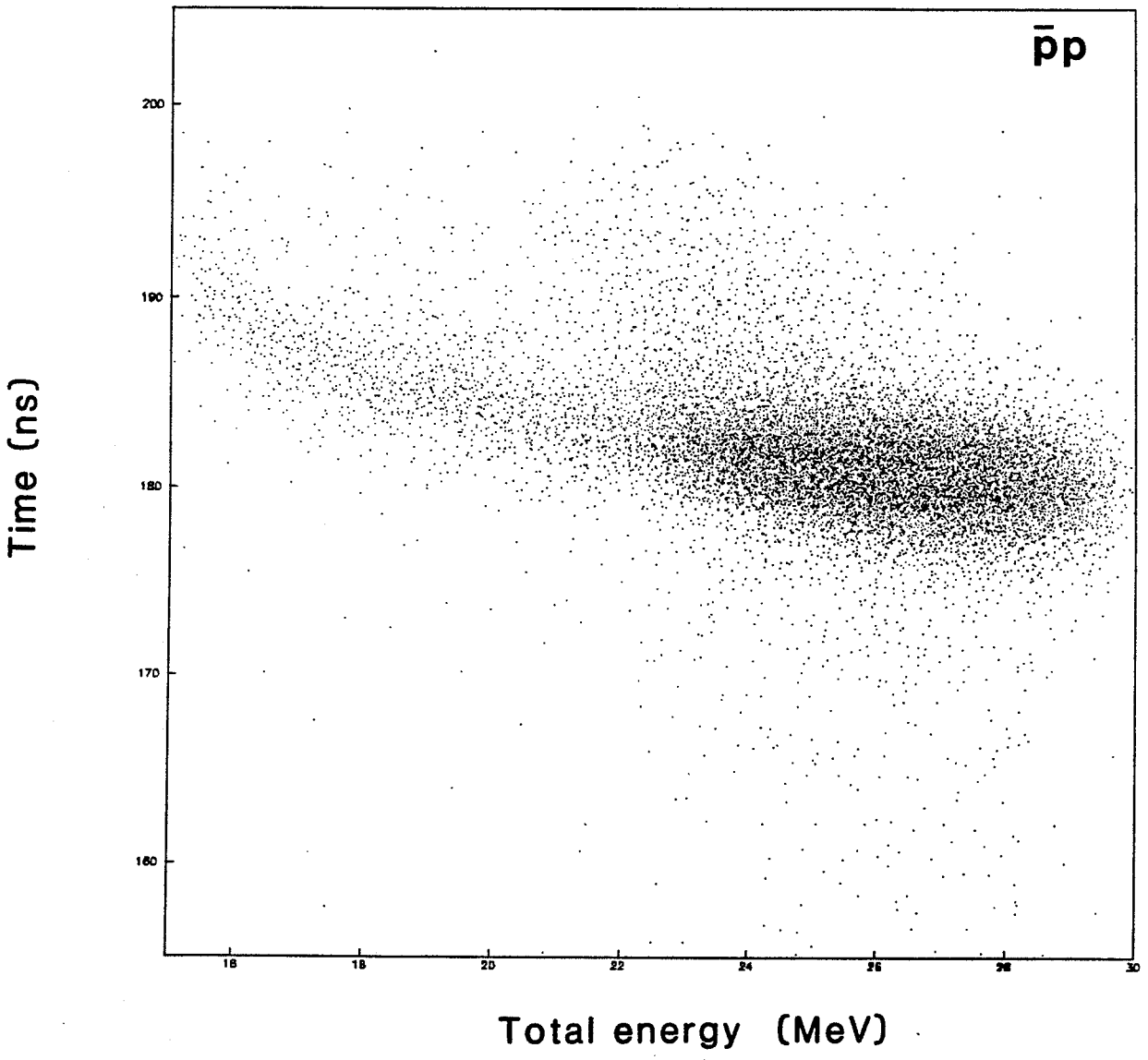

Figure 8.4 Total stack energy (sum of front and rear detector measurements) versus time measurement for $\bar{p}p$ data at $\theta = 6.8°$. The tail of inelastic recoils is visible trailing off to the left.

8.5 Parametrization of Inelastic Recoils

The forward scattered particle in a pp or $\bar{p}p$ interaction has a probability of diffractive excitation, an inelastic process that distorts the kinematics of the slow recoil proton as compared to elastic scattering. From Eq. 2.3, for fixed θ and $M_x^2 > m^2$ it can be seen that the inelastic recoils will be shifted somewhat lower in energy, and therefore will arrive somewhat later in time. But due to the finite detector size and resolution the separation is not complete, as can be seen in the scatter plot (Figure 8.4) of $\bar{p}p$ data from Stack 2 at $\theta = 6.8°$. The total energy found by summing the two stacks is plotted versus an arbitrary time scale for those recoils which satisfy the $m_r/m > 0.9$ cut. The dense area contains the elastic events and the inelastic proton recoils are visible trailing off to lower energies and slower times up to the minimum energy limit of the detector at about 15.4 MeV.

The contribution of the inelastic recoils that overlap into the elastic kinematic region could be calculated to sufficient accuracy for its subtraction as a background based on measurements of the corresponding excitation cross sections. A parametrization of the differential cross section $d^2\sigma/dtdM_x^2$ from data collected at Fermilab by the USA-USSR Collaboration [8.2] was used in a Monte Carlo program that simulated the detector geometry in exactly the same way as the elastic MC previously discussed. Using a gas-jet target and silicon recoil detectors, the Fermilab experiment of Kuznetsov et al. measured the double differential

cross section of the inclusive reaction pp → Xp in the ranges $0.001 \leq |t| \leq 0.017$ $(GeV/c)^2$ and $1.2 \leq M_x^2 \leq 8.0$ GeV^2 for incident momenta from 50 to 400 GeV/c. The data had only a weak dependence on s and were combined and normalized to $p_o = 300$ GeV/c, then fitted with

$$\frac{d^2\sigma}{dt\, dM_x^2}(t, M_x^2) = A(M_x^2)\, e^{b(M_x^2)\cdot(-|t|+0.01)} \tag{8.3}$$

resulting in empirical parametrizations for $A(M_x^2)$ and $b(M_x^2)$ starting with assumed functional forms. Figure 8.5 shows the parametrization $d\sigma/dM_x^2$ (integrated over t) as a function of M_x^2. Kuznetsov et al. found that the $b(M_x^2)$ values to be in good agreement with data obtained at larger |t| values in other experiments on the diffractive dissociation of nucleons [8.3].

In the MC, the origin, θ and t value of an inelastic event were generated, then the resulting value for M_x^2 was calculated from Eq. 2.2b. The events were kept for the simulated inelastic distributions for subtraction only as they followed Eq. 8.3 and would successfully penetrate into the active area of the rear stack detector. The inputs required by the MC (the jet width FWHM, detector resolution factor and detector center angle) were always the same as those that had been required by the elastic MC to reproduce the elastic peaks accurately. The parametrization was assumed to be valid for estimating the distributions of both pp and $\bar{p}p$ inelastic recoils, and excellent agreement was obtained in both cases over

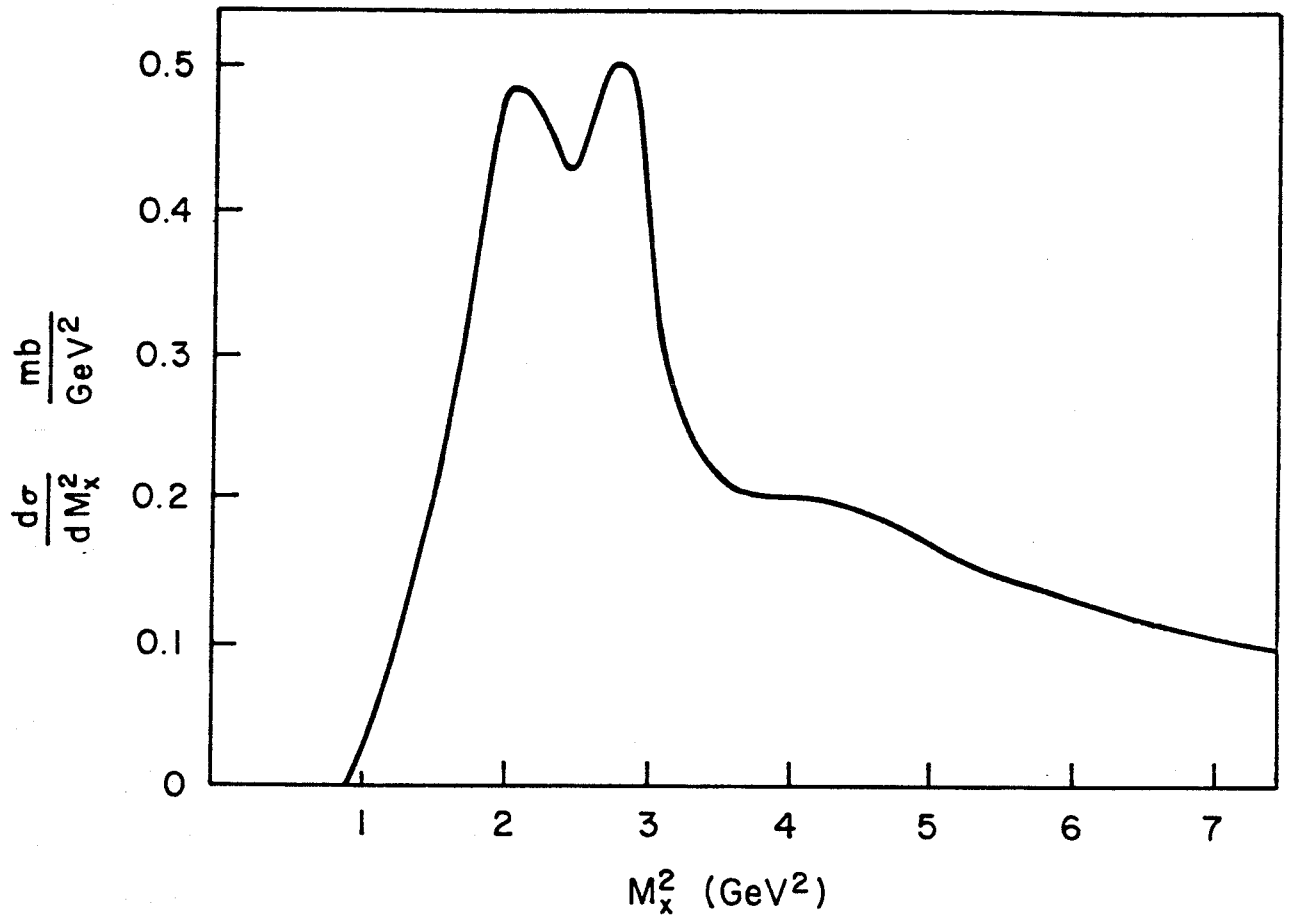

Figure 8.5 Differential cross section $d\sigma/dM_x^2$ versus M_x^2 (integrated over t) for pp → Xp scaled to 300 GeV/c laboratory momentum from Ref. 8.2.

that part of the inelastic spectrum not underneath the elastic peak.

8.6 Elastic Rate Determination

For the final histograms of the recoil proton energy distributions, a sharper TDC cut was applied to the data at each value of θ to reduce the remaining background. The cut was made partially energy-dependent to preserve the band of recoils originating from inelastic collisions for comparison to the MC. An example of the final analysis procedure is presented in Figures 8.6 through 8.8 for a $\bar{p}p$ Run Set at $\theta = 6.8°$.

Figure 8.6 and 8.7 depict identical histograms of data for the DE detector energy, E detector energy and total energy. All three distributions contain only those events satisfying the data cuts, that is, that are expected to be elastic or inelastic recoil protons coming to rest in the E detector. The calculated inelastic MC distributions alone are shown superimposed on the data in Figure 8.6 and the sum of the inelastic and elastic MC distributions are superimposed in Figure 8.7 in order to show the quality of the MC calculations. In each case the number of events generated in the MC distributions were determined by what best matched the data. The inelastic MC distributions are subtracted from the recoil data peaks leaving the final count of elastics that enter the rear detector as in Figure 8.8 for our example angle. MC peaks comprising only the elastic recoils are shown superimposed here. It then remains only to correct the

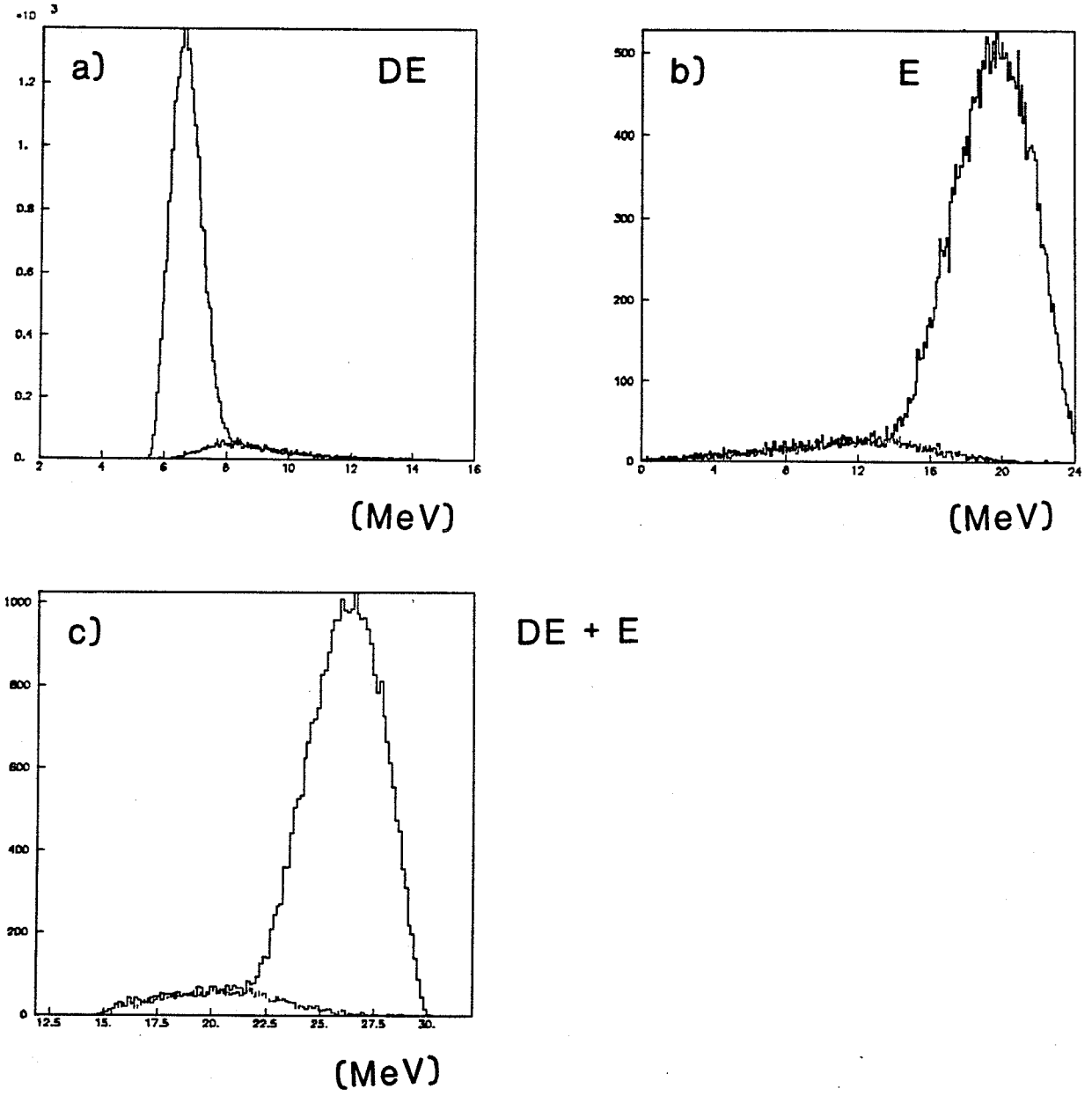

Figure 8.6 Measured energy (solid lines) for $\bar{p}p$ at $\theta = 6.8°$ with inelastic MC simulation superimposed (dashed lines) for **a)** front (DE) detector, **b)** back (E) detector, **c)** sum (DE+E).

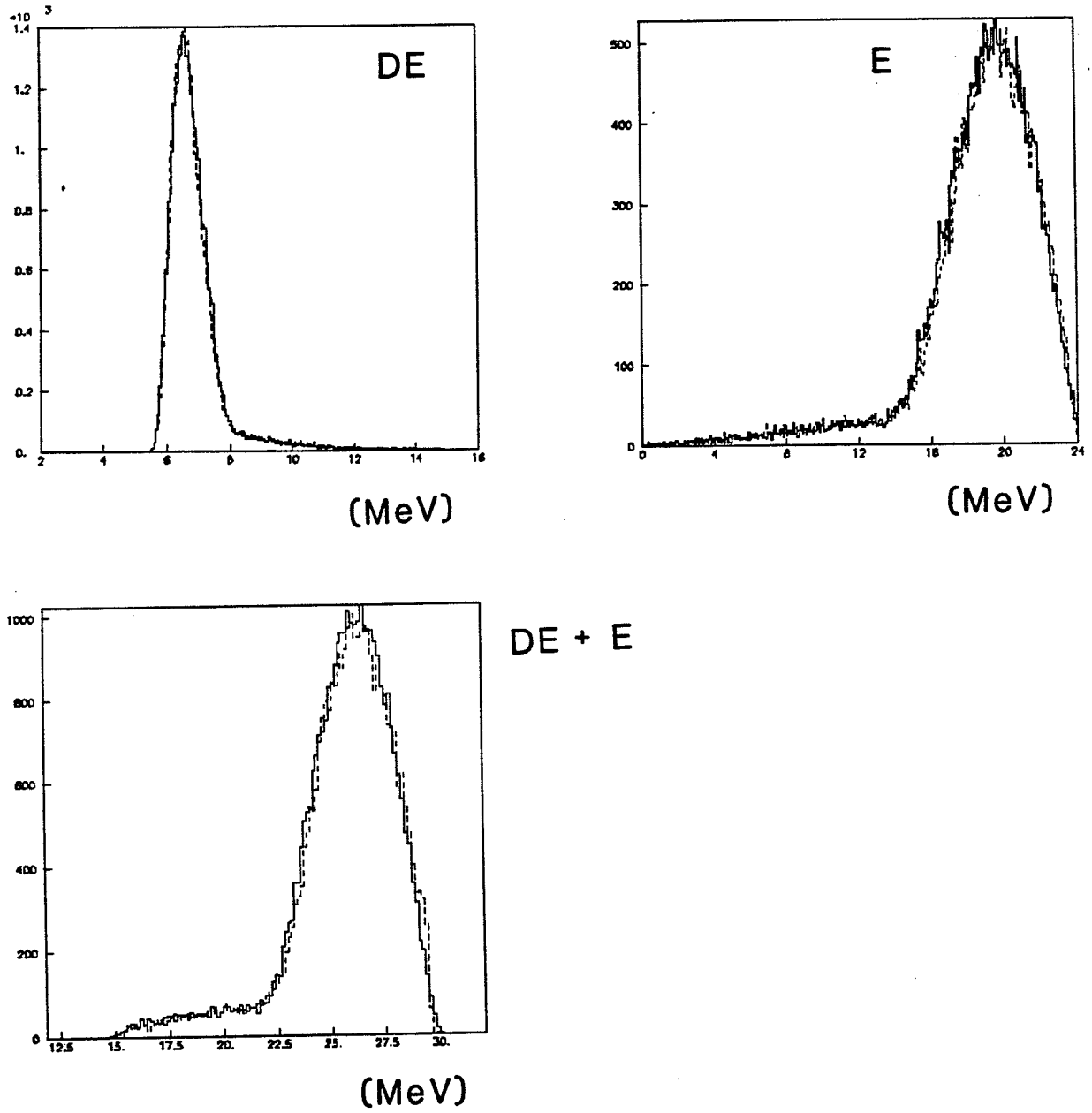

Figure 8.7 Same data as previous figure with sum of elastic and inelastic MCs superimposed.

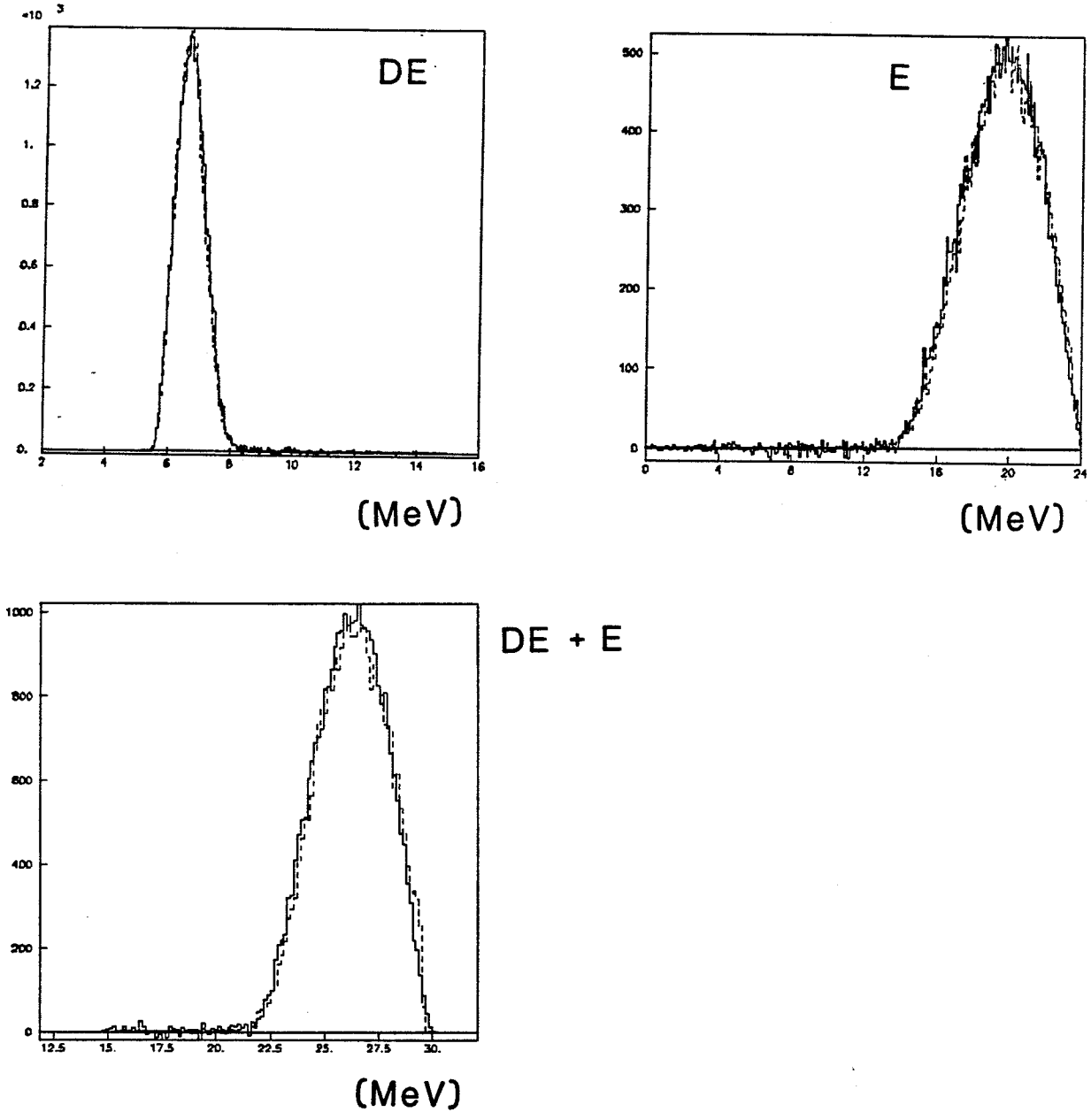

Figure 8.8 Same data as previous figures with MC inelastics subtracted. Dashed line is the elastic MC.

count within an appropriately limited energy range of the total energy histogram for losses using the elastic MC program. (The DE and E detector elastic peaks were used to verify the analysis procedures.)

Table 8.3 again lists the final weighted |t| values of all the stack points used in the pp and $\bar{p}p$ analysis, this time along with the associated luminosities and the elastic counting rates corrected for both losses and the relative acceptance of Stacks 1 and 2. The MC correction factors give the fraction of the total number of elastic events generated within the stack acceptance region that end up stopping in the rear detector and that pass the appropriate cuts used to analyze the associated data. The corrected rates enter as ΔN into Eq. 2.19 for the differential cross section calculation, but the final values will depend upon the overall normalization of the fit as discussed below.

Table 8.3 Elastic counting rates for Run Sets included in the stack analysis. Luminosity errors are statistical, elastic count errors are explained in the text.

[1]Run Set	$\|t\|$ (GeV^2)	Luminosity (nb^{-1})	[2]Monte Carlo corr. factor	Corrected elastic counts (/1000)
pp				
P21	0.0344	52.2 ± 0.3	0.979	31.9 ± 0.2
P22	0.0351	128.4 ± 0.5	0.957	78.7 ± 0.3
P51	0.0388	59.2 ± 0.4	0.993	37.0 ± 0.2
P01	0.0457	52.0 ± 0.3	0.988	30.8 ± 0.2
P02	0.0457	65.0 ± 0.4	0.988	38.9 ± 0.2
Ph1	0.0496	38.3 ± 0.3	0.984	22.9 ± 0.2
P11	0.0540	64.2 ± 0.4	0.697	36.2 ± 0.3
$\bar{p}p$				
Pb22	0.0370	30.7 ± 0.2	0.986	20.4 ± 0.1
Pb23	0.0372	41.3 ± 0.4	0.990	27.4 ± 0.2
Pb24	0.0372	42.9 ± 0.4	0.990	29.8 ± 0.2
Pb52	0.0415	37.6 ± 0.4	0.989	26.2 ± 0.2
Pb51	0.0417	46.1 ± 0.4	0.983	32.0 ± 0.2
Pb05	0.0496	66.9 ± 0.4	0.957	41.6 ± 0.2
Pb03	0.0497	18.3 ± 0.2	0.955	11.8 ± 0.1
Pb04	0.0497	49.1 ± 0.3	0.955	30.7 ± 0.2
Pbh2	0.0542	24.2 ± 0.2	0.765	14.9 ± 0.2
Pbh3	0.0546	34.4 ± 0.3	0.723	20.7 ± 0.2

[1]Run Set labelling explained in Chap. 5; "5" is (5/2)°, "h" is (1/2)°.
[2]MC correction factor is proportion of elastics that stop in rear detector. (Does not include stack relative acceptance.)

CHAPTER 9 PSD Analysis

The resolution and thickness (0.8 mm) of the PSD limited acceptance of recoil protons to energies $0.5 < E < 10$ MeV, with recoil angles in the range $16 < \theta < 73$ mrad. TDC information was recorded with time-of-flight values between 30 and 120 ns. Because the elastic recoil angle and t-o-f are both related to the energy, the simultaneous measurement of energy, position and time provided excellent background control.

Data were collected at several small pivot angles as listed in Table 5.1. Each Run Set was analysed separately then combined using the measured integrated luminosities. Briefly, analysis proceeded as follows. Based on the energy calibration, events were binned by $|t|$ and the elastic and inelastic recoils were isolated with time cuts for each Δt interval. From the distribution of events within these cuts across the PSD, a constant background level was determined and subtracted. Also, a correction was made for any loss of the tail of the elastic peak (approximately Gaussian) which would have extended beyond the physical edge of the PSD. The contribution to this peak from single diffractive recoils was estimated from the same parametrization used in the stack analysis.

At each pivot angle, the position peak of the lowest few Δt intervals was too close to the low angle edge of the PSD to allow adequate background determination. For such an interval, only the time information could be used for background estimation, which was well fit with a Gaussian and the

extrapolation beneath the recoil proton t-o-f peak was subtracted. The constant background level was estimated by averaging over a t-o-f interval above the recoil peak range.

The total integrated luminosity available for the PSD analysis for pp was 366 nb^{-1} and for $\bar{p}p$ was 526 nb^{-1}, yielding respectively about 525,000 and 355,000 measured elastic recoils. Details of the PSD analysis are given in the chapter sections that follow.

9.1 TDC Analysis

Following energy calibration and the corrections to the time and position signals described in Chapter 6, the analysis program divided the PSD data from one Run Set into bins of $|t|$ based on their energy measurements. The width of the bins, Δt, was increased slowly as $|t|$ increased and the rate dropped off so that the bins beyond the Coulomb region would have approximately the same statistical error. Events within each narrow Δt interval were further analyzed beginning with their time distribution. Figure 9.1 shows qualitatively the TDC signal by $|t|$ bin for the pp Run Set P11. Such a distribution was "sliced" into the Δt intervals so that the TDC cuts could be assigned.

Except for the lowest $|t|$ bins where the position distribution was not usable, a fairly generous TDC acceptance window was assigned to the data in each interval so as to preserve as many of the recoil protons as possible.

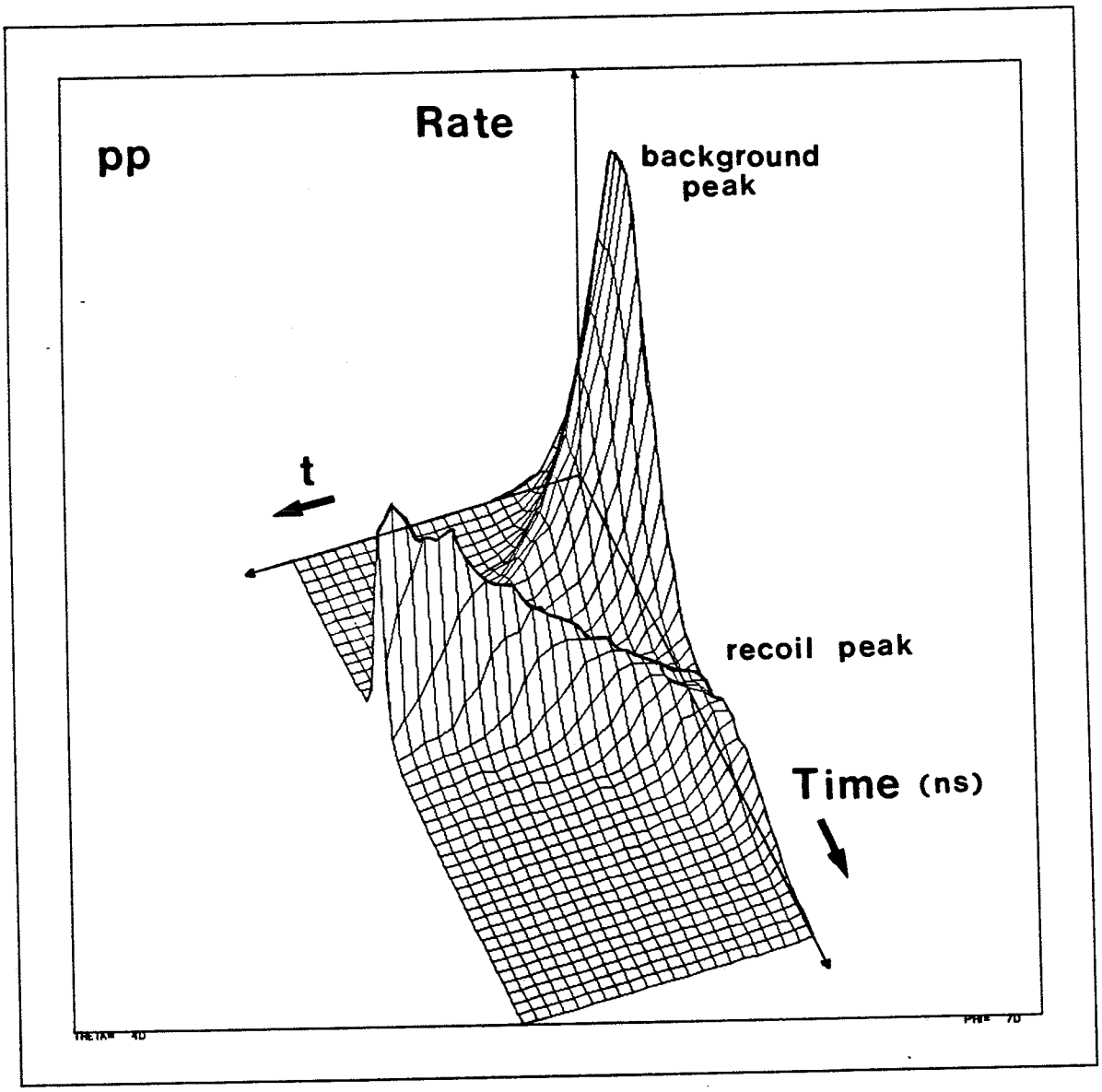

Figure 9.1 Example of the PSD time distribution by |t| bin.

Further background separation was then obtained using the position measurement. An example of the time spectra for a series of Δt intervals is shown in Figure 9.2 for Pb21. A Gaussian fit to the recoil TDC peak was used to estimate any inefficiency of the lower limit of the TDC window ("completing the Gaussian"). This correction was usually negligible except for some lower |t| bins in which the background overlapped strongly into the signal. In that case the correction could be up to a few percent.

The angular spread of recoils increases for lower |t| since

$$\Delta\theta = \frac{\Delta t}{4m\sqrt{|t|}} \quad . \tag{9.1}$$

As the position peak widened and the scattering angle decreased toward the lower |t| bins, eventually the elastic peak was not separated sufficiently from the lower PSD edge for the position spectrum to be used for further background determination (see Figure 9.5). At the same time, background associated with the beam bunch passing at these very low energies was very large, as was seen in Figure 9.1, but the t-o-f separation for the slow recoils was also large.

Figure 9.3a shows the time spectrum of data from the lowest |t| bin used in the analysis from one Run Set. The large peak contains background and the smaller peak about 90 ns later contains the recoil protons. The large background peak was in time with the passage of the beam bunches and presumably represents higher energy secondaries which penetrated through the

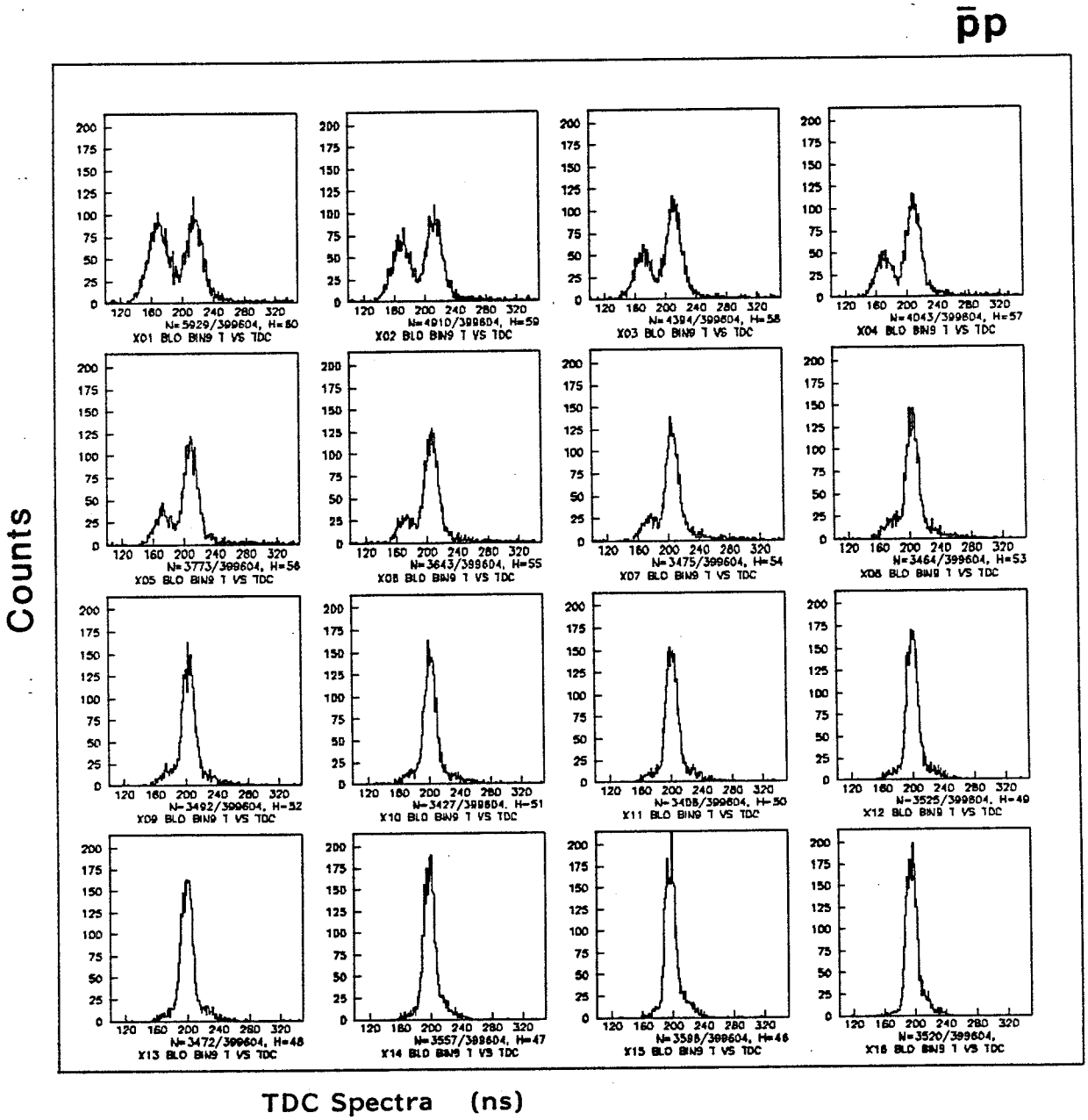

Figure 9.2 Time spectra without cuts from succesive Δt intervals of Pb21. Data are from the same bins as in Figure 9.5.

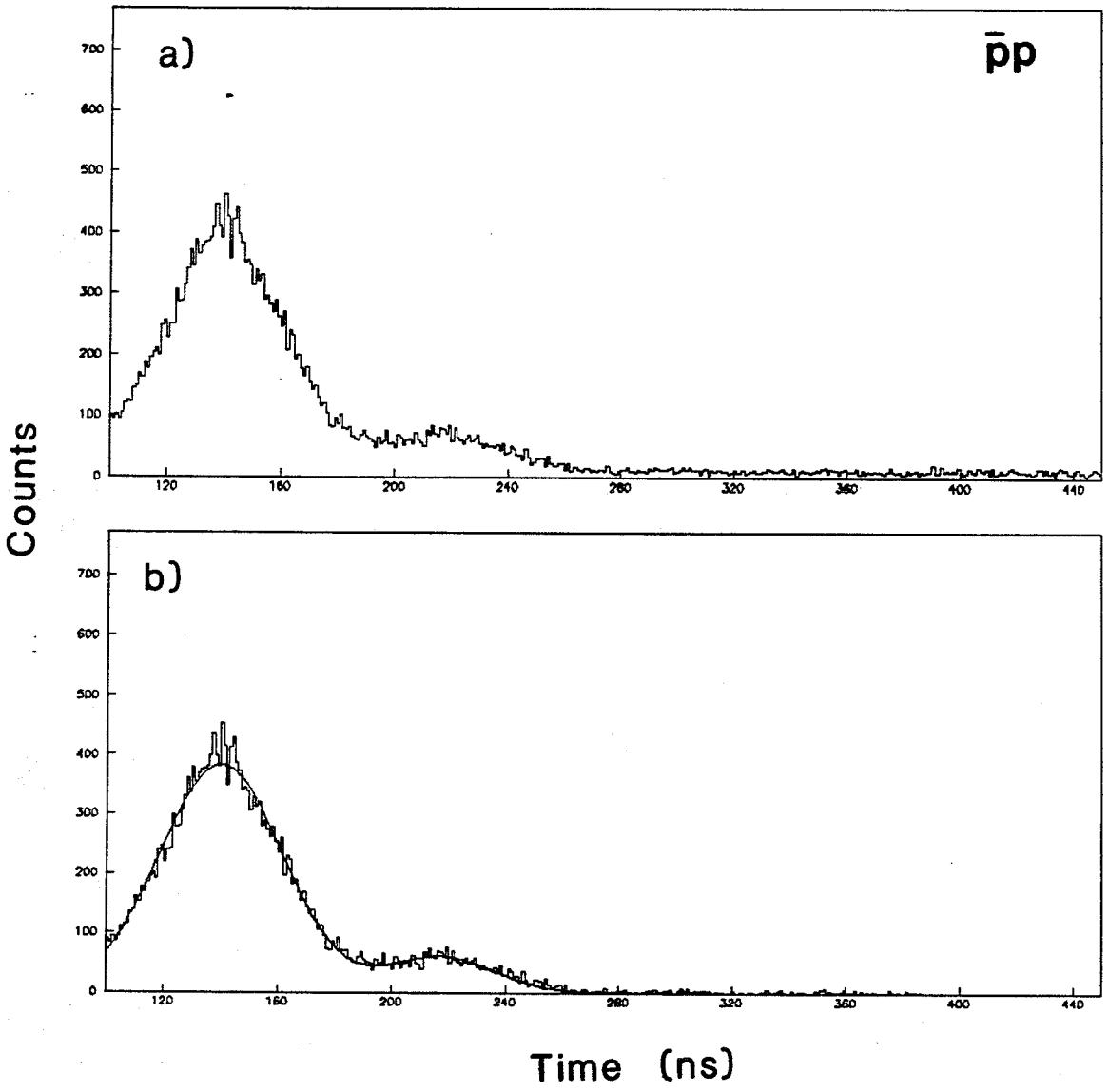

Figure 9.3 Example of analysis of lowest t bin, $0.0010 \leq |t| \leq 0.0012$ $(GeV/c)^2$ for Run Set Pb05.
a) Raw TDC spectrum of data in this interval.
b) TDC spectrum after subtraction of the constant background level with combined double Gaussian fit to background and data points.

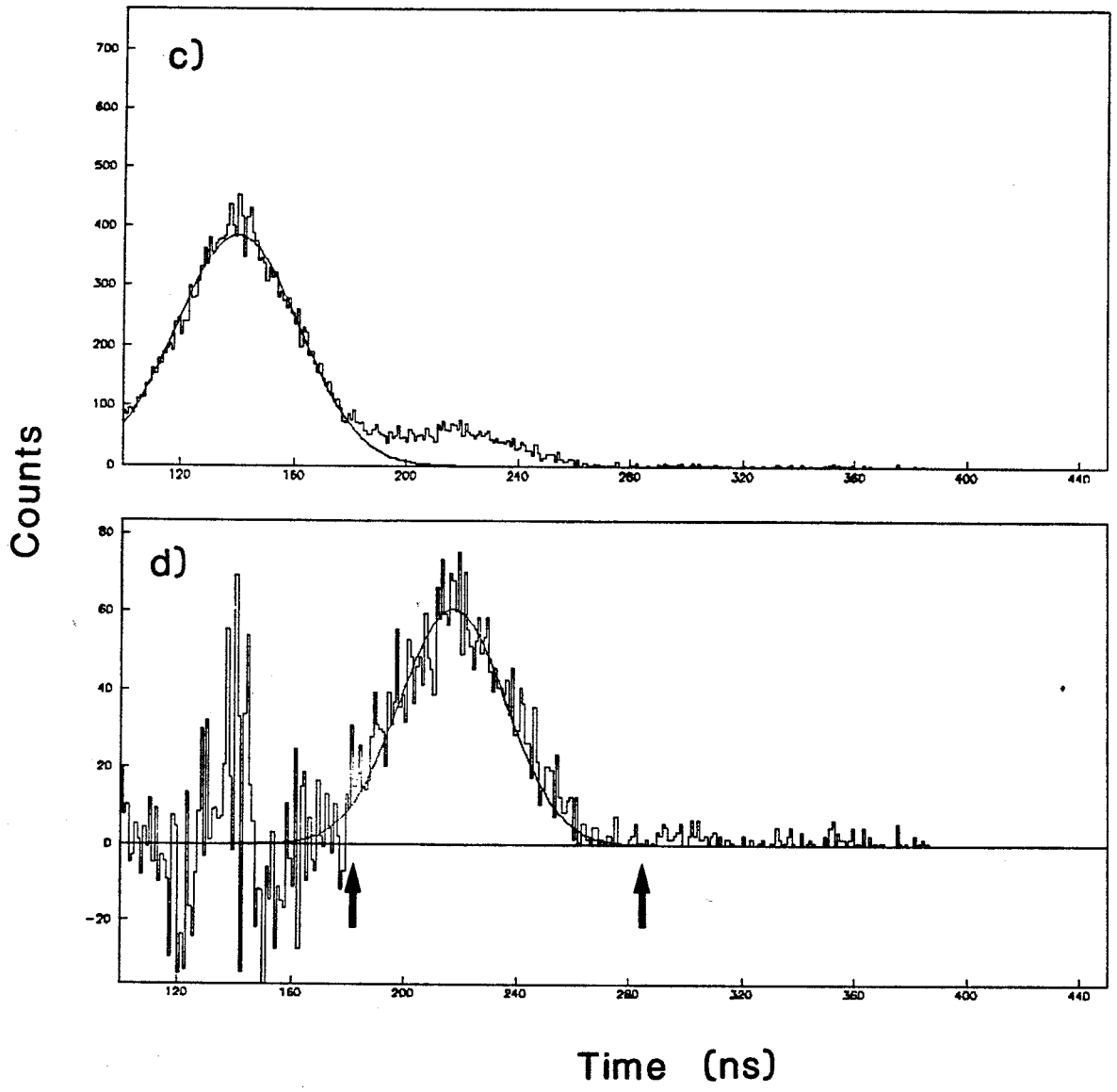

Figure 9.3 (continued)

c) Fit to background peak only

d) TDC spectrum after subtraction of the Gaussian fit to the background. Recoil count determined within the range marked by arrows then corrected for the "missing" portion of the Gaussian (4.8% in this case).

detector leaving only a small signal. Underneath all the data is a uniformly distributed background which at this low Δt interval consists mostly of electronic noise that exceeded the discriminator threshold. The constant background level was estimated by averaging over a t-o-f interval above the recoil peak and subtracted as in Figure 9.3b. The remaining peaks were then fit simultaneously with a curve consisting of the sum of two independent Gaussian distributions. The background peaks for these lowest few Δt intervals were well fit by Gaussians as in Figure 9.3c. The Gaussian function was next subtracted from the distribution and the recoil count determined by summing the remaining peak within a chosen interval, the lower limit of which was chosen approximately where the background and recoil rates were comparable. The count was corrected for this "missing" part of the peak using the Gaussian fit to the recoil peak. The very small inelastic contribution to these very low $|t|$ intervals was figured in the same way as for the higher intervals with usable position distributions as explained below. The error on the counting rates determined in this way was taken as the square root of the total counts in the recoil peak before the background Gaussian fits were subtracted.

9.2 Position Analysis

Position (x) across the PSD length (ℓ) is calculated from the raw PSD signals as

$$x = \frac{PSDX}{PSDT} \cdot \ell \text{ (mm)} \qquad (9.2)$$

subject to whatever corrections are necessary as previously described. Figure 9.4 shows a scatter plot of x versus |t| from the pp Run Set, P22. At this pivot angle, the position scale corresponds roughly to the scattering angles $0.8° \leq \theta \leq 4.0°$. The band of elastically scattered recoils, curved following the relation of Eq. 2.4, is clearly visible, as is the enhanced rate below the band due to inelastic recoils.

Once most of the background had been eliminated using the TDC cuts, the position spectra of the Δt intervals looked like Figure 9.5. The prominent elastic peaks overlap the tail of inelastics to the right at higher x (higher angle at fixed |t|). Events in the non-physical sector to the left of the elastic peak were assumed representative of a uniform background across the detector face. For the Pb21 Run Set pictured in Figure 9.5, the elastic peak was too close to the lower PSD edge in the first four Δt intervals for the small constant background to be estimated in this way. For these bins, with centers from 0.0024 to 0.0033 $(GeV/c)^2$, only the TDC information was used for the background estimate, as explained in the previous section.

The contribution to the elastic peak from SDD inelastic recoils was calculated using the same parametrization as for the stack analysis. Based on the luminosity of a Run Set, the angular distribution of inelastic recoils was calculated for each |t| bin and then was processed to follow the PSD position scale and PSD acceptance. A small adjustment for the measured variation in width of the PSD was also included. Agreement between the

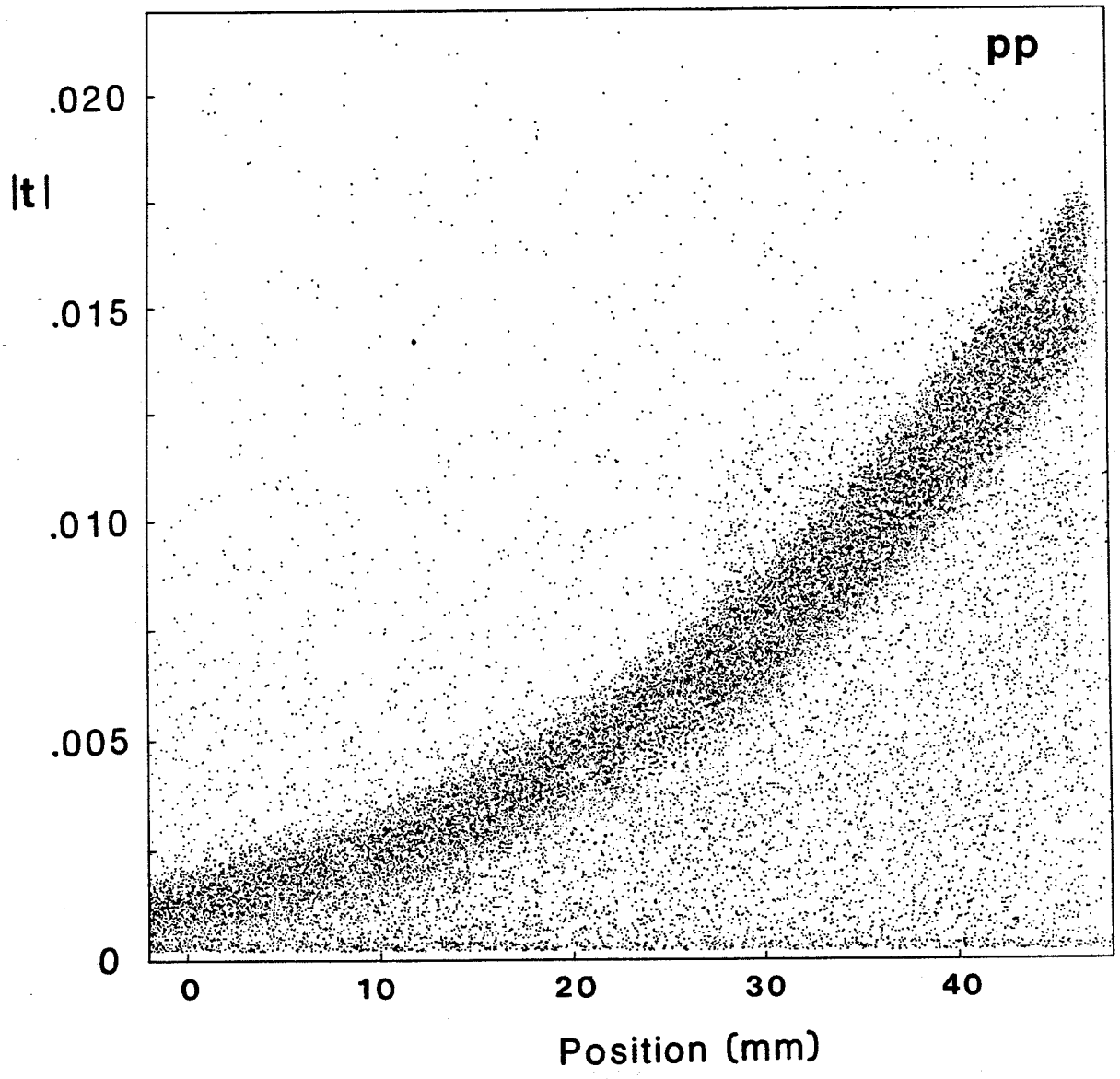

Figure 9.4 Position along the PSD versus momentum transfer $(GeV/c)^2$ of events in P22 that pass the TDC cuts.

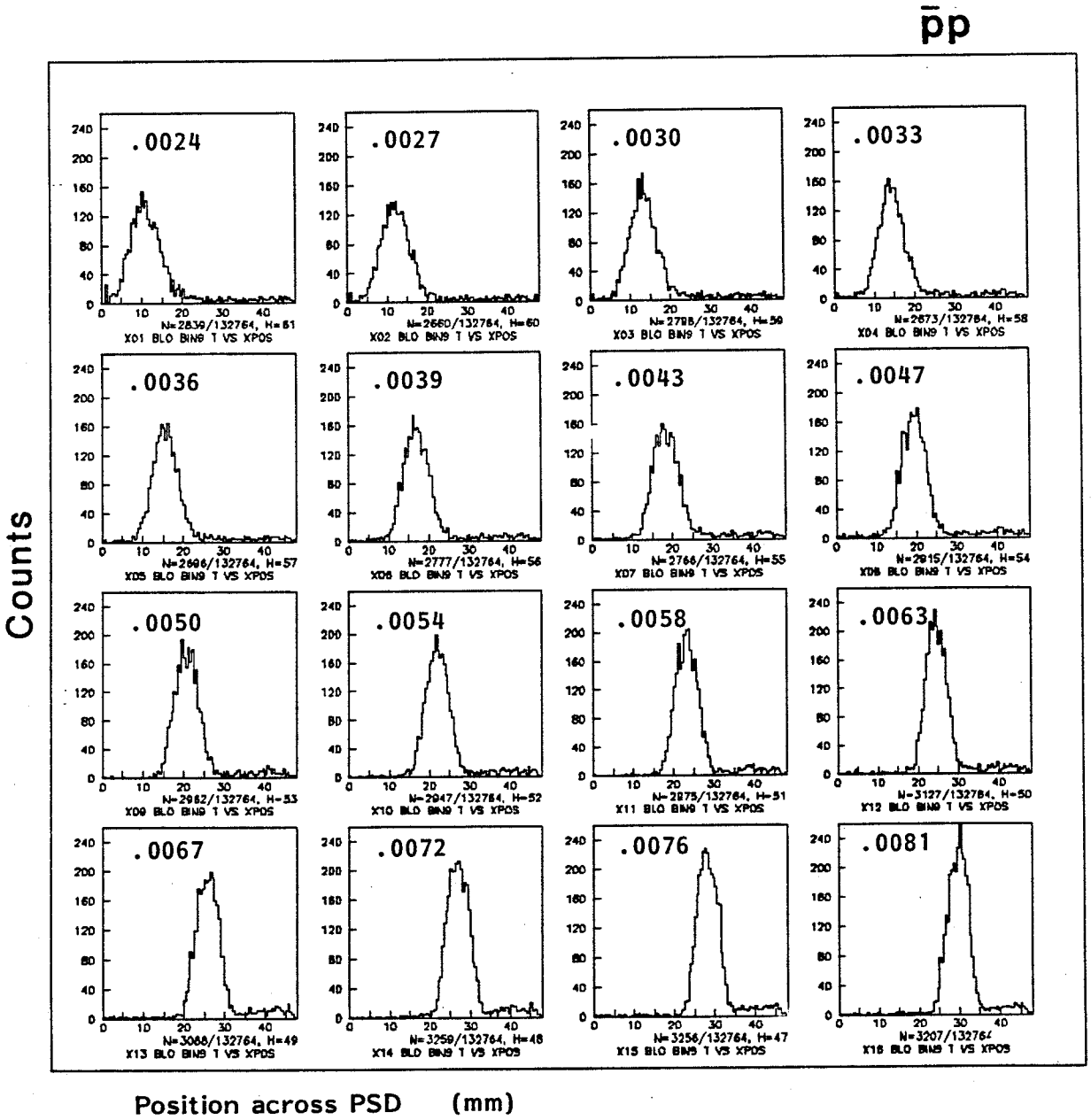

Figure 9.5 Position spectra after the TDC cuts from successive Δt intervals of Pb21. The |t| value of the center of the bin is shown in $(GeV/c)^2$.

parametrization and the presumed inelastic recoil distribution was good and the small part of the inelastic distribution that extended beneath the elastic peak was subtracted as in Figure 9.6. The subtraction generally amounted to less than 1% of the rate within the limits of the peak. Due to the simplicity of the PSD geometry compared to the stacks and the narrowness of the Δt intervals, a Monte Carlo simulation was not necessary. Again the same parametrization was assumed to hold for pp and $\bar{p}p$.

Because the accuracy of the inelastic recoil subtraction relied upon the position distribution of the data, the scale was verified by plotting in addition $\Delta M^2 = M_x^2 - m^2$ (from Eq. 2.3) for each Δt interval. If the distributions, as was usual, did not center on zero overall, the position scale was shifted to compensate. This shift was necessary because the raw PSDX signal originating from the detector was found to have a small offset with respect to the x = 0 mm point of the PSD (noted also with the pulser) that varied somewhat from run to run. A small amount subtracted from the PSDX signal, representing the average of the offset over the entire Run Set, generally brought the ΔM^2 distributions to be centered close to zero.

This small offset correction was also relevant to the correction for the loss of elastics at the PSD edge. The rates for the t bins near the extreme angle limits for each Run Set were corrected for any amount that a Gaussian fit extended beyond the detector edge. If this correction exceeded 5% for a particular interval, the interval was not included among the points used for the final fits. Additional losses due to nuclear collisions were

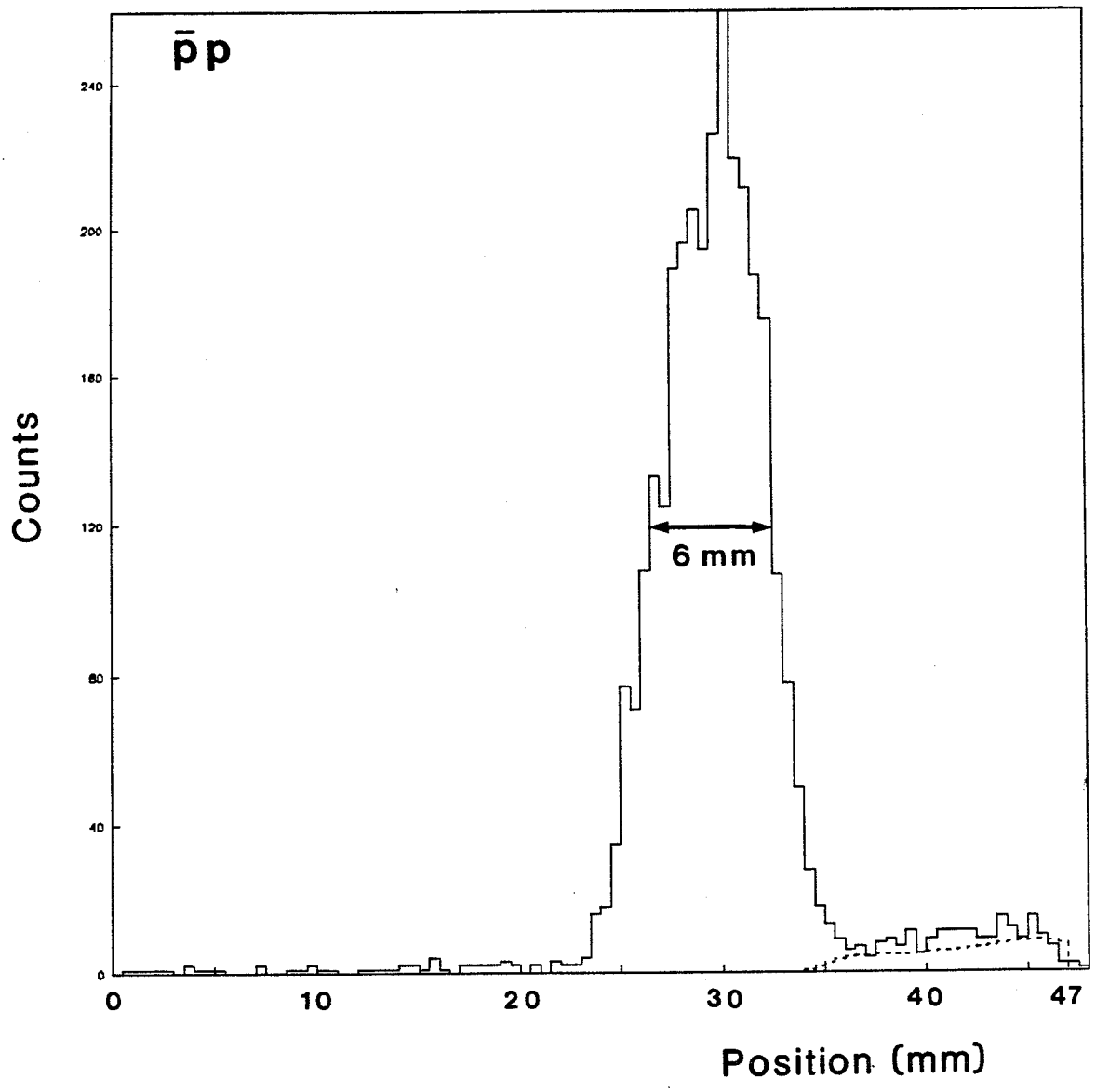

Figure 9.6 Position spectrum of events within the time cut for the interval $0.0078 \leq |t| \leq 0.0084$ $(GeV/c)^2$. The peak FWHM of 6 mm reflects the jet width. The average level of counts/mm into the region 0-20 mm determined the constant background subtraction. The dashed curve between 34-47 mm (the PSD upper edge) is the distribution of inelastic recoils as calculated by the parametrization.

insignificant since the PSD was so thin. The errors on the elastic count values were taken as the square root of the number of events in the elastic peaks, corrected for losses, before the constant background or inelastic subtractions.

CHAPTER 10 Results and Conclusions

10.1 Fitting for ρ and b

After the corrected elastic rates were determined, the un-normalized differential cross sections were calculated for the stack points using Eq. 2.19 and for the PSD t bins using Eq. 2.20. Employing given values for σ_{tot}, independent fits for pp and $\bar{p}p$ were made to the combined PSD and stack points from which values of ρ and b were extracted.

10.1.1 χ^2 Minimization

The fitting method involved the minimization of the standard χ^2 function, defined as

$$\chi^2 = \sum_{i=1}^{N_P} \left\{ \frac{[(d\sigma/dt)_i - \xi_P \cdot f(\sigma_{tot},\rho,b)]^2}{\delta^2(d\sigma/dt)_i} \right\} + \sum_{i=1}^{N_S} \left\{ \frac{[(d\sigma/dt)_i - \xi_S \cdot f(\sigma_{tot},\rho,b)]^2}{\delta^2(d\sigma/dt)_i} \right\} \qquad (10.1)$$

where $(d\sigma/dt)_i$ is the ith experimentally measured differential cross section point and $\delta(d\sigma/dt)_i$ is the error in that value. The functional parametrization of the differential cross section, $f(\sigma_{tot},\rho,b)$ is given by Eq. 2.16 and the overall normalization factors are ξ_P for the PSD and ξ_S for

the stack points. The total number of stack points included in the fits was $N_S = 7$ for the pp measurement and $N_S = 10$ for $\bar{p}p$. The PSD points were left independent by Run Set, so $N_P = 88$ for pp and $N_P = 256$ for $\bar{p}p$.

10.1.2 Inter-normalization of PSD Run Sets

The luminosity measured by the fixed detectors provided the initial normalization among the PSD Run Sets covering different t ranges. But because of the much greater rate of elastic recoils accepted by the PSD than accepted by the luminosity monitors, the inter-normalization was fine-tuned using the differential cross sections within the overlapping t regions as calculated for each Run Set. Bin by bin, the individual overlapping values were compared to the average of the four pp or eleven $\bar{p}p$ Run Sets and an overall adjustment was made to the luminosity associated with each Run Set. The differential cross sections were then re-calculated based on the inter-normalization. This adjustment was 1.8% at its greatest among the pp Run Sets and no more than 3.8% for $\bar{p}p$.

10.1.3 PSD Bin Correction and Fluctuations

Because the differential cross section changes so rapidly in the Coulomb region, the measured rate was not associated for fitting to the center value of a Δt interval, but with a value weighted by the distribution. This "binning correction" was performed by numerical integration of a suitable form of the differential cross section over each

interval and affected only t values associated with the very low bins, shifting them slightly lower from center (<0.4%).

The effect of detector energy resolution was tested by convoluting Eq. 2.16 with a Gaussian distribution. If the theoretical form is $F_{th}(t) = d\sigma/dt$, then a finite detector resolution would cause the cross section to be measured as

$$F_{exp} = \int_{t_1}^{t_2} \frac{1}{r(t')\sqrt{2\pi}} \; e^{\frac{-(t-t')^2}{2r^2}} \; F_{th}(t') \; dt' \qquad (10.2)$$

where t_1 and t_2 span the range of the PSD and r(t) is some unknown resolution function for the recorded energy of the recoil proton. Such binning fluctuations have the effect of making a rapidly falling cross section appear even steeper. A numerical analysis demonstrated that even with r = 50 KeV (twice the typical measured alpha particle resolution) the magnitude of the effect even at very low |t| was only a fraction of the statistical error. Since there was no evidence for poorer resolution for protons measured in the experiment, no compensation for binning fluctuations was included in the fit.

10.1.4 Vacuum Polarization

A second-order correction to the electromagnetic fine structure constant for vacuum polarization may be included in the differential cross section parametrization Eq. 2.16 and is given by [10.3]

$$\alpha(t) = \alpha\left(1 + \frac{\alpha}{3\pi}\cdot\ln\left(\frac{|t|}{4m_e^2}\right)\right) \qquad (10.3)$$

where $\alpha = \frac{1}{137}$ and m_e is the mass of the electron. The small change in the values obtained by the fit for the ρ parameters induced by the vacuum polarization correction are given below, but since apparently this correction has not been applied to earlier data, the final tabulated results are given without it.

10.1.5 Fit Results and Error Discussion

The values used for the total cross sections as input to the fits were $\sigma_{tot}(pp) = 39.46 \pm 0.04$ mb and $\sigma_{tot}(\bar{p}p) = 41.40 \pm 0.10$ mb obtained from a parametrization of the form given by Eq. 3.17 [10.1]. The experimental differential cross sections, with the normalization determined by the fits, are presented for Δt intervals of the PSD in Table 10.1. Values are given for the luminosity-weighted averages for the pp and $\bar{p}p$ Run Sets. The $d\sigma/dt$ values of the individual stack measurements are listed in Table 10.2 for pp and Table 10.3 for $\bar{p}p$. In Tables 10.1 through 10.3, the differential cross sections as determined by the fits are also shown. Finally, the fit parameters and their statistical correlation errors may be found in Table 10.4, along with the χ^2 per degree of freedom (d.o.f.) obtained by the fits.

Table 10.1 Differential cross section measurements for PSD Δt intervals averaged over all the Run Sets and corresponding values calculated from the fit function.

$\|t\|$	$d\sigma/dt$ (mb/GeV^2)			
(GeV/c)^2	pp PSD data	pp Fit	$\bar{p}p$ PSD data	$\bar{p}p$ Fit
0.00108	292.9 ± 3.0	291.6	313.0 ± 3.5	314.8
0.00126	234.9 ± 2.5	231.7	252.4 ± 2.6	252.6
0.00146	190.4 ± 2.2	191.3	210.5 ± 2.1	210.4
0.00168	163.1 ± 1.9	163.1	183.0 ± 1.8	180.7
0.00191	142.5 ± 1.4	142.9	160.9 ± 1.6	159.3
0.00216	127.8 ± 1.2	128.2	143.9 ± 1.2	143.5
0.00242	117.6 ± 1.1	117.2	132.0 ± 1.1	131.7
0.00269	108.2 ± 1.0	108.9	121.3 ± 1.0	122.6
0.00298	103.0 ± 1.0	102.4	116.0 ± 0.9	115.5
0.00329	96.7 ± 0.9	97.4	109.6 ± 0.9	109.9
0.00361	93.7 ± 0.9	93.4	105.5 ± 0.8	105.4
0.00394	89.8 ± 0.9	90.2	101.1 ± 0.8	101.7
0.00429	87.7 ± 0.8	87.5	99.4 ± 0.8	98.7
0.00466	84.5 ± 0.8	85.3	96.4 ± 0.8	96.1
0.00504	84.4 ± 0.8	83.4	94.0 ± 0.7	93.9
0.00543	82.0 ± 0.8	81.8	92.1 ± 0.7	92.0
0.00584	81.1 ± 0.7	80.4	90.2 ± 0.7	90.3
0.00626	78.7 ± 0.8	79.2	89.8 ± 0.8	88.9
0.00670	78.4 ± 0.8	78.1	87.8 ± 0.8	87.5
0.00716	78.2 ± 0.7	77.2	86.5 ± 0.7	86.3
0.00763	76.6 ± 0.8	76.3	85.3 ± 0.7	85.2
0.00811	75.7 ± 0.8	75.4	83.7 ± 0.8	84.2
0.00861	74.3 ± 0.8	74.7	82.9 ± 0.8	83.2
0.00912	74.7 ± 0.8	73.9	82.5 ± 0.8	82.3
0.00965	72.6 ± 1.0	73.2	82.0 ± 0.8	81.4
0.01019	72.2 ± 1.0	72.6	81.2 ± 0.8	80.6
0.01075	70.9 ± 1.0	71.9	79.5 ± 0.9	79.8
0.01132	70.2 ± 1 0	71.3	79.1 ± 0.9	79.0
0.01191	70.4 ± 0.9	70.7	78.9 ± 0.9	78.2
0.01251	70.7 ± 0.9	70.1	76.4 ± 0.8	77.4
0.01313	68.5 ± 0.9	69.5	75.8 ± 0.8	76.7
0.01376			75.8 ± 0.8	75.9

Table 10.2 Stack differential cross sections (pp).

$\|t\|$ $(GeV/c)^2$	$d\sigma/dt$ (mb/GeV^2)	Fit
0.03440	53.7 ± 0.5	53.9
0.03510	53.0 ± 0.3	53.4
0.03880	52.1 ± 0.4	51.2
0.04570	47.2 ± 0.4	47.3
0.04570	47.7 ± 0.4	47.3
0.04960	46.1 ± 0.5	45.3
0.05400	42.2 ± 0.5	43.1

Table 10.3 Stack differential cross sections ($\bar{p}p$).

$\|t\|$ $(GeV/c)^2$	$d\sigma/dt$ (mb/GeV^2)	Fit
0.03700	55.8 ± 0.6	56.0
0.03720	55.8 ± 0.5	55.8
0.03720	55.5 ± 0.6	55.8
0.04150	53.2 ± 0.7	52.9
0.04170	52.9 ± 0.6	52.8
0.04960	47.6 ± 0.4	47.8
0.04970	49.3 ± 0.7	47.7
0.04970	47.9 ± 0.4	47.7
0.05230	45.6 ± 0.7	46.2
0.05460	44.6 ± 0.6	44.9

Table 10.4 Results of the fits to combined PSD and stack values.

	b (GeV^{-2})	ρ	$\xi_p(/10^{-3})$	ξ_S	d.o.f	χ^2/d.o.f
pp	11.4 ± 0.5	0.009 ± 0.010	6.53 ± 0.06	0.825 ± 0.016	91	1.45
$\bar{p}p$	12.3 ± 0.5	0.048 ± 0.011	6.04 ± 0.06	0.832 ± 0.021	262	1.02

If the vacuum polarization correction is included in the fit, no changes occur in the slopes while the following results are obtained for the real parts: $\rho(pp) = 0.002 \pm 0.010$ and $\rho(\bar{p}p) = 0.041 \pm 0.011$ with little change in the χ^2.

The PSD data were also fit for the ratio ρ independently of the stack measurements by assuming a value for the nuclear slope from a parametrization similar to the one discussed in Section 3.3 [10.1]. The inputs and the resulting values of ρ are summarized in Table 10.5 [10.2]. The effect on ρ due to the uncertainty in the σ_{tot} and b parametrizations can be gauged from the values in the last columns of the table.

Table 10.5 Parameters for the fit to PSD data only.

	Input		Results			
	σ_{tot}(mb)	b (GeV^{-2})	ρ	χ^2/dof	$\Delta\rho/\Delta\sigma_{tot}$	$\Delta\rho/\Delta$b
pp	39.46±0.04	11.76±0.04	0.014±0.007	1.36	0.034 mb^{-1}	0.013 GeV^2
$\bar{p}p$	41.40±0.10	12.51±0.08	0.045±0.007	1.02	0.033 mb^{-1}	0.016 GeV^2

Fits were also made in which the total cross sections were left as free parameters. The results demonstrated consistency with the values obtained from the parametrization that were normally used as input to the fits. For the pp data, the fit leaving the cross section as a free parameter found $\sigma_{tot} = 39.5 \pm 0.4$ with $\rho = 0.008 \pm 0.016$ (χ^2/d.o.f. = 1.46), while for $\bar{p}p$ the fit found $\sigma_{tot} = 41.8 \pm 0.4$ with $\rho = 0.061 \pm 0.017$ (χ^2/d.o.f. = 1.01). There was no change in the slope values from what is presented in Table 10.4.

Table 10.6 summarizes sources of systematic error. The uncertainty in the total cross section values is reflected in the column headed as $\Delta\sigma_{tot}$, where, as is to be expected, it is seen that the slope, which on a log scale should be insensitive to the absolute normalization, is indeed little affected by the uncertainty of σ_{tot}. The alpha source width in the PSD of 25-30 KeV suggests a t-scale uncertainty on the order of 0.5%, contributing ± 0.006 to the ρ error.

Table 10.6 Error contributions to full fit of PSD and stack points.

Parameter	Statistical	$\Delta\sigma_{tot}$	t-scale
b(pp)	± 0.46	± 0.01	± 0.07
b($\bar{p}p$)	± 0.53	± 0.02	± 0.07
ρ(pp)	± 0.010	± 0.002	± 0.006
ρ($\bar{p}p$)	± 0.011	± 0.003	± 0.006

It should also be noted that the theoretical uncertainty in the calculation of the Coulomb-hadronic phase induces a systematic error in the determination of the ρ values. West and Yennie [2.2] set an uncertainty of $|\Delta\alpha\phi| \leq 0.015$ on their calculation but Amos et al. [3.14] have found that this adds negligible error when allowed to vary within the West and Yennie limits in their simultaneous fits for $\rho(pp)$ and $\rho(\bar{p}p)$ at the ISR.

10.1.6 Spin Effects

The effect of spin on the measurement of ρ was considered by N. Buttimore with regard to the UA6 measurement. Following Ref. 10.4, he found the spin corrections to ρ to yield [10.5]

$$\rho' = \rho \pm 1.164 \ |t|_{int} \tag{10.3}$$

where ρ is the conventional spin-averaged value and $|t|_{int}$ is the value at which the Coulomb and hadronic terms of the differential cross sections are of comparable magnitude (see Eq. 2.17). For the UA6 energy of $\sqrt{s} = 24.3$ GeV, this correction is $\rho' = \rho \pm 0.002$ in which the upper sign is for pp, the lower sign for $\bar{p}p$.

10.1.7 Normalization and Detector Acceptance

As defined for the fits, the normalization parameters ξ_P and ξ_S give an approximate determination of the absolute detector acceptance. In the case of the stacks, where the relative geometrical acceptance had already been included in the un-normalized differential cross sections, the agreement

between $\xi_S(pp)$ and $\xi_S(\bar{p}p)$ in Table 10.4 is noted. The normalization parameter ξ_P is related to the phi acceptance of the PSD, given as $\Delta\phi$ in Eq. 2.20. An approximate measure of this acceptance was made during running with the detector array arm rotated 90° to a vertical position (see Section 5.2.2). The pivot angle for this running was set so that elastic recoils would come to a stop within the PSD as well as within the front (DE) detectors of the stacks. With the assumption that the DE detectors had an area of 100 mm^2 (the nominal value) the phi acceptance of the PSD was determined to be $\Delta\phi \sim 6.5 \pm 0.1$ mrad by comparing the recoil rate from pp collisions accepted by the PSD to the rate accepted by the DE detectors. This value is in good agreement with the interpretation of $\xi_P(pp)$ as 6.53 ± 0.06 mrad in Table 10.4.

10.2 Plots

Figure 10.1a shows the PSD differential cross section measurements for all four pp Run Sets with the full fit to the PSD and stack points superimposed. The overlapping multiple measurements for particular t bins are actually associated with the same |t| values but have been displaced as necessary for clarity. Figure 10.1b is the same for the eleven $\bar{p}p$ Run Sets.

Values for the luminosity-weighted PSD measurements along with the stack points are shown in Figures 10.2a and b. The quantity $R = (d\sigma/dt)/(d\sigma/dt)_{\rho=0} - 1$ is plotted against momentum transfer-squared in Figure 10.3. The constructive interference in $\bar{p}p$ scattering at this energy

is evident while for pp scattering the destructive interference is barely noticeable since ρ(pp), although positive, is quite close to zero. The plot also shows how the data extend below the |t| value of maximum interference.

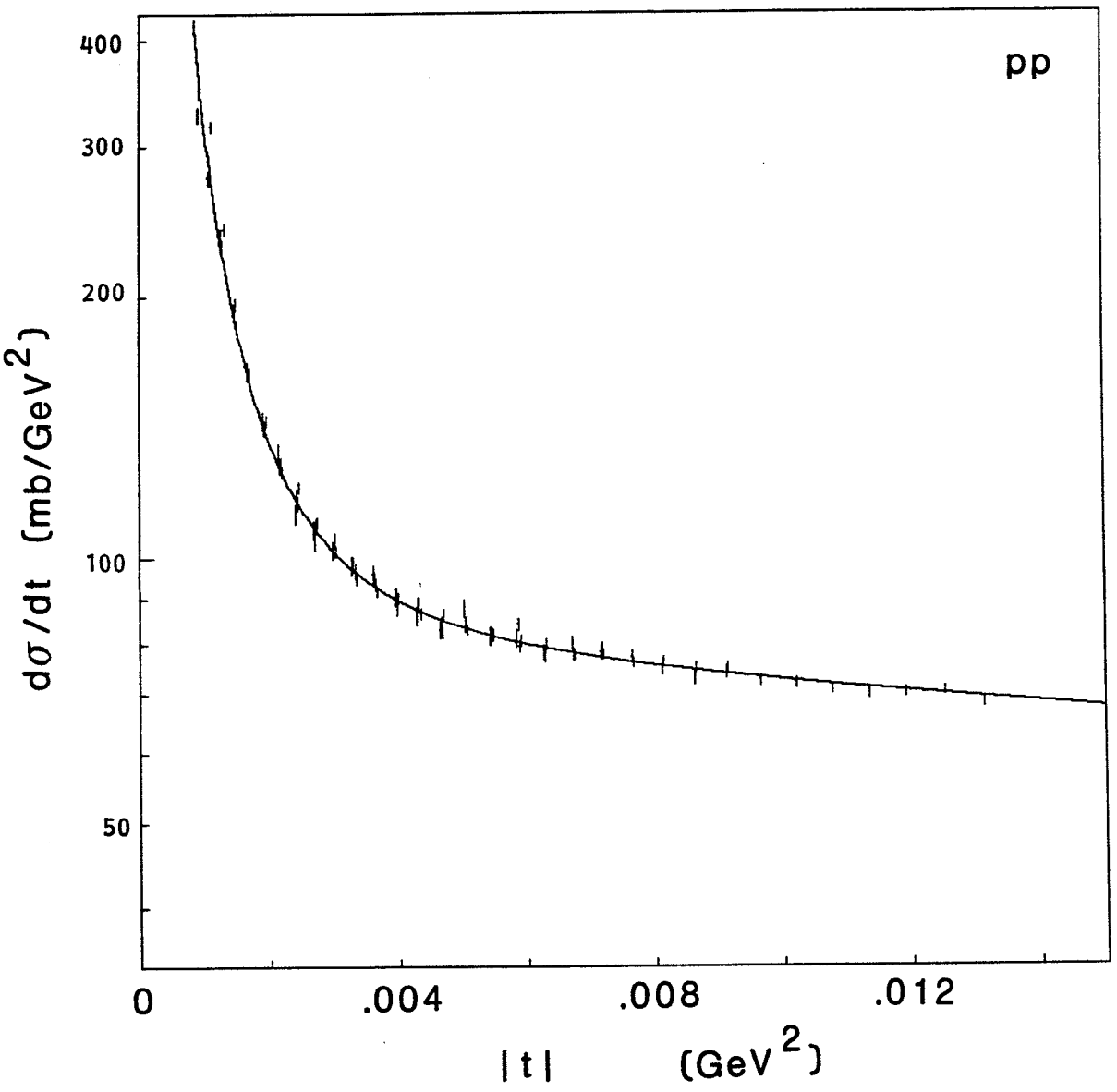

Figure 10.1 a) Differential cross section measurements from all pp Run Sets (PSD only) with the best fit shown. Some points have been slightly displaced for better visibility.

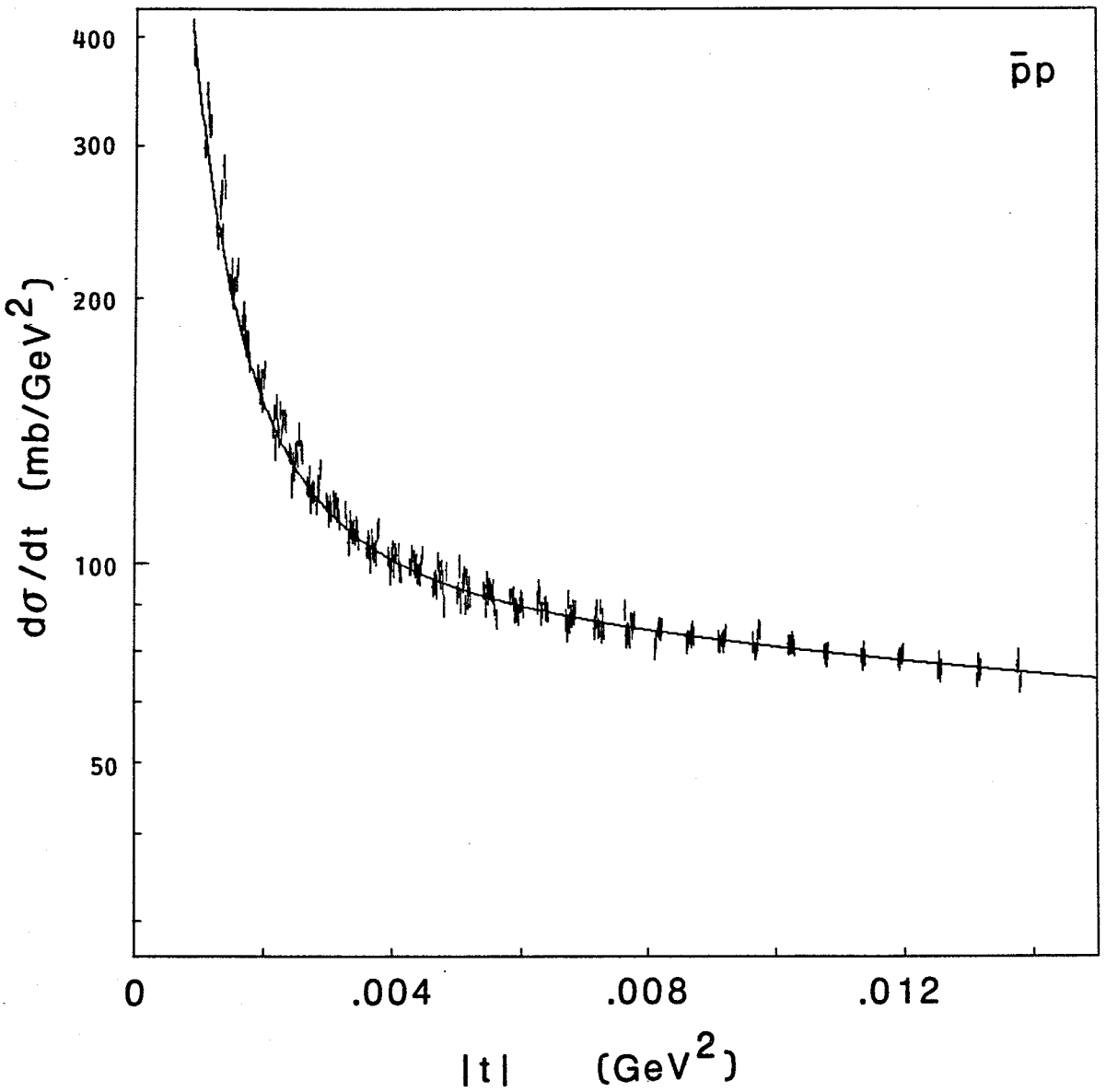

Figure 10.1 b) Differential cross section measurements from all $\bar{p}p$ Run Sets (PSD only). Points have been displaced for visibility.

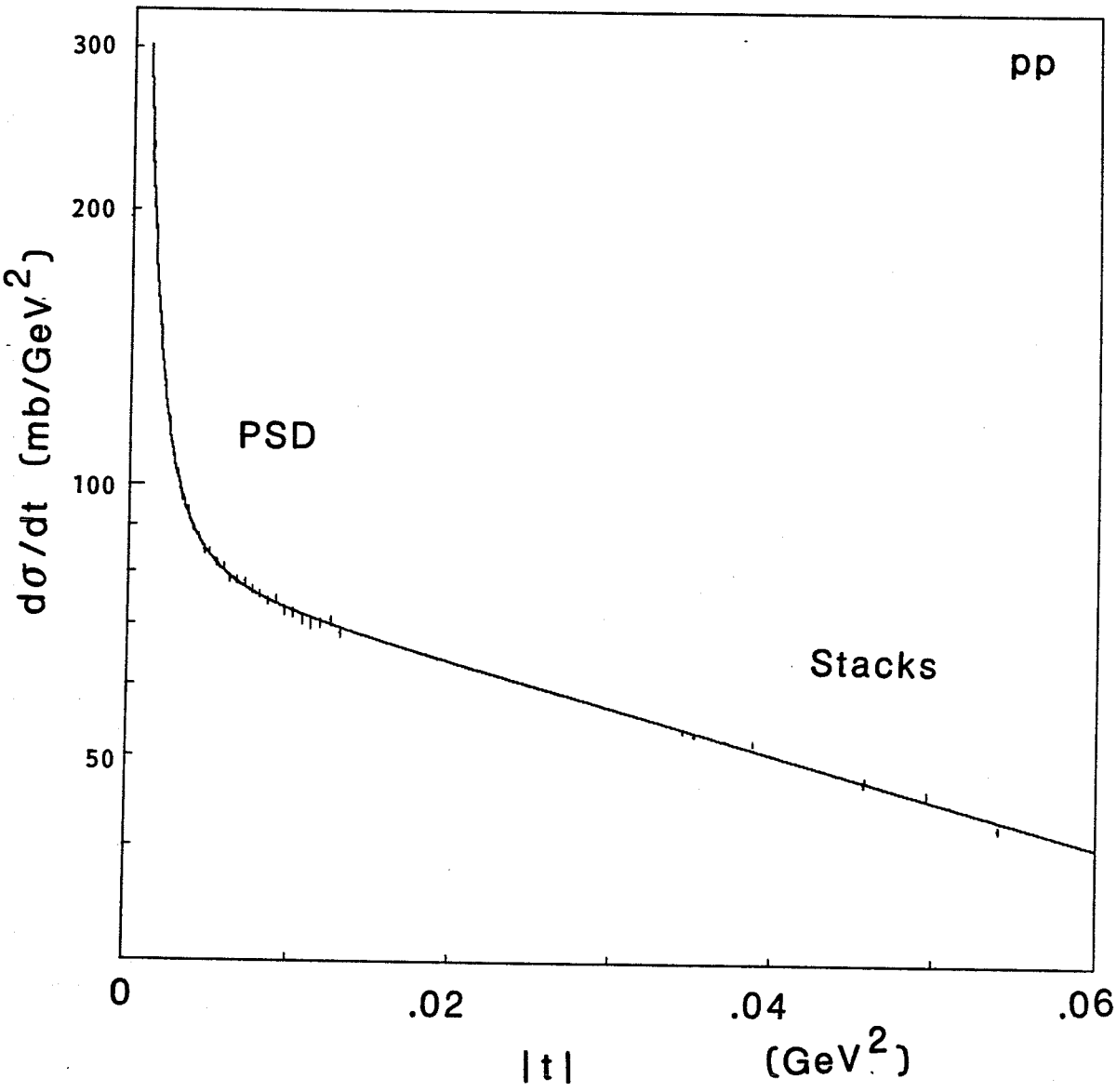

Figure 10.2 a) pp differential cross section with fit superimposed. The PSD points represent the average of the Run Sets.

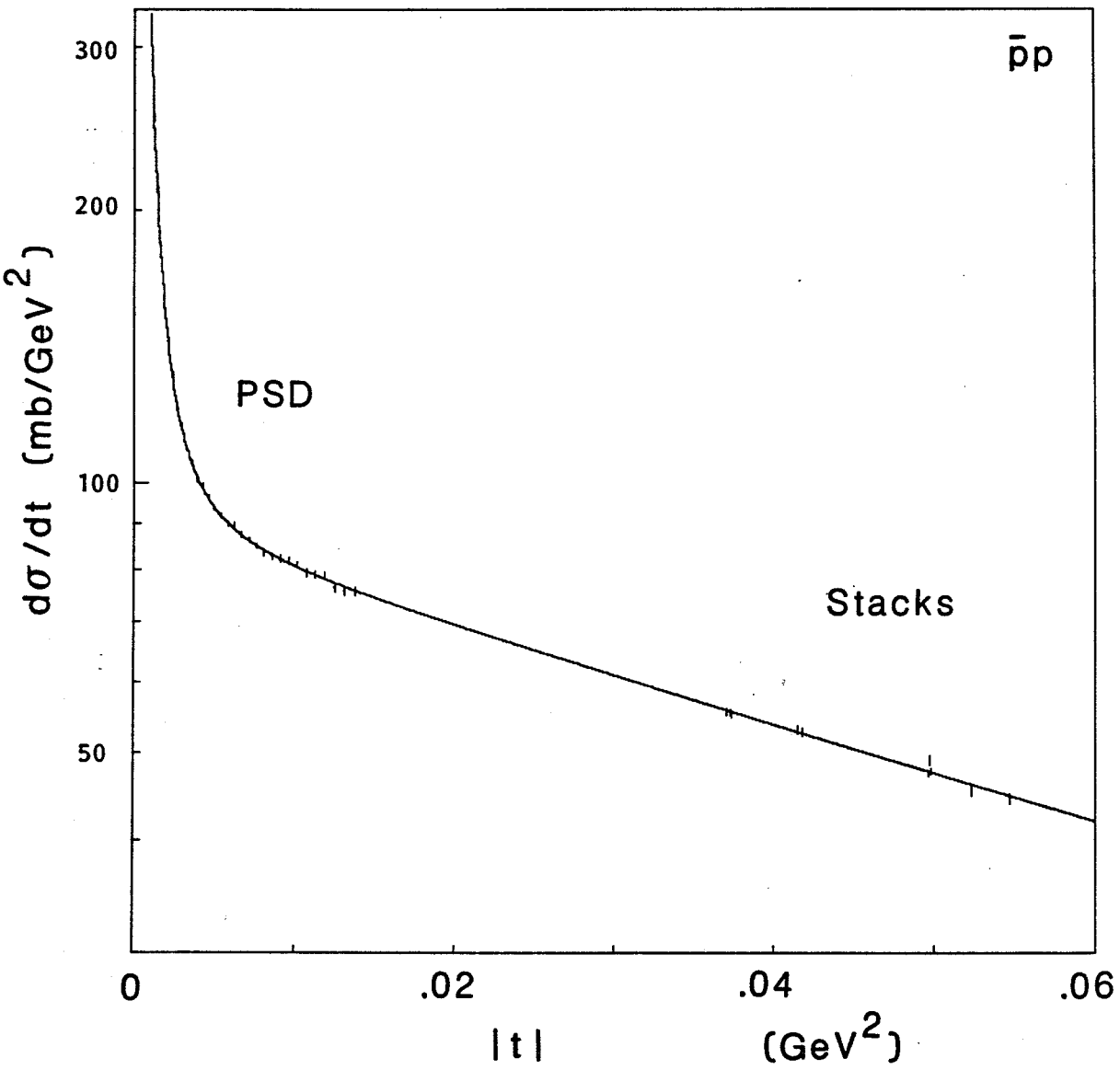

Figure 10.2 b) $\bar{p}p$ differential cross section.

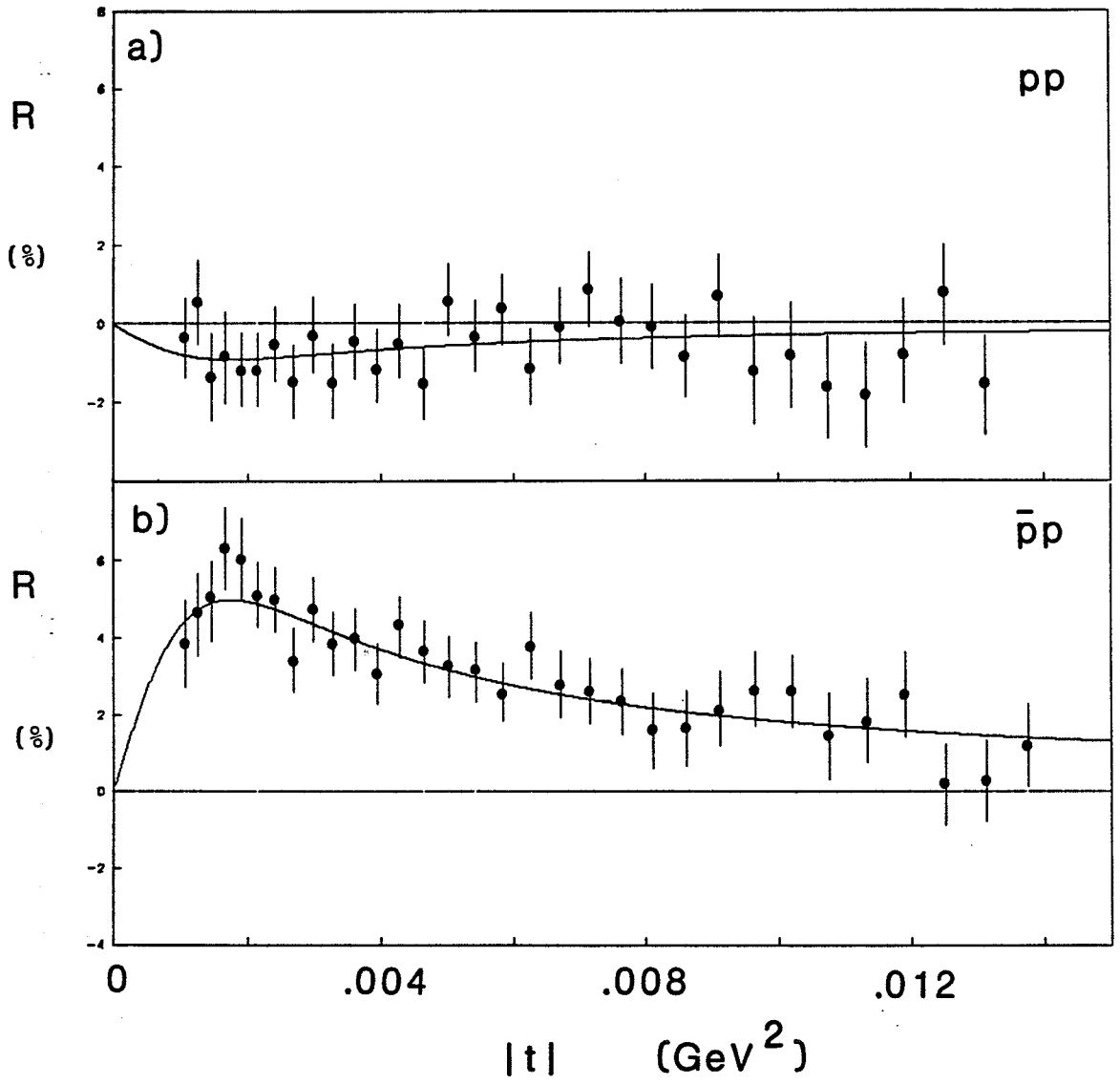

Figure 10.3 Proportion of real amplitude in the differential cross sections: the quantity $R = (d\sigma/dt)/(d\sigma/dt)_{\rho=0}$-1 presented as a percentage a) for pp, b) for $\bar{p}p$.

10.3 Conclusions

Table 10.7 summarizes the results of the fits to the complete sets of differential cross section measurements using parametrized values of the total cross sections as input to the fits. No corrections for vacuum polarization nor spin effects have been included.

Table 10.7 Summary of final results for the differential cross section fits

$b(pp)$ (GeV^{-2})	11.4 ± 0.5 (stat.) ± 0.1 (sys.)
$b(\bar{p}p)$ (GeV^{-2})	12.3 ± 0.5 (stat.) ± 0.1 (sys.)
Δb (GeV^{-2})	0.96 ± 0.70
$\rho(pp)$	0.009 ± 0.010 (stat.) ± 0.006 (sys.)
$\rho(\bar{p}p)$	0.048 ± 0.011 (stat.) ± 0.006 (sys.)
$\Delta\rho$	0.039 ± 0.014

The UA6 values for the ratio ρ are shown plotted with measurements at other energies in Figure 10.4. That the $\bar{p}p$ total cross section is rising through the UA6 energy is reflected in the positive value for $\rho(\bar{p}p)$. The total cross section for proton-proton scattering, however, is just beginning its rise with energy at $\sqrt{s} = 24.3$ GeV which correlates with the value found to be close to zero. The difference between $\rho(\bar{p}p)$ and $\rho(pp)$ is found to be $\Delta\rho = 0.039 \pm 0.014$, much less than the differences at lower energies. That this trend continues through ISR energies is consistent with the hypothesis that $\Delta\rho$ will go to zero asymptotically. The results for $b(pp)$ and $b(\bar{p}p)$ are compared to other measurements in Figure 10.5.

10.4 Discussion

This section concludes with an example of how theoretical considerations may be examined using these results. A. Martin has pointed out [10.6] that by taking $F_- = \frac{1}{2}(F(pp) - F(\bar{p}p))$ at $t = 0$ and defining the quantity $\rho_- = \text{Re } F_-/\text{Im } F_-$, one can demonstrate from the optical theorem the following identity:

$$\rho_- = \Delta\rho \frac{\sigma(\bar{p}p)}{\Delta\sigma} + \rho(pp) \ . \tag{10.4}$$

Additionally, it is possible to prove using dispersion relations that if $\Delta\sigma \sim E^{-\alpha}$ then $\rho_- = \cot(\pi\alpha/2)$. If one uses the value $\alpha = 0.56 \pm 0.01$ which Amos et al. found in applying the Amaldi-type parametrization of Eq. 3.15, then $\rho_- = 0.827 \pm 0.026$. Using $\Delta\sigma = 1.94$ mb, the UA6 measurements inserted into Eq. 10.4 give $\rho_- = 0.84 \pm 0.34$, consistent with the assumption that $\Delta\sigma \to 0$ aymptotically as $E^{-\alpha}$. On the other hand, the fit assuming a significant odd-under-crossing amplitude of Ref. 3.7 predicts for the UA6 energy $\rho_{odd}(pp) = -0.007$ and $\rho_{odd}(\bar{p}p) = 0.054$ yielding $\Delta\rho = 0.061$. This demonstrates a difference between the UA6 result and the odderon prediction of 0.022 ± 0.014 which, while not suggestive, does not rule out the possibility of an odd-under-crossing amplitude dominating at high energies. A definitive answer awaits precise comparisons of pp and $\bar{p}p$ at higher energies.

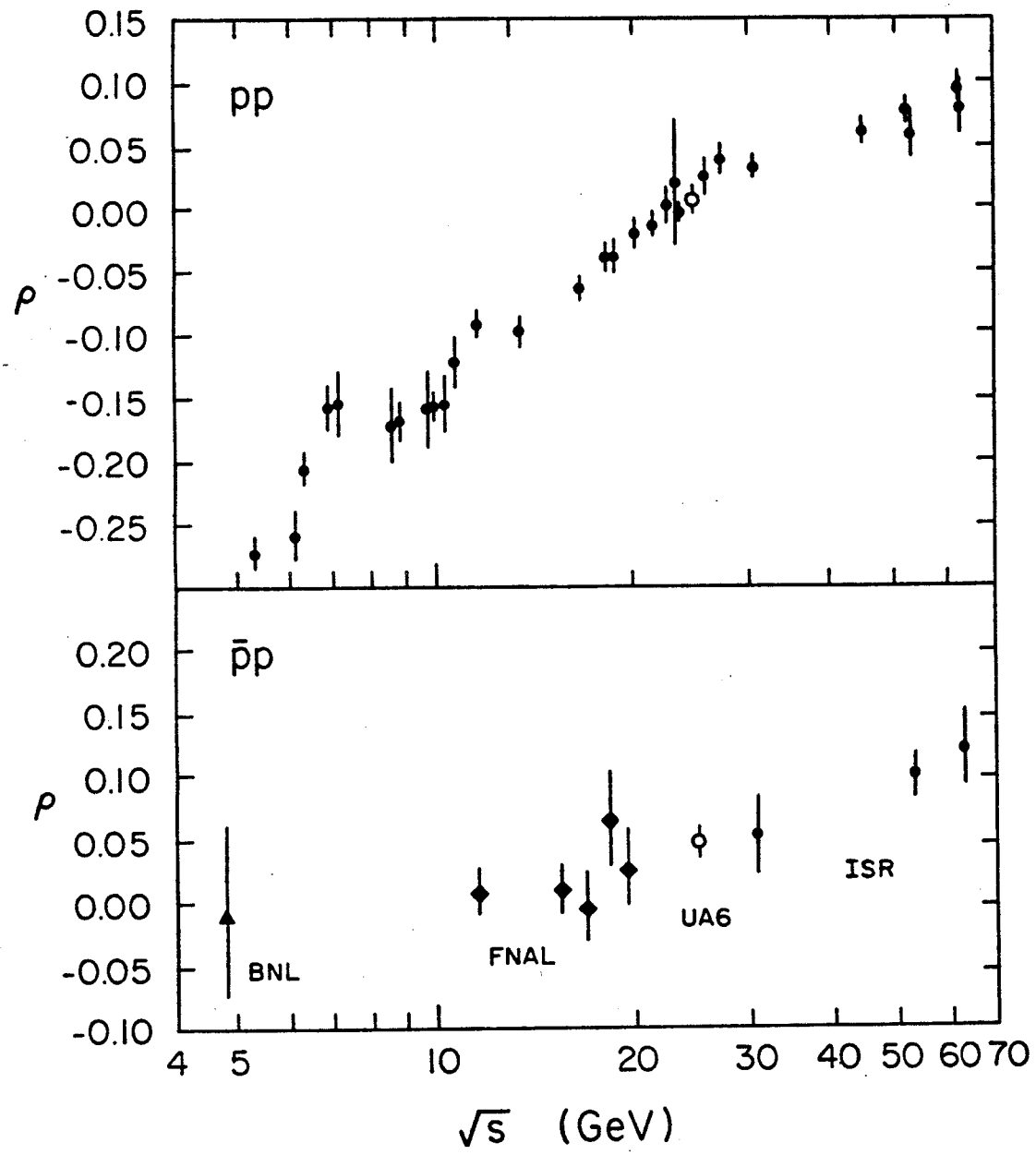

Figure 10.4 The UA6 values of ρ plotted with measurements at other energies. The error bars on the UA6 points represent the total error listed in Table 10.6. pp plot adapted from Ref 3.11; $\bar{p}p$ data from Refs. 1.7, 3.14 and 10.7. (Not shown is the UA4 result, Ref. 1.9, of $\rho(\bar{p}p) = 0.24 \pm 0.04$ at $\sqrt{s} = 546$ GeV.)

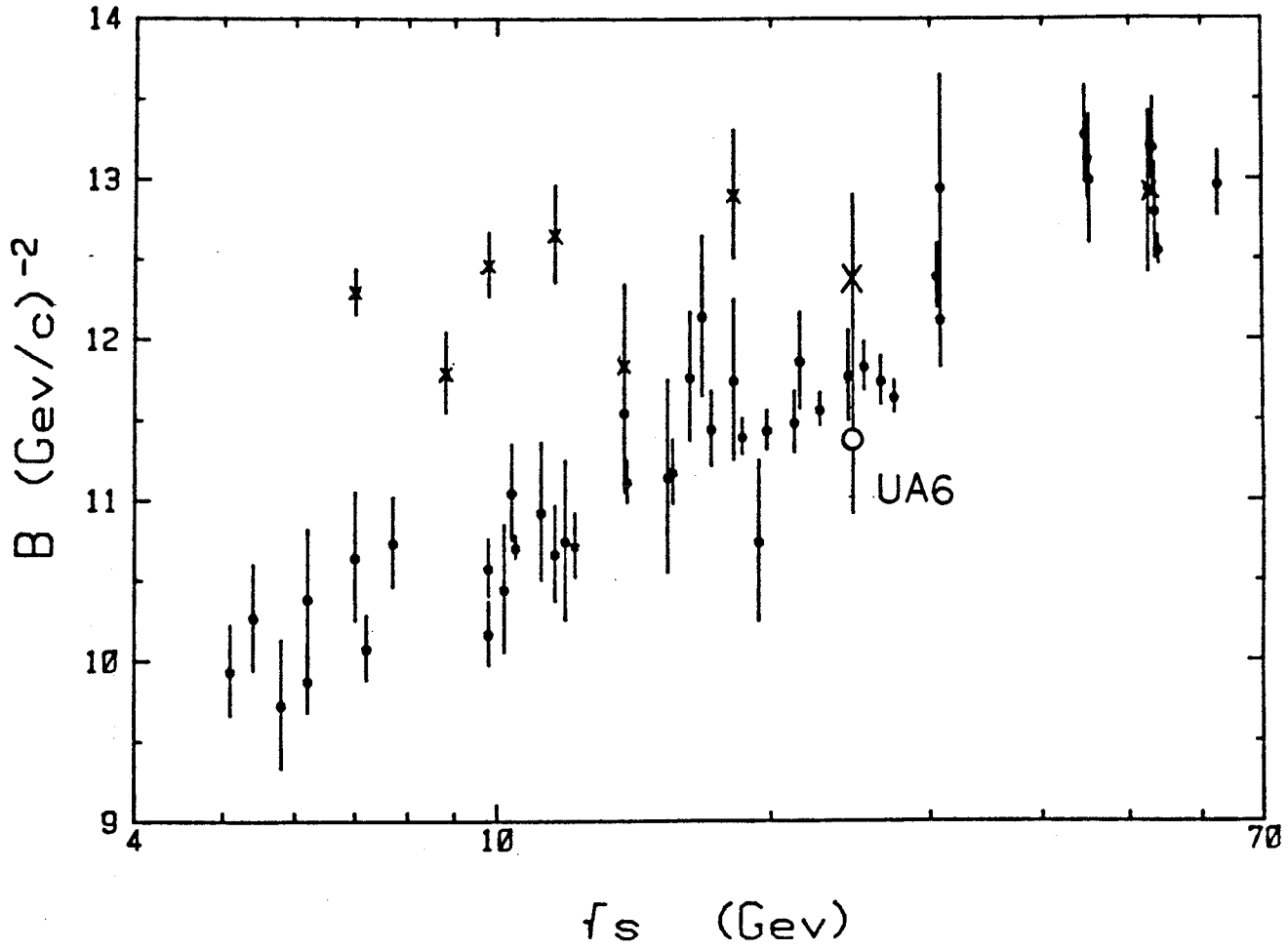

Figure 10.5 The UA6 slope values compared to measurements at other energies. Points marked "x" are $p\bar{p}$, circles are pp. Plot adapted from Ref. 3.11.

REFERENCES

1.1 Rutherford, E., **Philosophical Magazine** 6th Series 21 (1911) 669.

1.2 Kirillova, L. F. **et al.**, **Yadernaya Fizika** (USSR) 1 (1965) 533-539 ['Small-angle Elastic pp and pd Scattering in the Energy Interval 2-10 GeV,'**Soviet Journal of Nuclear Physics** 1 (1965) 379-383].

Akimov, Y. K. **et al.**, **Zhyrnal Eksperimentalnoi i Teoreticheskoi Fiziki** (USSR) 48 (1965) 767-769 ['Method of Investigating Elastic pp Scattering at High Energies by Means of Semiconductor Counters,' **Soviet Physics JETP** 21 (1965) 507-508].

Akimov, Y. K. **et al.**, **Journal of Nuclear Physics** (USSR) 4 (1966) 88-92.

Beznogikh, G. **et al.**, 'The Slope Parameter of the Differential Cross-Section of Elastic p-p Scattering in Energy Range 12-70 GeV,' **Physics Letters** 30B (1969) 274-275.

Beznogikh, G. **et al.**, 'Total Elastic p-p, p-d, p-n Cross Sections in the Energy Range of 1-70 GeV,' **Physics Letters** 43B (1973) 85-88.

1.3 Beznogikh, G. **et al.**, 'Small Angle Proton-Proton Elastic Scattering from 9 to 70 Gev/c,' **Physics Letters** 39B (1972) 411-413.

1.4 Bartenev, V. **et al.**, 'Small-Angle Elastic Proton-Proton Scattering from 25 to 200 GeV,' **Physical Review Letters** 29 (1972) 1755-1758.

Bartenev, V. **et al.**, 'Measurement of the Slope of the Diffraction Peak for Elastic p-p Scattering from 8 to 400 GeV,' **Physical Review Letters** 31 (1973) 1088-1091.

Bartenev, V. **et al.**, 'Real Part of the Proton-Proton Forward-Scattering Amplitude from 50 to 400 GeV,' **Physical Review Letters** 31 (1973) 1367-1370.

A review of the gas jet technique applied to this type of measurement may be found in Melissinos, A. C. and S. L. Olsen, 'Physics (and Technique) of Gas Jet Experiments,' **Physics Reports** 17C (1975) 77-132.

1.5 Amaldi, U. **et al.**, 'Measurements of the Proton-Proton Total Cross Section by Means of Coulomb Scattering at the CERN Intersecting Storage Rings,' **Physics Letters** 43B (1973) 231-236.

Amaldi, U. **et al.**, 'The Energy Dependence of the Proton-Proton Total Cross-Section for Centre-of-Mass Energies between 23 and 53 GeV,' **Physics Letters** 62B (1976) 460-466.

1.6 Amendolia, S. R. et al., 'Measurement of the Total Proton-Proton Cross-Section at the ISR,' **Physics Letters** 44B (1973) 119-124.

Amendolia, S. R. et al., 'Total Cross-Section Measurment at the ISR,' **Nuovo Cimento** 17A (1973) 735-756.

1.7 Amos, N. et al., 'Comparison of Small-angle $p\bar{p}$ and pp Elastic Scattering at 52.8 GeV Center-of-mass Energy at the CERN Intersecting Storage Rings,' **Physics Letters** 120B (1983) 460-464.

Amos, N. et al., 'Comparison of Small-Angle $p\bar{p}$ and pp Elastic Scattering at the CERN Intersecting Storage Rings,' **Physics Letters** 128B (1983) 343-348.

1.8 Carboni, G. et al., 'Measurement of the Antiproton-Proton Total Cross Section and Elastic Scattering at the CERN Intersecting Storage Rings,' **Physics Letters** 108B (1983) 145-150.

Carboni, G. et al., 'Evidence of a Rise in the Antiproton-Proton Total Cross Section at the CERN Intersecting Storage Rings,' **Physics Letters** 113B (1983) 87-92.

Ambrosio, M. et al., 'Measurement of Elastic Scattering in Antiproton-Proton Collisions at 52.8 GeV Centre-of-Mass Energy,' **Physics Letters** 115B (1982) 495-502.

1.9 Bernard, D. et al., 'The Real Part of the Proton-Antiproton Elastic Scattering Amplitude at the Centre of Mass Energy of 546 GeV,' **Physics Letters** B198 (1987) 583-589.

1.10 Antille, J. et al., 'Proposal for the Study of e^+e^-, γ, π° and Hyperon Production in $\bar{p}p$ Reactions at $\sqrt{s}$ = 22.5 GeV Using an Internal Jet Target at the SPS,' CERN SPSC/80-63 SPSC/P 148 (1980).

1.11 Bartenev, V. D. et al., **Yazernaya Fizika** 23 (1976) 759-768 ['Measurement of the Real Part of the Elastic pp Scattering Amplitude from 80 to 286 GeV with Silicon Position-Sensitive Detectors,' **Soviet Journal of Nuclear Physics** 23 (1976) 400-404.]

2.1 Bethe, H., 'Scattering and Polarization of Protons by Nuclei,' **Annals of Physics** 3 (1958) 190-240.

2.2 West, G. B. and D. R. Yennie, 'Coulomb Interference in High-Energy Scattering,' **Physical Review D** 172 No. 5 (1968) 1413-1422.

2.3 Cahn, R., 'Coulomb-Hadronic Interference in an Eikonal Model,' **Zeitschrift für Physik** C15 (1982) 253-260.

2.4 Goulianous, K., 'Diffractive Interactions of Hadrons at High Energy,' **Physics Reports** 101 (1983) 169-219.

2.5 Amaldi, U. et al., 'The Real Part of the Forward Proton Proton Scattering Amplitude Measured at the CERN Intersecting Storage Rings,' **Physics Letters** 66B (1976) 390-394.

3.1 Froissart, M., 'Asymptotic Behavior and Subtractions in the Mandelstam Representation,' **Physical Review D** 123 (1961) 1053-1057.

3.2 Martin, A., 'Extension of the Axiomatic Analyticity Domain of Scattering Amplitudes by Unitarity,' **Nuovo Cimento** 42A (1966) 930-954.

Łukaszuk, L. and A. Martin, 'Absolute Upper Bounds for $\pi\pi$ Scattering,' **Nuovo Cimento** 52A (1967) 122-145.

3.3 Pomeranchuk, I. Ya., **Zhyrnal Eksperimentalnoi i Teoreticheskoi Fiziki** 34 (1958) 725-728 ['Equality of the Nucleon and Antinucleon Total Interaction Cross Section at High Energies,' **Soviet Physics JETP** 7 (1958) 499-501.]

3.4 Eden, R. J., 'Use of Unitarity in Proving Pomeranchuk's Theorem on Cross Sections at High Energies,' **Physical Review Letters** 16 (1966) 39-41.

Kinoshita, T., **Perspectives in Modern Physics**, Ed. R. E. Marshak, New York: Wiley and Sons (1966) 211-213.

3.5 Discussed in Martin, A., 'What Do We Learn From Proton-Antiproton Diffractive Scattering at the CERN Colliders,' **Zeitschrift für Physik C** 15 (1982) 185-191.

3.6 Łukaszuk, L. and B. Nicolescu, 'A Possible Interpretation of pp Rising Total Cross-Sections,' **Lettere al Nuovo Cimento** 8 (1973) 405-413.

Kang, K. and B. Nicolescu, 'Models for Hadron-Hadron Scattering at High Energies and Rising Total Cross Sections,' **Physical Review D** 11 (1975) 2461-2465.

Gauron, P. and B. Nicolescu, 'Are There New Effects in the ISR and Collider $\bar{p}p$ and pp Data?' **Physics Letters** 124B (1983) 429-434.

3.7 Bernard, D., P. Gauron and B. Nicolescu, 'Odderon Interpretation of the New UA4 $\rho(\bar{p}p)$ Datum,' **Physics Letters** B199 (1987) 125-130.

3.8 Fischer, J., R. Saly and I. Vrkoc, 'Pomeranchuk-Type Theorems for Total and Elastic Cross Sections,' **Physical Review D** 18 (1978) 4271-4281.

3.9 Kinoshita, T., 'Pomeranchuk-Like Theorem That Can Be Proved,' **Physical Review D** 2 (1970) 2346-2348.

3.10 Cornille, H. and A. Martin, 'A "Pomeranchuk" Theorem for Elastic Diffractive Peaks,' **Physics Letters** 40B (1972) 671-674.

Cornille, H. and A. Martin, 'Constraints on the Phases of Helicity Amplitudes Due to Positivity,' **Nuclear Physics B** 77 (1974) 141-162.

3.11 Block, M. M. and R. Cahn, 'High Energy $p\bar{p}$ and pp Forward Elastic Scattering and Total Cross Sections,' **Reviews of Modern Physics** 57 (1985) 563-598.

3.12 Söding, P., 'Real Part of the Proton-Proton and Proton-Antiproton Forward Scattering Amplitude at High Energies,' **Physics Letters** 8 (1964) 285-287.

3.13 Khuri, N. and T. Kinoshita, 'Real Part of the Scattering Amplitude and the Behavior of the Total Cross Section at High Energies,' **Physical Review** 137B (1965) 720-729.

Khuri, N. and T. Kinoshita, 'Forward Scattering Amplitude and Univalent Functions,' **Physical Review** 140B (1965) 706-720.

3.14 Amos, N. **et al.**, 'Measurement of Small-angle Antiproton-Proton and Proton-Proton Elastic Scattering at the CERN Intersecting Storage Rings,' **Nuclear Physics** B262 (1985) 689-714.

3.15 Bourrely, C. and J. Fischer, 'Analytic Parametrization of High Energy Forward Scattering Amplitudes (I). pp and $p\bar{p}$ Scattering,' **Nuclear Physics** B61 (1973) 513-521.

3.16 Block, M. M. and R. N. Cahn, 'Forward Hadronic pp and $\bar{p}p$ Elastic Scattering Amplitudes: Analysis of Existing Data and Extrapolations to Collider Energies,' **Physics Letters** 120B (1982) 224-228.

Block, M. M. and R. N. Cahn, 'Consequences of $S\bar{p}pS$ Collider Data for Extrapolations of Cross Sections and Slopes,' **Physics Letters** 168B (1986) 151-157.

3.17 Block, M. M. and R. N. Cahn, 'High Energy Predictions for $\bar{p}p$ and pp Elastic Scattering and Total Cross Sections,' IInd International Conference on Elastic and Diffractive Scattering (October 1987) The Rockefeller University, New York.

4.1 Rubbia, C., P. McIntyre, and D. Cline, Proceedings of the International Neutrino Conference (1976) Aachen.

Rubbia, C., P. McIntyre, and D. Cline, 'Producing Massive Neutral Intermediate Vector Bosons with Existing Accelerators.' In Faissner, Reithler and Zerwas (1977) 683.

4.2 Mohl, D., G. Petrucci, L. Thorndahl, and S. van der Meer, 'Physics and Technique of Stochastic Cooling,' **Physics Reports** 58 (1980).

4.3 CLMR Collaboration, 'The UA6 Experiment,' 5th Topical Workshop on Proton-Antiproton Collider Physics,' Saint-Vincent (Feb. 1985).

4.4 A more complete description of the magnetic spectrometer may be found in Bernasconi, A., 'Contribution à l'étude de la production de π°, η et γ de grande impulsion transverse dans les interactions $\bar{p}p$ et pp à $\sqrt{s}$ = 24.3 GeV au SPS du CERN,' Faculté des Sciences, Université de Lausanne (unpublished thesis).

4.5 Vacchi, A., 'Large-area Transition Radiation Detectors for Electron Identification in the UA6 Experiment at the CERN $p\bar{p}$ Collider,' Proceedings of the Wire Chamber Conference, Vienna (Feb. 1986).

4.6 Antille, J. et al., 'A Measurment of the Inclusive π° and η Production Cross Sections at High p_t in $\bar{p}p$ and pp Collisions at $\sqrt{s}$ = 24.3 GeV,' **Physics Letters** B194 (1987) 568-572.

4.7 Cox, P. T., 'Direct Photon Production in pp and $\bar{p}p$ Collisions,' Advanced Research Workshop on QCD Hard Hadronic Processes, St. Croix, USVI, (Oct. 1987).

Bernasconi, A. et al., 'Direct Photon Production in Proton-Antiproton Interactions at $\sqrt{s}$ = 24.3 GeV,' CERN-EP/88-31 (1988).

4.8 Becker, E. W., R. Klingelhöfer and P. Lohse, **Z. Naturforsch.**, 17a (1962) 432.

4.9 EG&G Ortec, 'The Whys and Wherefores of Charged Particle Detector Spectrometry' (1985).

4.10 Norbeck, E. and R. C. Carlson, **National Academy of Science-National Research Council Publication** 1184 (1963) 42.

Ludwig, E. J., W. M. Gibson and J. S. Hood, **IEEE Transactions on Nuclear Science** NS-12 (1965) 247.

Owen, R. B. and M. L. Awcock, **AERE** R5393 (1967).

4.11 Walton, J., LBL, private communication.

4.12 Parametrization of data from Williamson, C. F., J. P. Boujot and J. Picard, CEA-R-3042 (July 1966).

6.1 Langley, R. A., 'Study of the Response of Silicon-Barrier Detctors to Protons and α-Particles,' **Nuclear Instruments and Methods** 113 (1973) 109-112.

7.1 EG&G Ortec, Oak Ridge, TN, private communication.

8.1 **American Institute of Physics Handbook**, McGraw-Hill (1972) 8-179.

8.2 Kuznetsov, A. A. **et al.**, **Yadernaya Fizika** (USSR) 30 (1979) 1018-1028 ['Diffractive Dissociation of Protons on Protons at Very Small Momentum Transfers and at Energies 50-400 GeV,' **Soviet Journal of Nuclear Physics** 30(4) (1979) 529-534.]

8.3 De Kerret, H. **et al.**, 'Experimental Results on Diffractive One-Pion Production at the CERN ISR,' **Physics Letters** 63B (1976) 477-482.

Biel, J. **et al.**, 'Features of Diffractive Dissociation of Neutrons in np Collisions at 50-300 GeV/c^2,' **Physical Review Letters** 36 (1976) 504-507.

Biel, J. **et al.**, 'Decay Properties of $p\pi^-$ Systems Produced in Neutron Dissociation at 50-300 GeV/c^2,' **Physical Review Letters** 36 (1976) 507-510.

Biel, J. **et al.**, 'Structure in Momentum-Transfer for $(p\pi^-)$ Systems Produced in Diffractive Dissociation of Neutrons on Protons,' **Physics Letters** B65 (1976) 291.

10.1 Block, M. M., private communication (1987).

10.2 Breedon, R. E., 'The Real Part of the Forward Elastic Scattering Amplitude for pp and $\bar{p}p$ at $\sqrt{s}$ = 24.3 GeV from Experiment UA6,' IInd International Conference on Elastic and Diffractive Scattering (October 1987) The Rockefeller University, New York.

10.3 Amos, N., 'Measurements of Proton-Proton and Proton-Antiproton Elastic Scattering at the European Center for Nuclear Research Intersecting Storage Rings,' Northwestern University, Evanston, Illinois (unpublished thesis) 164.

10.4 Buttimore, N. H., E. Gotsman and E. Leader, 'Spin-Dependent Phenomena Induced by Electromagnetic-Hadronic Interference at High Energies,' **Physical Review D** 18 (1978) 694-716. [Erratum, **Physical Review D** 35 (1987) 407.]

10.5 Buttimore, N. H., private communication (1987).

10.6 Martin, A., private communication (1987).

10.7 Foley, K. J. **et al.**, 'High-Energy, Small-Angle p-p and $\bar{p}$-p Scattering and p-p Total Cross Sections,' **Physical Review Letters** 19 (1967) 857-860.

Fajardo, L. A. et al., 'Real Part of the Forward Elastic Nuclear Amplitude for pp, $\bar{p}p$, π^+p, π^-p, K^+p, and K^-p Scattering Between 70 and 200 GeV/c,' **Physical Review** D24 (1981) 46-64.